Laser Drilling of Metals with a XeCl Excimer Laser

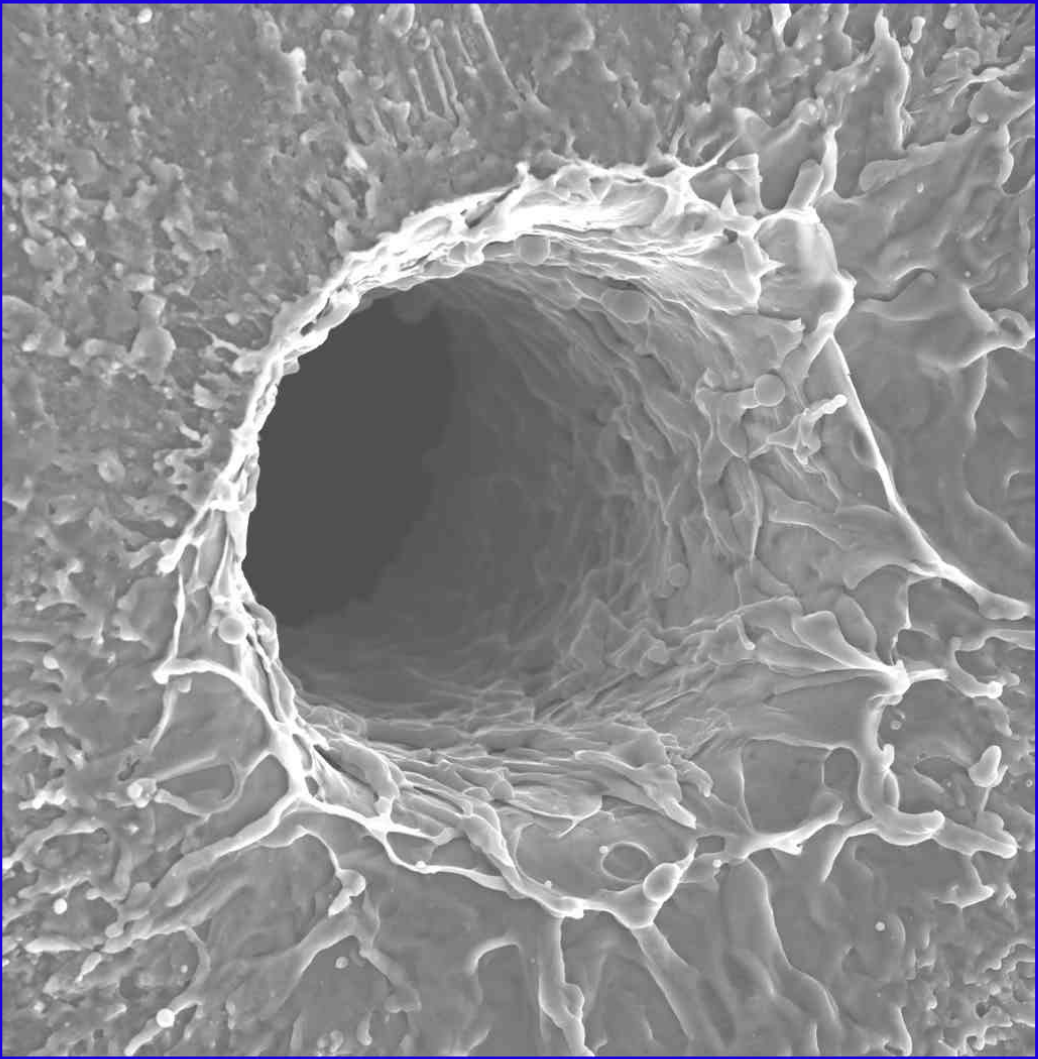

Aart Schoonderbeek

Laser Drilling of Metals
with a
XeCl Excimer Laser

Cover image: *Scanning Electron Microscope (SEM) image of a 50 μm hole, drilled in 125 μm aluminium foil.*

NCLR
NEDERLANDS CENTRUM
VOOR LASER RESEARCH

This research was carried out at Nederlands Centrum voor Laser Research (www.nclr.nl)

Laser Drilling of Metals with a XeCl Excimer Laser
Schoonderbeek, Aart
ISBN 90-365-2126-2

Printed by Print Partners Ipskamp, Enschede

LASER DRILLING OF METALS WITH A XECL EXCIMER LASER

PROEFSCHRIFT

ter verkrijging van
de graad van doctor aan de Universiteit Twente,
op gezag van de rector magnificus,
prof. dr. W.H.M. Zijm,
volgens besluit van het College voor Promoties
in het openbaar te verdedigen
op vrijdag 21 januari 2005 om 13.15 uur

door

Aart Schoonderbeek

geboren op 5 juni 1974

te Zwolle

Dit proefschrift is goedgekeurd door de promotoren,
Prof. dr. ir. J. Meijer
Prof. dr. K.-J. Boller

Contents

Publications

- **A. Schoonderbeek**, C.A. Biesheuvel, R.M. Hofstra, K.-J. Boller, J. Meijer, The influence of the pulse length on the drilling of metals with an excimer laser, Journal of Laser Applications, vol. 16, nr. 2, pp. 85-91, 2004.
- **A. Schoonderbeek**, C. Biesheuvel, R. Hofstra, K.-J. Boller, J. Meijer, Shadowgraphic imaging of material removal during laser drilling with a long pulse excimer laser, Applied Physics A, published online, 2004.
- T. Masuzawa, J. Meijer, T. Bourouina, **A. Schoonderbeek**, J. Eindhoven, Laser beam machining of microlenses by hole area modulation (HAM) method, pp. 395-398 in Proceedings of the Euspen Conference 2002 (ISBN 90-386-2883-8), The Netherlands, 2002.
- **Aart Schoonderbeek**, Cornelis A. Biesheuvel, Ramon M. Hofstra, Klaus-J. Boller and Johan Meijer, High speed drilling of metals with a long pulse XeCl excimer laser, pp. 667-677 in Proceedings of High-Power Laser Ablation IV, SPIE 4760, USA, 2002.
- **A. Schoonderbeek**, C.A. Biesheuvel, R.M. Hofstra, K.-J. Boller, J. Meijer, High speed drilling of metals with a long pulse XeCl excimer laser, in Proceedings of ICALEO 2002, USA, 2002, CD-ROM.
- **A. Schoonderbeek**, C.A. Biesheuvel, R.M. Hofstra, K.-J. Boller, J. Meijer, Shadowgraphic imaging of metal drilling with a long pulse excimer laser, pp. 395-400 in Proceedings LPM 2003, SPIE 5063 (ISBN 0-8194-4869-9, ISSN 0277-786x), Germany, 2003.
- **A. Schoonderbeek**, C. Biesheuvel, R. Hofstra, K.-J. Boller, J. Meijer, Material ejection during drilling with a long pulse excimer laser, in Proceedings of ICALEO 2003, USA, 2003, CD-ROM.
- D.F. de Lange, **A. Schoonderbeek**, J. Meijer, Melt ejection during laser drilling, in Proceedings of ICALEO 2004, USA, 2004, CD-ROM.
- D.F. de Lange, **A. Schoonderbeek**, J. Meijer, Simulation of meltpool surface shape for laser drilling and welding, pp. 337-348 in Proceedings of LANE 2004 (ISBN 3-87525-202-0), Germany, 2004.

Chapter 1

Introduction

Albert Einstein (1917) introduced the concept of stimulated emission, which is the basic process for a laser. The word laser is an acronym for Light Amplification by Stimulated Emission of Radiation. The realisation of the first laser was published by the group of C.H. Townes (Gordon *et al.*, 1955). At that time, Townes' system was not called a laser, but a maser as it operated in the microwave range. Schawlow and Townes published ideas to extend maser techniques to the infrared and optical range (Schawlow and Townes, 1960). The first laser at visible wavelength was constructed by Maiman (1960). Soon after the laser was invented it was dubbed as ”a solution looking for a problem”. So new was the tool, that thinking had not caught up with the possibilities.

Nowadays many different types of lasers are known. A comprehensive overview of the working principle of lasers, its dynamics and properties, as well as an overview of the various types of lasers is given by Siegman (1986). Commonly the 'laser medium' is used as the basis of the classification in different types. The types that have the highest relevance for industrial processes are the gas lasers, solid-state lasers and semiconductor lasers. Gas lasers emit radiation with the widest variety of wavelengths compared to lasers using other active media. With gas lasers very high output powers can be obtained. A special type of the gas laser is the excimer laser, which emits in the ultraviolet wavelength range of the spectrum. First excimer laser radiation (Xe_2^*) was published by Basov *et al.* (1971).

Historically, laser drilling was the first industrial application by Western Electric, using a ruby laser in 1965 to drill holes in diamond dies for extrusion (Steen, 1998). Nowadays a wide variety of applications for laser radiation is known. Lasers are used, for example, for measurement and detection, for transmission of information through glass fibres, for material processing and for ignition for nuclear fusion. Lasers are found in well-known equipment like compact disc players and recorders, barcode cash-registers and printers. Laser material processing has become of industrial importance and includes cutting, welding, hardening, bending, cladding and drilling. Laser beams are used as a tool for all these applications because of the unique properties of the laser light.

1.1 Research definition

This thesis is about laser drilling with a unique excimer laser. Since the mid-1980s, European researchers have been attempting to develop powerful excimer lasers that are capable of industrially processing of materials. The goal of two Eureka projects, EU213 and EU205, was to develop a high power 1kW, 1kHz excimer laser (Bell, 1996). Afterwards, two groups continued the research. The French group Sopra (Uteza *et al.*, 2000) and the Dutch NCLR (Timmermans *et al.*, 2000). The knowledge obtained by NCLR in this project was used for the development of a unique XeCl excimer laser with a nearly diffraction limited beam and 175 ns pulse duration (Hofstra *et al.*, 2000). During recent years a lot of research was done on applications of this laser.

The mentioned excimer laser has a lot of advantages for material processing. It is known that nanosecond laser pulses with a short wavelength are highly suitable for high accuracy processing of various types of material (Von Allmen and Blatter, 1995; Bäuerle, 2000). The advantages found with short wavelengths are, among others, an increased absorption by the material and a decreased absorption by the plume. The combination of high processing speed and high processing quality suitable for industrial applications can only be obtained with lasers with high average output power. Mask projection is commonly used in material processing with standard excimer lasers but blocks a large part of the laser energy from usage, which results in a low processing speed. With the NCLR laser a high processing speed is possible because the excellent beam quality enables usage of the entire beam instead of using mask projection techniques. Further, focussing of the diffraction limited beam, leads to high power densities. The research described in this thesis contributes to understanding of drilling metals with such a novel excimer laser. Because of the lack of suitable excimer lasers, scarcely any experimental investigations were published in the parameter regime of this laser, before this study started. The research definition for this thesis is as follows:

> *Study the drilling of metals with a XeCl excimer laser with a nearly diffraction limited beam and relatively long optical pulse duration. This to obtain a fundamental understanding of the underlying processes, which is essential to achieve the highest processing speed and to control the quality of the drilled holes.*

1.2 Outline thesis

In chapter 2, the laser drilling process is described. Attention is given to different processes which play an important role: the heating of the material by the laser beam, the melting and evaporation, the build-up of a recoil pressure as a consequence of the evaporation, and the interaction of the laser beam with the cloud of vapour and melt above the hole. In chapter 3 the equipment and methods are described, which are used for the experiments. After that, a description is given of the characteristics of the laser that are the most important for material processing. Information is given about the properties of the laser beam and how these are obtained. It ends with an overview of the methods for hole analysis. Chapter 4 is about the influence of the pulse duration on the hole drilling of metals. It is shown that high speed and high efficiency drilling of metals is possible with long pulse excimer lasers with a high beam quality. In chapter 5 the results are described of studying the material removal during laser drilling and the transparency of the plume at the wavelength of the drilling laser. In chapter 6 the numerical model is described, which is developed to describe and to quantify the phenomena during drilling. This modelling is done in a parameter regime, which is minimally described in literature so far. Calculations done with the model are compared with experimental results and give a good explanation of the relevant processes. Finally, chapter 7 gives a summary of the research.

Chapter 2

The laser drilling process

For many years, solid state lasers have been used in machining processes like drilling of cooling holes in jet engine components. These lasers have pulse durations in the millisecond range, which results in a clearly present recast layer and heat-affected zone. However, industry demands improvements in the quality of machined features. More specifically, the drilled holes have to be more consistent in geometry, and must exhibit minimal recast layers and heat-affected zones. Application of hard-to-machine materials makes laser drilling even more challenging. In this thesis a laser with short pulse duration in the nanosecond range is used. Therefore, material is removed with a very small heat-affected zone compared to laser material processing with pulse durations in the millisecond range.

For a better understanding of this thesis, a simplified description is given of the different stages and physical effects during the laser drilling process. This description is based on the work done for this thesis and is illustrated by figure 2.1. In figure 2.1a the target is shown, before it is hit by the laser beam. In figure 2.1b the laser beam has just reached the target surface. Part of the laser beam is reflected as indicated by the arrow in figure 2.1b. The absorbed part of the laser beam heats the material, as is shown in figure 2.1c. For this and further pictures the reflected part is not drawn for clarity reasons, but it remains during the entire pulse duration. When the heat flow rate is high enough, the material starts to melt. This is shown in figure 2.1d by the development of a melt pool with a curved solid-liquid interface. For further heating, the surface reaches temperatures above the boiling temperature, such that significant vaporization starts (figure 2.1e). At high vaporization rates, the vapour particles exert a pressure on the melt surface. This recoil pressure accelerates the melt and ejects

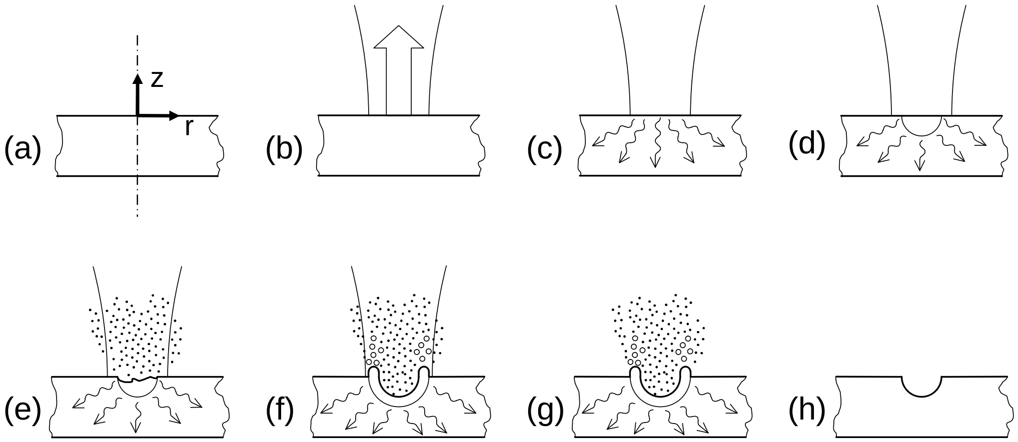

Figure 2.1: *Schematic overview of the laser drilling process.*

- *a.)* *The target before the laser pulse has started.*
- *b.)* *The laser beam hits the surface and is partially reflected.*
- *c.)* *Material heating.*
- *d.)* *Material melting.*
- *e.)* *Material vaporization.*
- *f.)* *Acceleration of the melt by the recoil pressure. The laser beam travels through a cloud of particles.*
- *g.)* *After the laser pulse has ended ejection of melt and vaporization continues.*
- *h.)* *Material removed with a single pulse.*

it out of the hole as is shown in figure 2.1f. In figure 2.1f it is shown that the laser beam has to travel through a cloud of particles. This cloud or plume can attenuate the laser beam before it reaches the processing region. This attenuation is caused by scattering and absorption of the laser light by particles in the plume, like melt droplets, vapour, ionized vapour, and condensed material clusters. After the laser pulse has ended ejection of melt and vaporization continues as is shown in figure 2.1g until the temperature increases below the boiling and melting temperature. In figure 2.1h it is shown how the hole looks after the laser pulse has ended and the material has cooled down. Figure 2.1h shows that, in general, for drilling a hole through the target with nanosecond pulse duration, a series of pulses is necessary. Each of the above mentioned processes will be described into more detail in the following sections. These descriptions will be used in the following chapters to explain the experimental results and the modelling.

2.1 Absorption of the laser beam

In general, a laser beam irradiating a target is partially reflected, partially transmitted and partially absorbed. Suppose that the laser beam hits the target vertically and propagates into the negative z-direction (figure 2.1a and 2.1b). In this case the attenuation of the beam in the material by absorption is described by Lambert-Beer's exponential law with the optical absorption coefficient α. Thus, the internal heat generation Q follows the same exponential decay function versus depth (Von Allmen and Blatter, 1995; Bäuerle, 2000). More specifically, absorption of a normal incident and rotationally symmetric laser beam results in the following distribution of the heating as function of radius r, depth z and time t,

$$Q(r,z,t) = I(r,z=0,t)\,\alpha e^{\alpha z} \tag{2.1}$$

where I is the power density. The optical absorption length l_α is the depth at which the power density has decreased to a fraction of $1/e$ with respect to its value on the surface, and is

$$l_\alpha = \alpha^{-1}. \tag{2.2}$$

For metals optical absorption lengths are typically in the order of 10 nm. When the material removal process is dominated by vaporization the removal per pulse, for nanosecond pulses, is in the order of 100 nm (Song and Xu, 1998; Williams *et al.*, 1998). When the process is dominated by melt ejection, like in the experiments described in this thesis, the removed depth per pulse is in the order of 1 to 100 μm (chapter 4 and chapter 5). Thus, in the melt ejection regime, the layer in which the laser beam energy is absorbed is significantly thinner than the removed depth per pulse. Therefore, the optical transmission during the pulse is small enough to be safely neglected.

To determine the laser energy used in the drilling process, it is necessary to know which amount is absorbed and which amount is reflected. The absorbed fraction of the laser energy depends on the processed material, the wavelength of the laser beam, the angle of incidence, polarization, and a number of geometrical effects. Furthermore it depends on the temperature of the target, in particular if the target surface changes from the solid state to the liquid state by melting. In practice the absorbed fraction of the beam energy, called absorptivity A, is also influenced by the surface roughness, oxide layers, and impurities at the surface. For drilling deeper holes, multiple reflections can play a role. Because some of the mentioned parameters change during the drilling process, the absorptivity also changes during the process. Some of the mentioned parameters are explained in further detail to show their influence on the drilling process.

Table 2.1: *Absorbed fraction of the energy (absorptivity) for a normal incident laser beam at a polished surface at room temperature and atmospheric pressure for different wavelengths (Bäuerle, 2000).*

material	$A(\lambda)$	$A(\lambda = 1.06\,\mu\text{m})$	$A(\lambda = 10.6\,\mu\text{m})$
Al	0.14 (305 nm)	0.06-0.38	0.02
Cu	0.75 (300 nm)	0.02-0.29	0.01
Au	0.72 (357 nm)	0.02	0.02
Fe	0.43 (600 nm)	0.36	0.3
Mo	0.37 (248 nm)	0.3-0.39	
Ni	0.51 (357 nm)	0.33	0.03

Wavelength

The absorbed fraction of the energy, $A \leq 1$, shows a general trend to increase when the incident radiation wavelength decreases when going from the infrared to the ultraviolet spectral range. Typical absorptivities in the near ultraviolet and visible spectral range for some metals are shown in table 2.1.

Angle of incidence and polarization

It will be explained how the absorptivity depends on the angle of incidence. Whereas at normal incidence, the absorption of radiation does not depend on polarisation, for oblique incidence the polarisation becomes important. The absorptivity can be calculated as a function of the incidence angle θ_i for linearly polarized radiation directed parallel (index ||) or perpendicular ($\perp$) to the surface (Prokhorov *et al.*, 1990)

$$A_{\|}(\theta_i) = 1 - R_{\|}(\theta_i) = 1 - \frac{(n_1^2 + n_2^2)\, cos^2\theta_i - 2\, n_1\, cos\,\theta_i + 1}{(n_1^2 + n_2^2)\, cos^2\theta_i + 2\, n_1\, cos\,\theta_i + 1} \tag{2.3}$$

$$A_{\perp}(\theta_i) = 1 - R_{\perp}(\theta_i) = 1 - \frac{(n_1^2 + n_2^2)\; - 2\, n_1\, cos\,\theta_i + cos^2\theta_i}{(n_1^2 + n_2^2)\; + 2\, n_1\, cos\,\theta_i + cos^2\theta_i} \tag{2.4}$$

assuming $\theta_i \leq 90°$ with θ_i defined as the angle with respect to the normal of the surface, and the complex index of refraction $\vec{\mathbf{n}}_{\mathbf{r}} = n_1 + i\, n_2$. In these equations R is the reflectivity, n_1 is the real part, called refractive index, and the imaginary

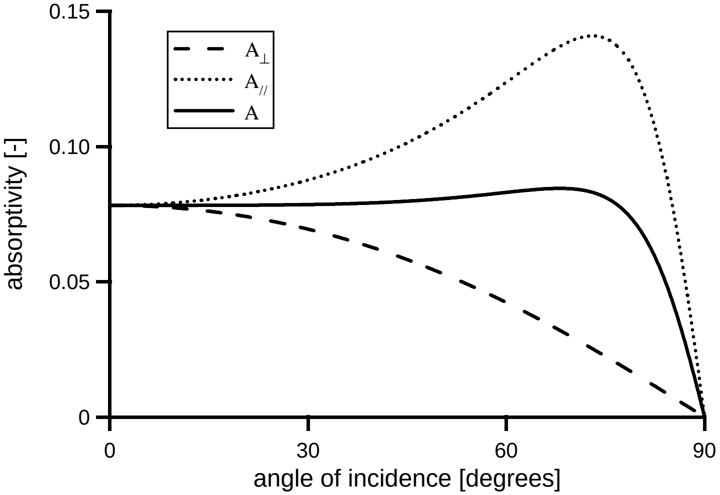

Figure 2.2: *Normal-incidence absorptivity of an evaporated aluminium coating for polarized and non-polarized 308 nm radiation with* $n_1 = 0.26$ *and* $n_2 = 3.42$ *(Gray, 1972).*

part n_2 is called the extinction coefficient. The extinction coefficient is related to the optical absorption coefficient α as

$$n_2 = \frac{\lambda\,\alpha}{4\pi}. \tag{2.5}$$

For non-polarized light as well as for circularly polarized light, equations 2.3 and 2.4 can be combined to

$$A = 0.5(A_{||} + A_{\perp}). \tag{2.6}$$

In figure 2.2 an example is shown of the dependence of the absorptivity on the angle of incidence. For the combined absorptivity it can be seen that the influence of the angle of incidence up to 70° is small. However for larger angles, the absorptivity decreases quickly and almost vanishes for an almost parallel incidence of the light. This effect in combination with multiple reflections, as described in the next section, may influence the drilling of deeper holes, where a rather large amount of the laser beam hits the walls of a deep and narrow hole where large angles of incidence are expected. On the other hand, there is no strong influence expected due to the change in absorptivity with the angle of incidence, for holes that are shallow in comparison with the diameter.

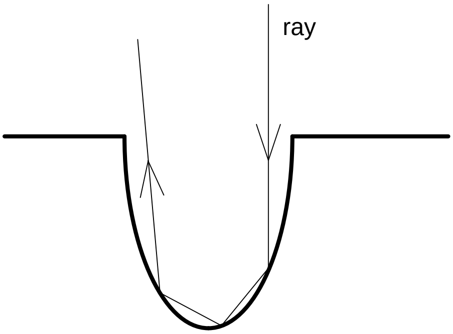

Figure 2.3: *A typical path of an individual ray undergoing multiple reflections.*

Multiple reflections

Multiple reflections in an already formed hole compared with the irradiation of a flat surface may lead to higher energy input because part of the laser light reflected within the hole is absorbed when it is irradiating the hole wall again (Solana and Negro, 1997). To describe the power density distribution in the hole it is necessary to consider the way the laser light is redistributed when it is reflected from the hole wall. This distribution can be obtained in different ways. For example, when the dimensions of the hole are much larger than the wavelength of the laser beam, diffraction and interference can be neglected, and the incident light can be decomposed into individual geometric-optical rays. The path of each individual ray undergoing multiple reflections can be traced out in detail to calculate the power density distribution on the hole wall (Solana and Negro, 1997; Milewski and Sklar, 1996; Ki *et al.*, 2002; Kar *et al.*, 1992). This is shown in figure 2.3, in which a single incident ray is traced. In the shown case, the first reflection of the ray irradiates the wall twice again, which increases the absorbed fraction of the energy. The figure also shows that the reflection points are likely to appear close to or at the bottom of the hole, such that in hole drilling, the energy tends to concentrate near the centre of the bottom of the hole. As a result, the effective power density at the bottom of the hole reaches a value that is higher than the original distribution at the entrance of the hole. Therefore it is expected that multiple reflections lead to deeper, steeper holes (Ruf *et al.*, 1999). However, the presence of a plume inside the hole might dramatically change the energy deposition pattern generated by multiple reflections and might counteract the high concentration of the laser beam on the centre region. For a better estimate of the relative importance of the two effects, the influence of the plume will be discussed in further detail in section 2.4.

Temperature

The absorptivity A, in general, increases with increasing temperature. For many solid metals, this behaviour can be described, by the following empirical linear relationship (Ujihara, 1972)

$$A(T) = A_0 + A_1 \cdot (T - T_{t=0}) \tag{2.7}$$

where A_0 is the absorbed fraction of the energy at reference temperature $T_{t=0}$, and A_1 is a material constant, both depending on the laser wavelength. In general, at longer wavelengths the absolute increase with temperature is small, but the relative increase can be considerable. Typical values of A_1 found in literature for copper are $1 \cdot 10^{-4}$ K^{-1} for 10.6 μm, $2 \cdot 10^{-4}$ K^{-1} for 1064 nm (Ujihara, 1972), and $3 \cdot 10^{-4}$ K^{-1} for 308 nm (Sicard *et al.*, 2001). Beyond the melting temperature the absorptivity of metals increases even further. In the infrared the increase is typically a factor of 1.5-2 (Prokhorov *et al.*, 1990). For shorter wavelengths the increase is smaller. For example, calculations of Sicard *et al.* (2001) show for an aluminium alloy an increase by a factor of 1.2 in the absorptivity after melting, i.e., A changes from 0.29 to 0.35 at a wavelength of 308 nm.

2.2 Heating, melting and vaporization

That amount of the energy of the laser beam which is absorbed at the target surface is converted into heat. This heat is either transported into the material by conduction, or results in melting and vaporization of the material. This section describes these processes.

2.2.1 Heating and melting

In processing metals, most photons are absorbed by the conduction electrons and not by the lattice. Only thereafter, the energy of the excited electrons is dissipated into heating of the lattice by collisions, which happens in picoseconds. This means for laser processing of metals with nanosecond and longer pulses that the laser energy is converted to a good approximation instantaneously into heat, which is transported by conduction, and increases the temperature of the target. The conduction of heat is governed by the following equation (appendix C, equation C.15)

$$c\,\rho \frac{\partial T}{\partial t} = \nabla \cdot (k \nabla T) \tag{2.8}$$

where c is the specific heat, ρ is the density, T is the temperature, t is the time, and k is the thermal conductivity. Equation 2.8 shows that conduction of heat in the target depends on the material properties. In this equation the term on the left hand side represents the rate of change of the accumulated heat in an infinitesimal volume element. The term on the right hand side represents conduction to and from the adjacent volume elements.

Equation 2.8 is used to estimate the power density necessary to reach the melting temperature at the end of a laser pulse with duration t_p. Solving equation 2.8 to obtain a spatial and temporal temperature distribution from arbitrary boundary conditions usually requires numerical methods. However, in simplified cases analytical solutions can be found. In this case a calculation is performed for a laser beam with a top-hat power density distribution and infinitely large diameter, which heats the flat surface of a semi-infinite solid. The time-dependent increase of the surface temperature follows a square-root law

$$T\,(r, z=0, t) - T\,(r, z=0, t=0) = 2\,A_0\,I\sqrt{\frac{t}{c\,\rho\,k\,\pi}} \tag{2.9}$$

where I is the constant power density absorbed at the surface after $t = 0$. Note that equation 2.8 and equation 2.9 apply only to relatively small increases in the temperature, when phase transitions do not yet occur, such as melting or vaporization. For a phase transition from solid to liquid a relatively large amount of heat is necessary, which is called the latent heat for melting, L_m. For pure metals this phase transition occurs at a sharply defined melt temperature T_m. However, for alloys, this phase transition occurs gradually over a certain temperature range. The analytical solution of equation 2.9 can be used up to the melting temperature. The result of the calculation is shown in figure 2.4, where equation 2.9 equal to T_m is used, to plot the power density to melt nickel and aluminium as a function of the pulse duration $t = t_p$ (parameters in appendix B). Figure 2.4 shows that for short pulse durations a high power density is necessary to reach the melt temperature. Although the direct use of equation 2.9 is limited to below the melting temperature additional conclusions can be drawn for hole drilling. As drilling means to remove material and not only to melt material, the surface should reach the melting temperature long before the laser pulse ends. Only then the remaining part of the pulse contains enough energy for further heating and removal of the material. For example, according to equation 2.9 and figure 2.4, a power density of 32 MW/cm^2 is necessary for melting the surface of nickel for processing with a pulse duration of 10 ns. This means that at this power density, pulses much longer than 10 ns will be required for removal of material.

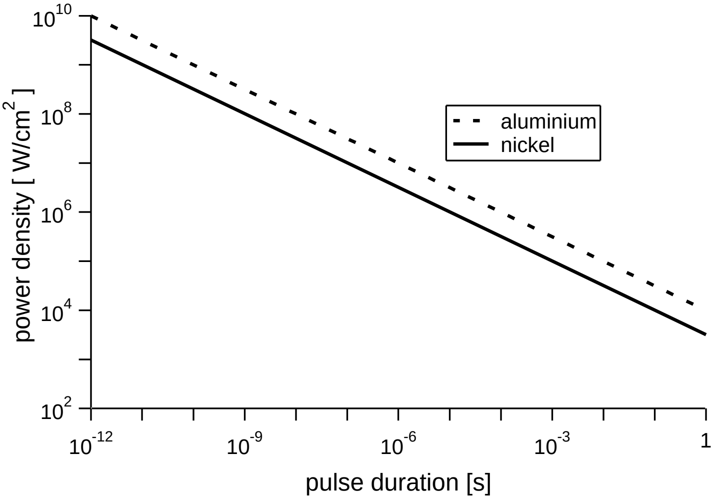

Figure 2.4: *The power density necessary to reach the melting temperature at the end of a laser pulse with a certain pulse duration* t_p *for aluminium and nickel. The lines are constructed according to equation 2.9.*

2.2.2 Vaporization

Strong vaporization starts at the surface when the material is further heated after melting. To understand the influence of the laser parameters on the vaporization process, some theory is presented in this section. The vaporization at the surface leads to a rapid flow of hot gaseous material with high speed, which exerts a recoil pressure distribution on the melt pool. This pressure distribution drives molten material out of the melt pool (Von Allmen and Blatter, 1995). Besides, it has to be mentioned that absorption of the laser beam by the plume can further increase the recoil pressure.

Vapour pressure

In this section, the vapour pressure at the liquid-vapour interface is calculated, which is used in the next section to derive the vaporized mass flow rate. For these calculations, a phase-equilibrium is assumed at the liquid-vapour interface, which is valid in the temperature range from the boiling temperature T_b almost up to the critical temperature T_c (Von Allmen and Blatter, 1995; Song and Xu, 1998; Atkins, 1986). For such a phase-equilibrium, the Clapeyron equation is valid (Atkins, 1986)

$$\frac{dp}{dT} = \frac{\Delta S_m}{\Delta V_m} \tag{2.10}$$

which relates the vapour pressure p to ΔS_m and ΔV_m which are, respectively, the changes of molar entropy and molar volume when the transition from liquid to vapour occurs. The molar entropy of vaporization at a temperature T is equal to $\Delta H_{v,m}/T$, with $\Delta H_{v,m}$ the change of the molar enthalpy of the vapour. With the knowledge that the molar volume of a gas is much greater than the molar volume of a liquid, and the assumption that the vapour behaves like an ideal gas, the Clapeyron equation turns into the Clausius-Clapeyron equation (Atkins, 1986)

$$\frac{d\,ln\,p}{d\,T} = \frac{\Delta H_{v,m}}{R_m\,T^2} \tag{2.11}$$

where R_m is the molar gas constant. For a vaporization enthalpy, which is independent of the temperature, integration results in

$$p(T) = p_0\, e^{\frac{\Delta H_{v,m}}{R_m}\left(\frac{1}{T_b} - \frac{1}{T}\right)} \tag{2.12}$$

where p_0 is the vapour pressure at temperature T_b. Equation 2.12 gives the vapour pressure as a function of the temperature at the surface. This equation will be used in the following sections.

Vapour flow

The vaporized mass flow rate, corresponding to the vapour pressure of equation 2.12 can be calculated with kinetic gas theory. This theory takes into account that the vaporized particles possess a Maxwell-Boltzmann thermal equilibrium velocity distribution at a temperature equal to the surface temperature. This means that a virtual wall at a small distance above the liquid-vapour interface would experience a number of collisions Z_w per unit time per unit area (Atkins, 1986) where Z_w is given by the Maxwell-Boltzmann distribution. Multiplying this number of collisions with the mass of a single vapour particle m gives the vaporized mass flow rate $\dot{m}_v$

$$\dot{m}_v = m\,Z_w = p(T)\sqrt{\frac{m}{2\,\pi\,k_B\,T}} \tag{2.13}$$

where k_B is the Boltzmann constant. Together with the vaporized mass flow rate a heat flow rate leaves the surface. This heat flow rate can be calculated by multiplying the vaporized mass flow rate of equation 2.13 with the enthalpy $H(T)$ of the material

$$q_v = H(T)\,\dot{m}_v. \tag{2.14}$$

Calculations of the vapour flow and recoil pressure

Since the invention of the laser, many authors studied the vaporization of the irradiated target. Anisimov (1968) stated that in the direct vicinity of the vaporizing surface there is a region of several mean free path lengths in which the vapour distribution approaches equilibrium. Anisimov approximated the distribution function within the discontinuity region by the weighted sum of distribution functions before and after the discontinuity with coordinate-dependent coefficients. The expression for the distribution at the vaporizing surface takes into account the fact that the vaporized atoms have a Maxwell-Boltzmann distribution at a temperature equal to the surface temperature, as mentioned in the previous paragraph. The analysis of Anisimov (1968) shows that about 18% of all vaporized particles return to the surface. The net vaporization rate is thus somewhat smaller than the equilibrium value of equation 2.13. This gives for the vaporized mass flow rate $\dot{m}$

$$\dot{m} \approx 0.82\dot{m}_v. \tag{2.15}$$

Similarly the recoil pressure p_r was found from the analysis of Anisimov (1968) to be about half the saturated vapour pressure

$$p_r \approx 0.55p(T). \tag{2.16}$$

The analysis done by Anisimov (1968) is since successfully used by many authors for modelling work, with or without modifications (Knight, 1979; Von Allmen and Blatter, 1995; Bäuerle, 2000; Itina *et al.*, 2003; Morozov, 2004)

2.3 Material removal

In the beginning of section 2.2.2 it was explained that material can be removed not only by vaporization, but also as melt. In this process, the vaporization generates a recoil pressure, which accelerates the melt, deforms the melt pool and finally ejects part of it out of the hole. The melt ejection can occur smoothly, in an explosive way, or as a combination of both.

Melt ejection

Melt ejection during drilling of metals with an excimer laser is until now not well understood for lack of detailed experimental investigations. During the laser drilling experiments described in this thesis it is observed that the material is mainly removed by melt ejection and not by vaporization alone. Common excimer lasers with a pulse duration of 20-30 ns have been used only occasionally for the applications of this thesis. Studies about melt ejection can be found in literature for two major applications. One application is vapour deposition of thin metal and dielectric films (Koren *et al.*, 1990). In this case vaporization is required and melt droplets have to be avoided, in order to obtain dielectric films with high quality. Another application, done with long pulse Nd:YAG lasers, is drilling, in which melt ejection is preferred for a high drilling efficiency because the energy required for melting is significantly less than for vaporization (Voisey *et al.*, 2001). These two examples show that for any given application an individual balance has to be found between an efficient material removal and the desired quality which may suffer from recast.

Finding the required balance can be rather difficult due to the dynamical behaviour of the melt flow. The melt ejection may continue after the laser pulse has ended until complete solidification of the material has occurred. On the other hand, vaporization ends soon after the end of the laser pulse when the energy input ends. Correspondingly, the velocity achieved with a sufficiently long laser pulse should be high enough to eject most of the material in molten state. For the latter it is beneficial if the velocity of the melt is high, depending on the processed material in the range from ten up to a few hundreds of m/s. However, besides the melt velocity, some of the most important parameters for the melt ejection are the viscosity of the melt, the pulse duration, and friction of the wall. A low viscosity of the melt, results in low friction in the melt and therefore a high velocity can be reached, without a high energy consumption. The higher the velocity of the melt which is reached during the laser pulse the more molten material can be ejected before the melt has resolidified after the laser pulse.

Explosive boiling

Two different mechanisms of vaporization are possible. Vaporization at the surface as was described in section 2.2.2 occurs at surface temperatures below the critical temperature, which is named normal boiling. At high surface temperatures above the critical temperature, explosive boiling in the bulk of the melt pool may occur. When this mechanism occurs, the hot region near the surface breaks down in a very short time into vapour and liquid droplets (Miotello and Kelly, 1999). Several authors (Niedrig and Bostanjoglo, 1997; Song and Xu, 1998) conclude from modelling and experimental work that explosive boiling is necessary to explain the high vaporization rates at extremely high power densities. In contrast to this, experimental work for processing of metals with excimer lasers is known only for low power densities and short pulse durations, where material is mainly removed by vaporization. This is compared with a process with mainly melt ejection a less efficient process. Correspondingly, with mainly vaporization as removal process, the achieved removed depths per pulse are observed to be only in the range of 100 nm. With mainly melt ejection as removal process, like in the experiments described in this thesis, an up to 3 orders of magnitude larger removed depth per pulse is found ranging from 1 to 100 μm. For this thesis, experiments have been done in the power density regime where temperatures are expected to reach the critical temperature. Therefore explosive boiling may occur.

2.4 The plume

In section 2.1 was explained that reflection of the incident radiation reduces the amount of absorbed energy, and that multiple reflections can focus the laser beam at the bottom of a hole. However, for a realistic estimate of the power density distribution at the bottom and walls of the hole it is required to discuss the influence of the plume on the hole drilling process. In general, the laser beam will be attenuated when it travels through a plume of removed material. This attenuation is caused by scattering and absorption from particles in the plume, like melt droplets, vapour, ionized vapour, and condensed material clusters. These particles are generated in the following ways. The high power density of the laser beam leads to a fast vaporization of the irradiated material. The vaporized material moves into the surrounding atmosphere and forms a shockwave that compresses the ambient gas. More about the formation of such shockwaves in the experiments is found in chapter 5. The absorption of the laser beam by the plume leads to high temperatures behind the shockwave that may lead to partial ionization of the material vapour. The high number density of the particles (Dyer and Sidhu, 1988; Mehlman *et al.*, 1993) within the expanding material vapour leads to the formation of material clusters (Kar and Mazumder, 1994). Additionally, melt droplets will be found in the plume as was described in section 2.3.

Once a plume is present the incident laser beam interacts with the particles in the plume. Schittenhelm *et al.* (1998) describe three interaction mechanisms, which play an important role. These are the absorption of photons by electrons, named Inverse Bremsstrahlung absorption, ionization of molecules or atoms by the absorption of photons, named Photo-Ionization, and scattering and absorption due to material clusters, named Mie scattering. The contribution of each of these processes depends strongly on the laser wavelength and the atomic species, particularly for infrared radiation and lower power densities. At shorter wavelengths, however, absorption of the laser beam by the plume was found to decrease. Studies in literature (Breitling *et al.*, 1999) showed, at a wavelength of 1064 nm, that a larger amount of the laser radiation was absorbed at the front of the plume, where the beam just entered the plume. Contrary to this, at a wavelength of 355 nm, the laser beam was mainly absorbed at the target and by the vapour close to the target. As there was much less attenuation by the plume, generally, more laser energy reaches the target for material processing with short wavelengths.

Absorption of the laser light by the plume does not only have a detrimental effect, such as reducing the power density of the laser beam reaching the target. In some applications the absorption of the laser light by the plume can have a practical application. The absorption is for example used to generate hot plasmas by irradiating solid targets with visible and ultraviolet nanosecond laser pulses for the deposition of thin solid films. This technique has been applied successfully to a wide range of materials including metals, semiconductors, insulators and superconductors (Amoruso *et al.*, 1999). One of the processes expected for absorption of laser energy by the plume inside the hole, is that it subsequently causes a secondary drilling process, utilizing the absorbed energy (Abeln *et al.*, 1999; Treusch, 1985; Breitling *et al.*, 2003; Dausinger *et al.*, 1999). Laser energy absorbed by the vapour inside the hole gives additional heating and expansion of the vapour. The heat input by the vapour can keep the material longer in molten state, even after the laser pulse has ended. Furthermore, the extra heat input in the vapour is expected to increase the recoil pressure, which is beneficial for the ejection of molten material.

The effect of the plume depends strongly on the used power densities and the type of material removal process. For short pulses, at low power densities with material removal only by vaporization, the laser beam can be attenuated strongly by the plume resulting in a decrease of the processing speed. Song and Xu (1998) found in their experiments, at low power densities up to 0.5 GW/cm^2, that the plume absorbs a large amount of the energy in the laser beam. In contrast to this, the experiments described in this thesis are performed with long pulses at higher power densities in the range where melt ejection occurs up to 35 GW/cm^2. For these pulses, a significant amount of the laser beam energy reaches the target, as will be shown in the following chapters.

Chapter 3

Equipment and methods

In this chapter an outline is given about the working of the XeCl excimer laser that is used for the experiments. Furthermore, the target handling and the methods used for hole analysis are described.

3.1 The excimer laser

For the experiments described in this thesis an excimer laser, with a special design, is used. This laser emits a nearly diffraction limited beam. A more detailed description of this laser can be found in literature (Timmermans, 1995; Timmermans *et al.*, 2000; Hofstra *et al.*, 1997; Hofstra, 1999). Important for generating the laser beam are the characteristics of the lasing medium and the resonator configuration. Both subjects are discussed in this section.

3.1.1 Lasing medium

Excimer lasers are a special type of pulsed gas lasers that emit very energetic pulses lasting tens to hundreds of nanoseconds in the ultraviolet range of the electromagnetic spectrum. The word ”excimer” originally came from the term ”excited dimer,” meaning a pair of identical atoms which form only in the excited state a molecule. These excimer atoms are repulsive in the ground state. Nowadays, the term has been used in a more general manner to describe any diatomic or triatomic molecule that only exists in the excited state (these are properly termed ”exciplexes”). The most important group of these excimers for high power lasers is that of the rare gas halides. Table 3.1 lists examples of these species with their corresponding emission wavelengths. The excimers are ex-

Table 3.1: *The most important exciplexes used for excimer lasers with their corresponding emission wavelengths (Migliore, 1996)*

gas	λ [nm]
ArF	193
KrCl	222
KrF	248
XeCl	308
XeF	351

cellent lasing mediums, because a repulsive ground state only exists. There is a population inversion whenever molecules are formed in the excited state. With appropriate excitation this leads to high gain.

In almost all commercial excimer lasers the energy required to cause excitation is provided by an electrical discharge. The main part of the laser is the pressurised laser chamber sealed with windows to allow the beam to travel through and out of the laser medium, which is shown in figure 3.1. The laser chamber is filled with a gas mixture containing the rare gas and the halogen. An electrical discharge brings the atoms in a state where the excimer is formed. For repetition rates higher than 1 Hz it is necessary to refresh the gas between the discharge electrodes between two pulses (Migliore, 1996). In figure 3.1 a resonator is shown with two mirrors, one totally reflective mirror and one partially transmitting output mirror. The combination of the laser medium and mirrors is used to amplify the light, while the beam leaves the cavity through the output mirror. The resonator setup will be discussed in more detail in the following section.

The discharge of an excimer laser always becomes unstable after a while. Therefore, only pulsed operation is possible. The duration of the stable period of a gas discharge depends strongly on the starting conditions. Besides a homogeneous gas distribution a homogeneous electron distribution is necessary, to ensure simultaneous breakdown along the whole length of the discharge area. In this system is chosen for an x-ray pre-ionisation pulse, resulting in a homogeneous electron distribution (Timmermans *et al.*, 2000). During the stable period a glow discharge is formed. A general property of a glow discharge is its constant voltage across the electrodes almost independent of the current flowing through the discharge. During the steady state phase of the discharge, the electrical circuit can be described with an LC-circuit as shown in figure 3.2a. The capacitor of this main-pulse circuit, C_m, is charged with a voltage, which is twice the steady state voltage of the gas discharge for proper matching. Closing the switch results in a complete discharge of the capacitor in a single current pulse without oscillations. However, for the breakdown of the gas a higher voltage is needed, typically 4 to 6 times the steady state voltage. With a circuit as shown in figure 3.2a these two demands can never be fulfilled simultaneously. Either the voltage on the capacitor is too low, resulting in a poor breakdown of the gas, or the voltage is too high, resulting in oscillations of the current. Nevertheless, most commercial excimer lasers use only such a circuit. The discharge in such lasers becomes quickly unstable which limits the pulse duration.

For the high beam quality of the laser used in the experiments, a certain number of optical roundtrips is necessary. This can be obtained with a discharge with a relative long stable period, which is realised with a pre-pulse circuit as shown in figure 3.2b. Discharge of the pre-pulse circuit capacitor C_p results in a high voltage (figure 3.3) with a very fast rise time for homogeneous breakdown of the laser gas. Subsequently the main-pulse circuit is used to deliver the main part of the pulse energy under matched conditions to sustain the discharge (figure 3.3). In this way, the discharge can be kept stable for 400 ns resulting in optical pulses of 200 ns with excellent beam quality.

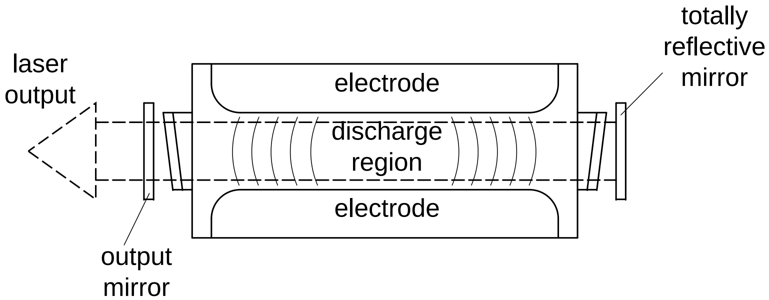

Figure 3.1: *Schematic drawing of the discharge area.*

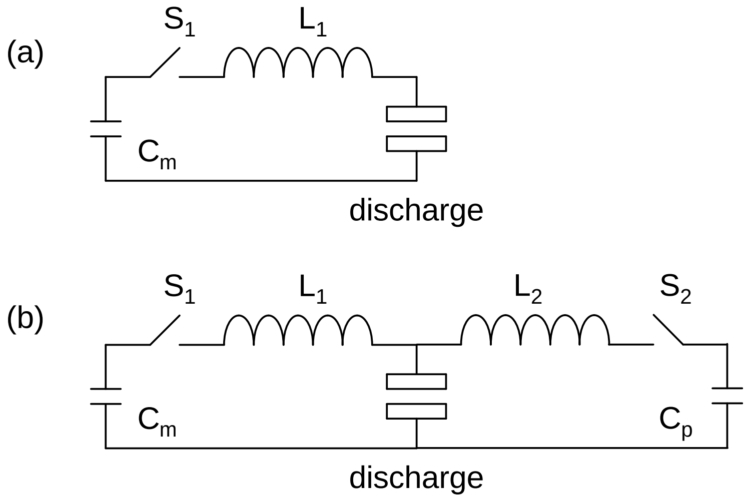

Figure 3.2:
a.) *The main-pulse circuit, to sustain the discharge during the steady state.*
b.) *Pre-pulse circuit added to the main-pulse circuit of figure a, to obtain homogeneous breakdown of the laser gas.*

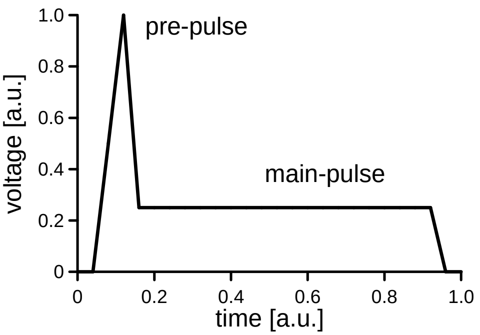

Figure 3.3: *Schematic curve of the voltage over the electrodes with the pre-pulse and the main-pulse.*

3.1.2 Resonator configuration

The used resonator configuration is described in this section, together with the focussing of the obtained laser beam. A laser basically consists of a laser medium inside a resonator. This medium determines the maximum energy output. The resonator however, is important for the spatial beam quality, which should be as good as possible for efficient drilling.

In figure 3.1 a resonator configuration is shown with two mirrors. The beam leaves the cavity through the output mirror. In section 3.1.1 was mentioned that the discharge of most commercial excimer lasers becomes quickly unstable which limits the pulse duration. The pulse duration of such a laser is typically 20 ns, which means, with a resonator length in the order of 1 meter, that the generated ultraviolet light performs only a few roundtrips. During these roundtrips the light has to be amplified from the level of weak spontaneous emission to the output level of the laser. After every roundtrip, the distinction between the power density level of the laser modes increases. The lowest order mode is strongly amplified, while the amplification of the higher order modes is orders of magnitude lower due to the high losses. As a result of the limited number of roundtrips, the spatial beam quality of standard excimer lasers with short pulse duration and high gain is rather poor. It actually means that the beam is difficult to focus to a tiny spot and high power density. To obtain a high beam quality the duration of the gain is 10 to 20 times the duration of the gain of standard excimer lasers, while the magnitude of the gain is reduced (for information about standard excimer lasers, see Basting (2001)). This enables an increased number of roundtrips of the ultraviolet light in the resonator, which results in a high beam quality.

For this particular XeCl excimer laser (λ = 308 nm), many resonator configurations are possible as described by Hofstra et al. (1997; 1998; 1999). A stable resonator configuration is used in the experiments. More general information about resonators can be found in literature (Siegman, 1986). The plano-concave stable resonator as shown in figure 3.4 consists of a concave mirror M_1 with a radius R_1 of 10 m and a plane mirror M_2. The resonator length L is 1.9 m. An aperture in the resonator suppresses building up of higher order transverse modes resulting in a Gaussian beam. This resonator configuration

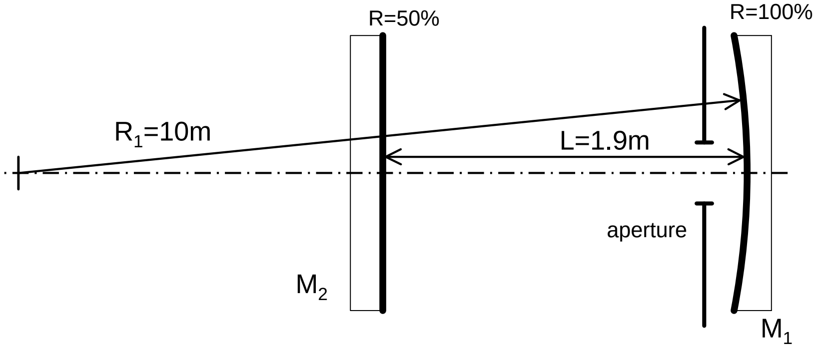

Figure 3.4: *Stable resonator with concave mirror M_1 and plane mirror M_2*

is chosen because of the relative easy mathematical description of a Gaussian beam. The power density distribution after focussing of this laser beam is calculated on basis of the calculated and measured beam properties.

The beam waist is defined as the plane where the beam has the smallest diameter and a plane wave front. The waist is located on the outcoupling mirror M_2 (Siegman, 1986). The corresponding waist radius w_0, at which the power density is $1/e^2$ of the peak value, can be calculated with the given resonator parameters to be

$$w_0^2 = \frac{L\lambda}{\pi}\sqrt{\frac{R_1}{L} - 1} \Rightarrow w_0 \approx 620\,\mu\text{m}. \tag{3.1}$$

The divergence, the far-field half-angular spread θ_d, is

$$\theta_d = \frac{\lambda}{\pi w_0} \approx 160\,\mu\text{rad}. \tag{3.2}$$

The Rayleigh range z_R describes the distance that a collimated beam travels before the beam begins to diverge significantly (Siegman, 1986)

$$z_R = \frac{\pi w_0^2}{\lambda} \approx 4\text{ m} \tag{3.3}$$

The near field beam profile behind the oscillator is measured by imaging the laser beam on a scintillator and with an image intensified CCD camera. The beam power is attenuated to $\approx 1\%$ before it reaches the scintillator. A typical measured beam profile is shown in figure 3.5a. The radial power density distribution

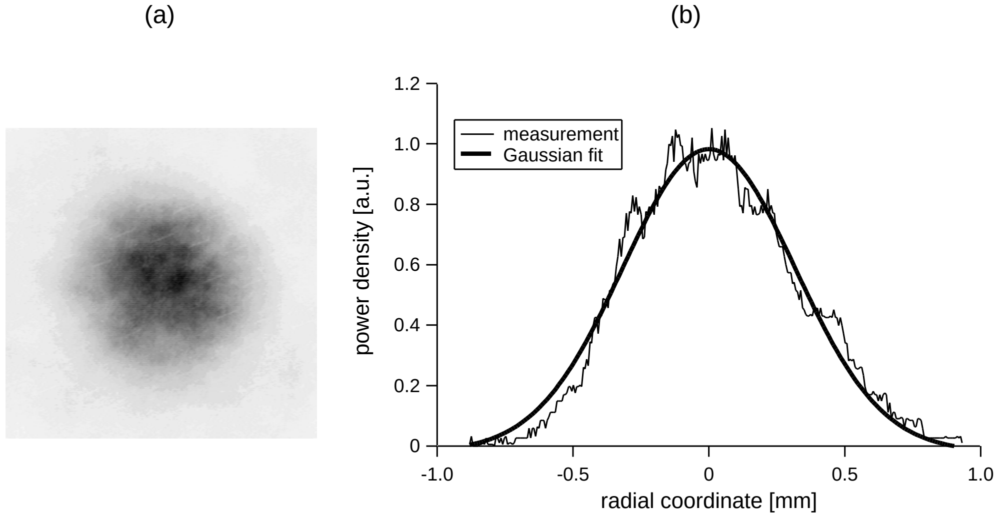

Figure 3.5: *The measured near field beam profile obtained with the plano-concave stable resonator from figure 3.4.*
a.) The beam profile.
b.) The radial power density distribution with a Gaussian fit.

together with a Gaussian fit is plotted in figure 3.5b. There is a good agreement between the measured beam diameter and the calculated value of equation 3.1. The spot diameter is nearly constant up to a few meters behind the outcoupling mirror according to the calculated value of the Rayleigh range in equation 3.3. The temporal pulse shape is measured with a high-speed photodiode. The measured pulse duration is typically about 175 ns long as shown in figure 3.6.

Although the measurements show that the generated beam has indeed maximum (diffraction limited) beam quality, the stable resonator configuration with

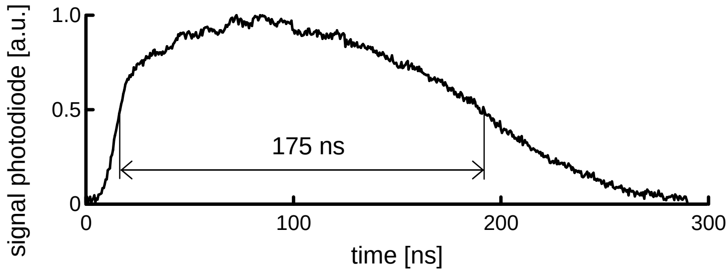

Figure 3.6: *Measured temporal shape of the laser pulse with 175 ns length (Full Width at Half Maximum, FWHM). This pulse is obtained with the plano-concave stable resonator of figure 3.4.*

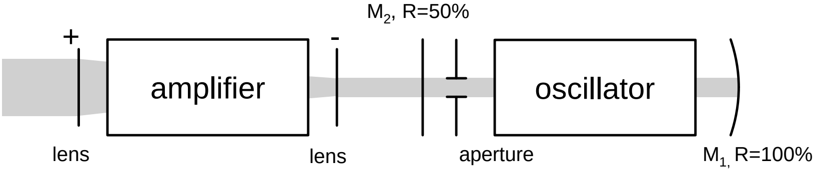

Figure 3.7: *Master Oscillator Power Amplifier (MOPA) setup, using two identical XeCl gas-discharge systems.*

an aperture, results in low pulse energy. To significantly increase the pulse energy, while maintaining the high beam quality, the pulse power is amplified by a so called Master Oscillator Power Amplifier (MOPA) setup, by using a second identical XeCl gas-discharge system. This setup is shown in figure 3.7. Before amplification, the beam from the Master Oscillator is expanded 6.5 times to match it to the size of the gain region of the Power Amplifier. This is done to extract more energy from the amplifying medium before saturation (McKee, 1991). With this step the pulse energy is amplified from 1.5 mJ to 30 mJ without noticeably influencing the pulse duration. The pulse shape is about the same after amplification in the Power Amplifier.

The laser beam is focussed to a small spot. The properties of the beam around this spot are calculated. For the experiments, in which only the oscillator is used, the beam is focussed with a lens with a focal length of 100 mm. The laser beam from the MOPA setup is focussed with a lens with a focal length of 500 mm. The radial power density distribution of a Gaussian beam remains Gaussian after focussing and is

$$I\left(r\right) = \frac{2P}{\pi w^2} e^{-2r^2/w^2} \tag{3.4}$$

where w is the beam radius, I the power density, P the pulse power and r the radial coordinate. The $1/e^2$ spot diameter in the focus d_0 is for a Gaussian beam (Siegman, 1986)

$$d_0 = \frac{4\, f \lambda}{\pi\, D} \tag{3.5}$$

where f is the focal length of the lens and D is the incoming beam diameter. The resulting diameters are given in table 3.2 which shows a similar spot diameter in the focus for both setups. Information about the propagation of the laser beam around the waist is given by the Rayleigh range, given in table 3.2, analogous to equation 3.3. The properties of the beam in the focus region determine to a large extent the geometrical properties of the drilled holes, e.g. the diameters of the holes at the laser beam side of the target, drilled with a power density just above

Table 3.2: *The focal length f, the spot diameter of the focus d_0, the Rayleigh range z_R, the pulse energy E_{puls} with the standard deviation of the pulse energy σ_n, the power P and the power density I_{1/e^2}, which is the average power density over the $1/e^2$ spot diameter of the focus, and the maximum power density I_0, which is the power density at the optical axis in focus at r=0.*

	oscillator	MOPA
f [mm]	100	500
d_0 [μm] (equation 3.5)	32	25
z_R [mm]	2.6	1.6
E_{puls} [mJ]	1.5	30
σ_n [%]	5	10
P [kW]	9	171
I_{1/e^2} [GW/cm^2]	1.1	34.9
I_0 [GW/cm^2]	2.1	69.8

the melt ejection threshold, are similar to the calculated spot diameter. The pulse power, which will be mentioned for the experimental results in the following chapters, is obtained by dividing the pulse energy by the pulse duration. The power density is calculated by dividing the pulse power by the $1/e^2$ spot area of the focus. The calculated pulse power and the power density for the 175 ns pulse are shown in table 3.2.

3.2 Target handling

The experiments are done mainly with metals as target material. Pure metals are used as foils ranging from 25 to 500 μm in thickness. Alloys are used in the range from a half up to a few millimetres in thickness. Thin foils are mounted in a slide frame, to ensure flat clamping. The targets are used as delivered and cleaned with ethanol before drilling. The targets are rigidly clamped. Depending on the experiment, the targets are positioned horizontally or vertically, but the influence of the gravitational forces on the process is negligible. The target is placed with respect to the focus of the laser beam at the position where the minimal number of pulses is necessary for drilling through the target. With this procedure, the focus of the laser beam is at approximately a fourth of the target thickness below the surface. In most of the experiments, holes are drilled in targets placed in air at atmospheric pressure. Some experiments are done while blowing helium along the surface of the target.

3.3 Hole analysis

Different techniques are used for analysis of the drilled holes. Standard metallographic techniques are used to generate cross sections of holes. An example is shown in figure 3.8a. The surfaces are prepared by grinding with increasingly fine grit size. To make the structure visible, the grinding is followed by polishing with an aluminium-oxide emulsion and etching, e.g., for carbon steel with a dilution of 3% nitric acid in ethanol. The polished surface has to coincide with the plane containing the axis of the drilled hole. To ensure this a cross section is made in a plane slightly skew with respect to a plane containing the axis of a row of holes. This method results in a cross section in the proper plane of at least one of these holes. Furthermore, for this hole the proper position of the cross section can be verified by comparing with the cross sections of the adjacent holes.

Targets are examined and imaged using a Scanning Electron Microscope (SEM) from which an example is shown in figure 3.8b and a variety of optical microscopes equipped with digital cameras from which an example is shown in figure 3.8c.

Some standard techniques could not be used because the holes are too small to perform accurate measurements. For example, the holes are to small for weighing the amount of removed material (Voisey *et al.*, 2002) or for x-ray study of the hole geometry (Karasev *et al.*, 1971).

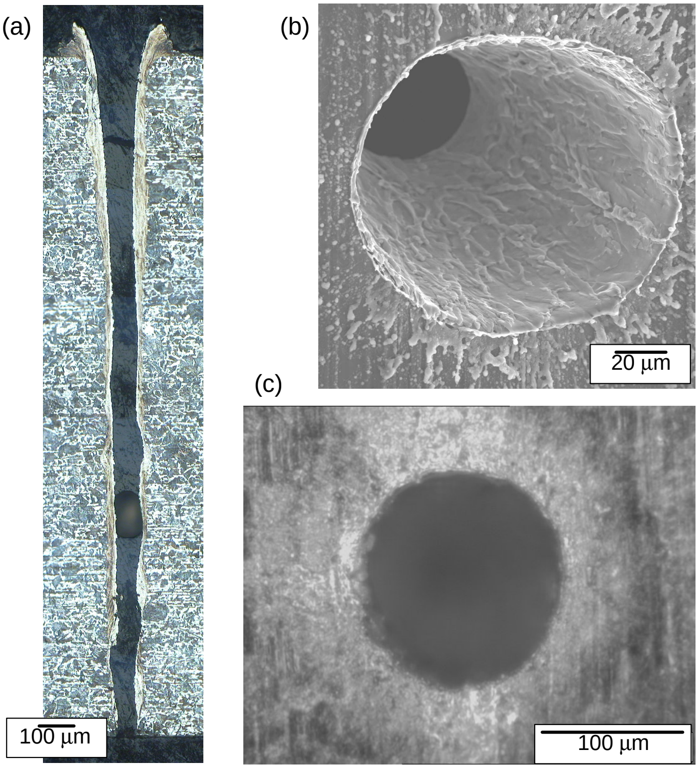

Figure 3.8: *Some examples of the used techniques for hole analysis.*

a.) *A cross section of a hole drilled in 2 mm steel.*

b.) *Scanning Electron Microscope (SEM) image made at an angle of 19° of a hole drilled in 125 μm aluminium foil.*

c.) *Image made with an optical microscope equipped with a digital camera of a hole drilled in 500 μm aluminium.*

Chapter 4

Influence of the pulse duration

The goal of the experiments described in this chapter is to study the influence of the pulse duration on hole drilling of metals. Previous studies found for metals (Chen and Liu, 1999; Dausinger, 2000) were done employing various types of lasers. The results are difficult to compare and interpret because they involve simultaneous variation of other laser parameters as well, instead of varying the pulse duration only. In the described experiments this is avoided by changing exclusively the pulse duration with a special developed pulse slicing technique to ensure an identical beam quality for all pulse durations. In the experiments holes are drilled in different metal targets, such as aluminium and nickel foils of 25 and 125 μm thickness. The amount of removed material is obtained for a range of pulse durations between 6 and 150 ns, and for a range of pulse energies between 0.01 and 10 mJ. The drilling experiments are done under normal laboratory conditions, without shielding gas. A low repetition rate of 0.1 Hz ensures that the repetition rate does not influence the drilling rate.

4.1 Experimental setup

The experimental setup shown in figure 4.1 allows to change independently both the pulse energy and the pulse duration. The energy is easily adjustable by using a set of attenuators. Adjustment of the pulse duration involves the combination of a number of optical components, which will be further explained in this section. The pulse shapes obtained with the pulse slicing method will be described in more detail and information will be given about data processing of the experimental results.

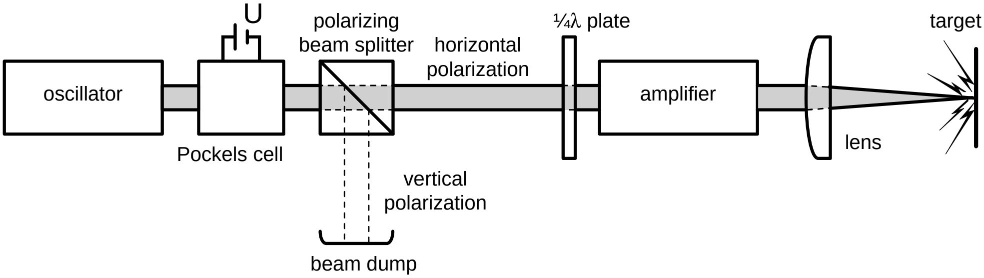

Figure 4.1: *Pulse slicing with a Pockels cell, which enables slicing pulses with durations in the range of 5 to 150 ns out of a 175 ns long laser oscillator pulse all with exactly the same beam quality.*

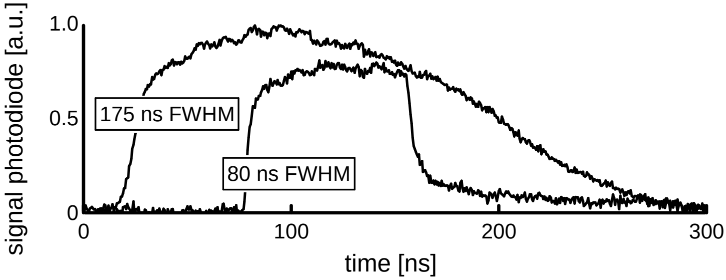

Figure 4.2: *An 80 ns pulse sliced out of a 175 ns pulse.*

4.1.1 Pulse slicing method

The MOPA setup which was described in section 3.1.2 and shown in figure 3.7 is used to obtain a Gaussian output beam. A Brewster-window is placed inside the resonator to obtain a linear polarization of the oscillator output beam as required for the pulse slicing technique. Behind the oscillator the beam is sent through a Pockels cell, which rotates the plane of polarization $\frac{1}{2}\pi$ radians when the proper half-wave voltage is applied (Hecht, 1998) (figure 4.1). Pulse slicing is done by a polarizing beam splitter behind the Pockels cell which transmits the rotated polarization, while any other polarization, e.g., as produced when no voltage is applied, is dumped sidewards. The switching time for the Pockels cell is limited by the speed of the high-voltage switching electronics to about 2 ns, which determines the fastest rise and fall time and also the minimum duration of a sliced pulse to about 5 ns. To ensure that the holes are drilled with circularly polarized light a quarter-wave plate is placed at the input side of the amplifier. Besides this, the quarter-wave plate prevents reflections from the target from entering the oscillator. The sliced pulse can be focused directly or can be amplified if a higher pulse energy is needed. A single lens is used to focus the beam. Further details about focusing of the beam were already given in table 3.2. The pulse shape behind the oscillator and amplifier is measured with high-speed photodiodes with 1 ns rise and fall time. Figure 4.2 shows an oscillator pulse of 175 ns and a pulse, sliced out the middle of this pulse, with a duration of 80 ns. This is done by switching the Pockels cell about 50 ns after the start of the 175 ns pulse. Note that the oscillator pulse ends with a ramp ranging from 175 to 300 ns. To slice pulses with an almost constant power during the pulse this ramp should be excluded. Therefore the pulse slicing method is employed to generate pulses with a maximum duration of 150 ns.

4.1.2 Power range for sliced pulses

The power of the sliced pulses is limited by the limited discrimination between the different planes of polarization of the polarizing beam splitter. Generally, after amplification a ’leaking’ power of about 1 percent of the power of the sliced pulse is observed. This may appear like a small amount, but it is observed that at high powers the ’leaking’ is higher than 1 percent and may contribute to the drilling process as well. This is due to amplification of the ’leaking’ power by, possibly a higher factor than the sliced pulse power, due to gain saturation effects at higher power densities (McKee, 1991). To avoid this ambiguity it is decided to restrict the power to values where the ’leaking’ power does not significantly influence the drilling process.

4.1.3 Pulse shapes

The pulse shapes which are used for the experimental results, are schematically shown in figure 4.3. For brevity, pulses with a duration of about 10 ns are called short pulses and pulses with a duration of about 100 ns are called long pulses. Figure 4.3a shows a long pulse with pulse duration t_a, power P_a and energy E_a. Figure 4.3b shows a pulse with the same amount of energy as the pulse of figure 4.3a ($E_b = E_a$, i.e. the same area), but with much shorter pulse duration t_b. Therefore the power of the short pulse of figure 4.3b is proportionally higher than of the long pulse of figure 4.3a. Figure 4.3c shows a short pulse with the same power as the long pulse of figure 4.3a ($P_c = P_a$, i.e. the same height). Therefore the energy of the short pulse in figure 4.3c is proportionally lower than of the long pulse of figure 4.3a. A fair comparison between drilling speeds of a long and short pulse may be made when both the power and the energy of the

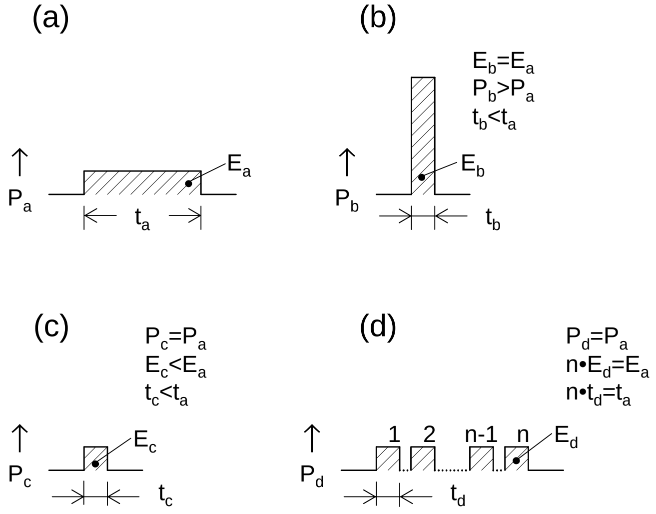

Figure 4.3: *Drilling with long and short pulses can be compared for equal pulse energy or equal pulse power. The pulse shapes for both situations are shown schematically (a,b,c). A single long pulse can also be compared with a series of short pulses with equal power and the same cumulative energy as the long pulse (d).*

pulses are similar, which is obviously not possible with single pulses of different duration. To do this, a long pulse is compared with a series of short pulses with the same power and the same cumulative energy. The pulse frequency is low enough to avoid interaction between the pulses. Such a series of pulses with a pulse duration t_d is shown in figure 4.3d in which $P_d = P_a$ and $n \cdot E_d = E_a$.

4.1.4 Data processing of the experimental results

A number of different quantities can be used to present the experimental results. The average drilled depths per pulse and the average removed volumes per pulse are obtained for different materials and thicknesses at different energies, powers, and pulse durations. The average drilled depth per pulse is obtained from the number of pulses required to drill through the foil. For pulse energies where penetration requires only a single or just a few pulses the average drilled depth might thus be underestimated, because the number of pulses can only be an integer number. The errors in the average drilled depth per pulse, resulting from this consideration, are shown by vertical error bars. To obtain the pulse power, the measured pulse energy is divided by the measured pulse duration. The pulse-to-pulse fluctuation of the energy was given in table 3.2, the maximum deviation in pulse duration for pulses around 9 ns is ±0.5 ns, and for

target	h [μm]	t_p [ns]	E_{puls} [mJ]	d_0 [μm]	P [kW]	I_{1/e^2} [GW/cm^2]
Ni	125	21, 78, 104, 150	0.05-10	25	0.5-100	0.1-18
Al	125	9,104	0.05-10	25	0.5-100	0.1-18
Al	25	9, 21, 48, 104	0.01-1	25	0.25-25	0.05-5
Fe	125	6-105	0.01-0.21	32	2.0	0.25
Cu	125	6-105	0.01-0.21	32	2.0	0.25
Ti	125	6-105	0.01-0.21	32	2.0	0.25
Ni	125	6-105	0.01-0.21	32	2.0	0.25
Al	125	6-105	0.01-0.21	32	2.0	0.25

Table 4.1: *Covered parameter range of the experiments presented in this chapter.*

pulses around 100 ns ± 2 ns. Therefore, the dominant contribution to the error in power originates from the pulse-to-pulse fluctuations in the energy, which results in an error of 5% for pulse powers up to 15kW and an error of 10% for amplified pulse powers higher than 15 kW. The fluence (J/cm^2) and power density or intensity (W/cm^2) at the target are both obtained from the measured pulse energy and the beam diameter as found in table 3.2. The relative error in fluence and power density is dominated by the pulse-to-pulse variation of the energy because the laser beam did not shown any significant beams size fluctuations. Thus the relative errors for fluence and power density equal the errors mentioned for energy and power.

4.2 Results and discussion

Holes are drilled with the experimental setup as described in the previous section. Table 4.1 shows the parameter range covered in the experiments for 125 μm nickel, aluminium, iron, copper, titanium, and 25 μm aluminium foil. In this table, h is the thickness of the target, t_p is the pulse duration, E_{puls} is the pulse energy, d_0 is the spot diameter in focus, P is the pulse power and I_{1/e^2} is the power density.

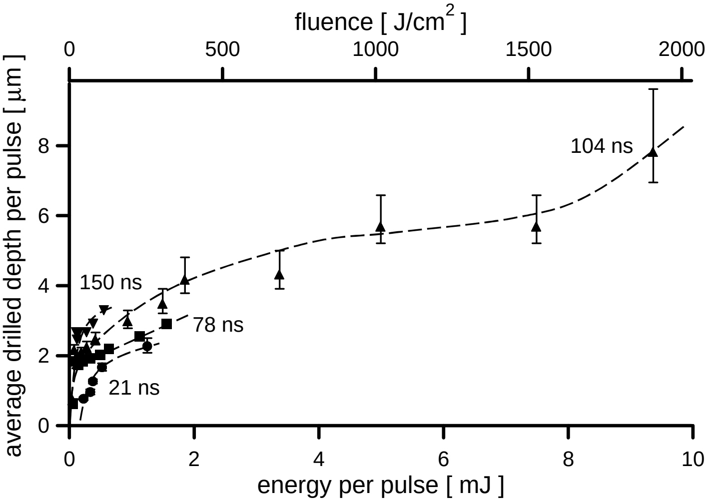

Figure 4.4: *The average drilled depth per pulse versus pulse energy for a foil of 125 μm thick nickel.*

4.2.1 Material removal

Removal in depth

Figure 4.4 shows the average drilled depth per pulse versus the pulse energy for 125 μm nickel foil. For a better clarity of the graph, error bars are shown only for pulse durations of 21 and 104 ns. It can be seen that the average drilled depth per pulse is larger for the long pulses than for the shorter pulses at the same energy. However, different pulse durations with the same pulse energy have different powers and are difficult to compare directly. For a better comparison the data of figure 4.4 is processed to obtain the average drilled depth per pulse versus the pulse power, as is shown in figure 4.5 for 125 μm nickel foil.

The results for 25 and 125 μm thick aluminium foil are shown respectively in figure 4.6 and 4.7. The observed effects for nickel and aluminium are similar. Because of this, the discussion will concentrate on the results of aluminium. The different measurement values for nickel and aluminium are likely due to the different material properties, especially the thermophysical properties, which will be discussed into more detail in chapter 6 that is about modelling of the drilling process. The experiments with nickel and aluminium foils show a rapid increase of the average drilled depth per pulse beyond a power of 0.5 kW, where the transition from the vaporization regime to the melt ejection regime

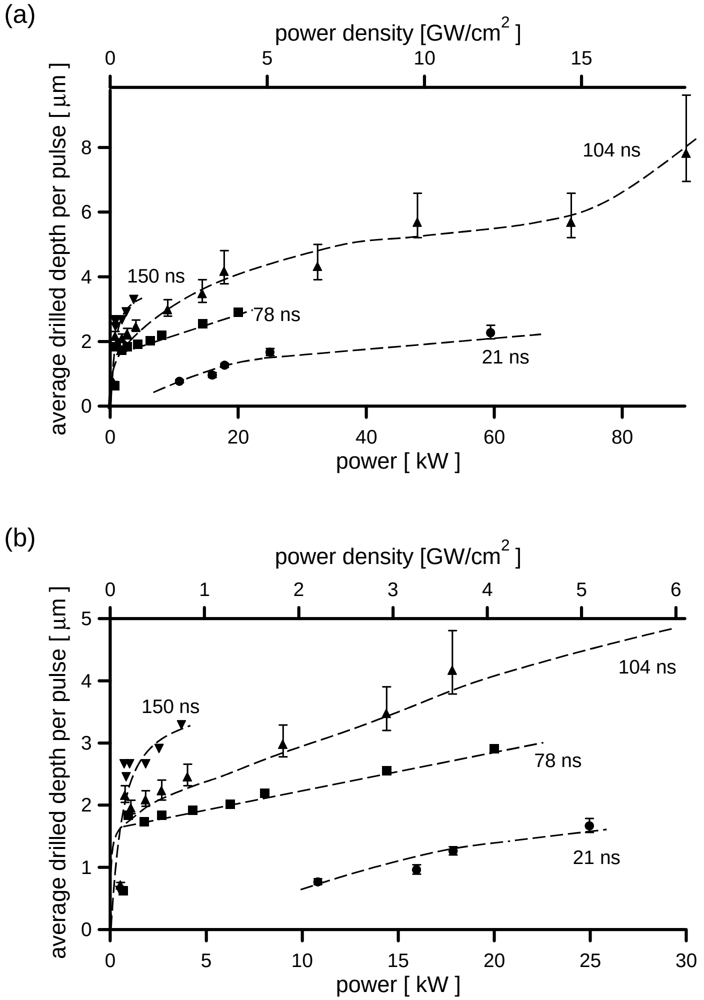

Figure 4.5:

a.) *The average drilled depth per pulse versus pulse power for a foil of 125 µm thick nickel is shown. This figure is obtained from the measurements as shown in figure 4.4. Vertical error bars are shown for the pulse duration of 21 and 104 ns.*

b.) *Section of figure 4.5a.*

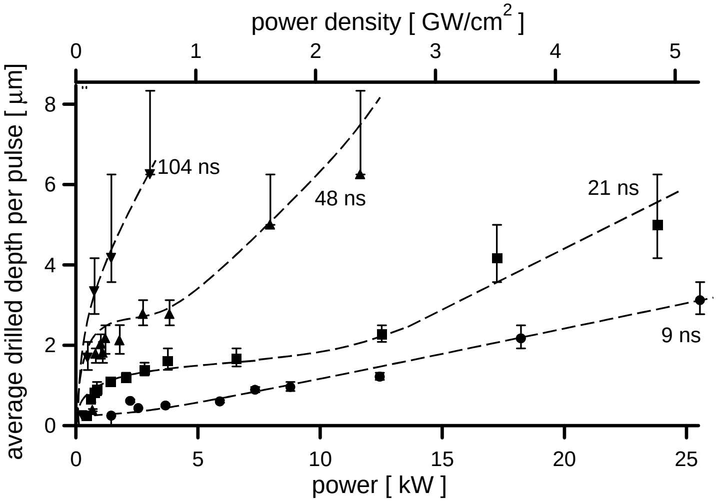

Figure 4.6: *The average drilled depth per pulse versus pulse power for a 25 µm thick aluminium foil. The pulse durations are 9, 21, 48 and 104 ns.*

is observed. In section 2.1 is stated that the drilled depth in the vaporization regime is in the order of 100 nm per pulse. When the process is dominated by melt ejection, like in the experiments described in this chapter, a much larger removed depth per pulse is reached with values from 1 to 100 µm.

The drilled depths are compared for different pulse durations. This is done with the help of figure 4.7 in which the average drilled depth per pulse for 125 µm aluminium is shown. The long 104 ns pulse removes, at a pulse power of 29 kW, 18 µm per pulse compared to the short 9 ns pulse removing 2.5 µm per pulse, which is a factor of 7 more. At the same power level and consequently different pulse energies the average drilling depth is higher for long pulses than for short pulses. However, the energy in the short pulse is lower than in the long pulse, thus comparing the drilled depth for a long pulse with a single short pulse is not appropriate. Therefore, a long pulse has to be compared with a series of short pulses as shown in figure 4.3d, where the power of the series of short pulses and the long pulse are the same and the series of short pulses contain the same cumulative energy as a single long pulse (4.3). For this comparison, in figure 4.7b the drilled depth is shown for a single short pulse and the series of 12 short pulses. It is shown that at the same power and the same cumulative energy a series of short pulses performs better with respect to drilling in depth, for which a possible explanation will be given at the end of this section.

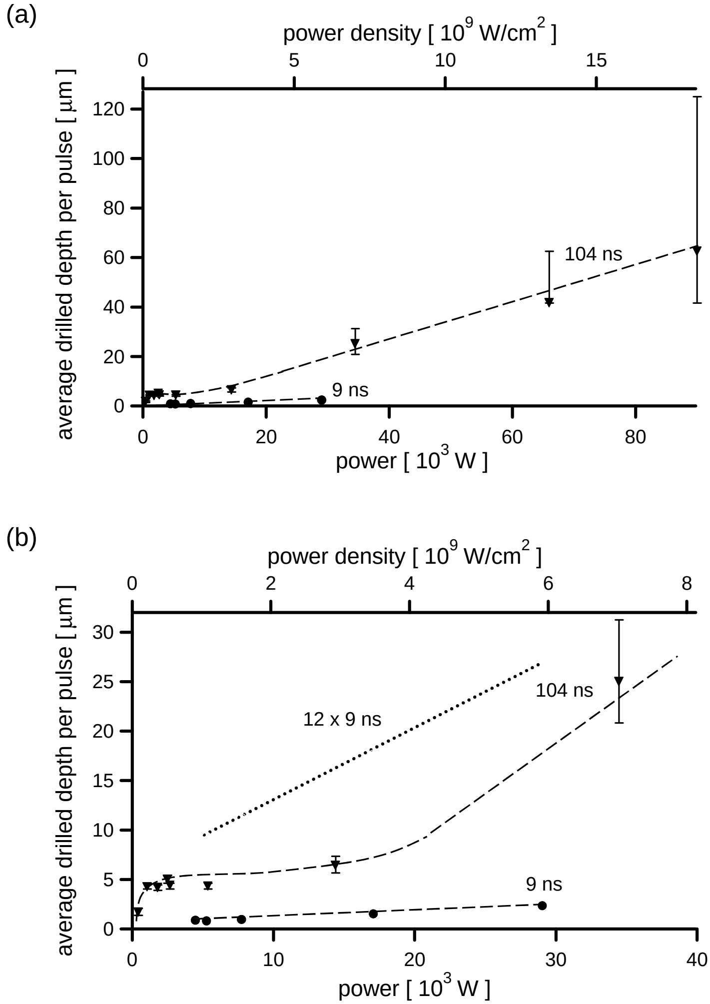

Figure 4.7: *Average drilled depth per pulse versus pulse power in a foil of 125 µm thick aluminium. The long pulses contain more energy. The dotted line shows the drilled depth for a series of 12 short pulses, with the same cumulative energy as a single long pulse.*

There seems to be a remarkable correlation between the hole diameter and the drilled depth per pulse. In figure 4.8 the diameters of the holes, measured at the top side of the foils, and the average drilled depths per pulse are shown for 125 μm thick nickel and aluminium. The measurements reveal that the average drilled depth is roughly constant from 20-65 kW for nickel and from 2-15 kW for aluminium as shown respectively in figure 4.8a and 4.8b. The diameter increases first with increasing power in that range with the constant drilled depth. But at powers above 65 kW and 15 kW for respectively nickel and aluminium the diameter decreases.

Two processes are expected to explain the drilling depth being nearly independent on the power in the range as shown in figure 4.8a and 4.8b. One of these processes is described by Semak *et al.* (2003). They introduced a model based on the melting threshold radius and the threshold time necessary for melt ejection for drilling with a Gaussian beam. Melt is only removed for melt ejection times shorter than the solidification time of the molten material. The melt ejection time is:

$$t_{ej} = \frac{r_m}{v_m} < t_m \tag{4.1}$$

where t_{ej} is the time for melt ejection from the melt pool, r_m is the melt pool radius, v_m is the melt velocity and t_m is the time between melting and solidification. Semak *et al.* (2003) show that the melt ejection threshold is almost equal to the melting threshold for drilling holes with a small diameter. Above the melting threshold the melt radius rapidly increases with increasing pulse power. The melt velocity also increases with increasing pulse power due to the higher recoil pressure. When the melt velocity increases proportional with the melt radius, the melt ejection time remains constant according to equation 4.1. No extra penetration depth is reached due to the constant melt ejection time and therefore the drilled depth remains approximately constant. The measurements in figure 4.8 show for the power range with roughly constant drilled depth per pulse, that the diameter of the holes increases strongly, which supports the proposed theoretical explanation. Simulations by Semak *et al.* (2003) based on the previously described experiments done for this thesis show reasonable agreement between their results and these measurements.

The second process that may lead to a constant drilled depth versus power is an increasing attenuation of the laser beam by the plume with increasing power, which results in a constant power at the target surface. The mechanism of attenuation of the laser beam by the plume was already described in section

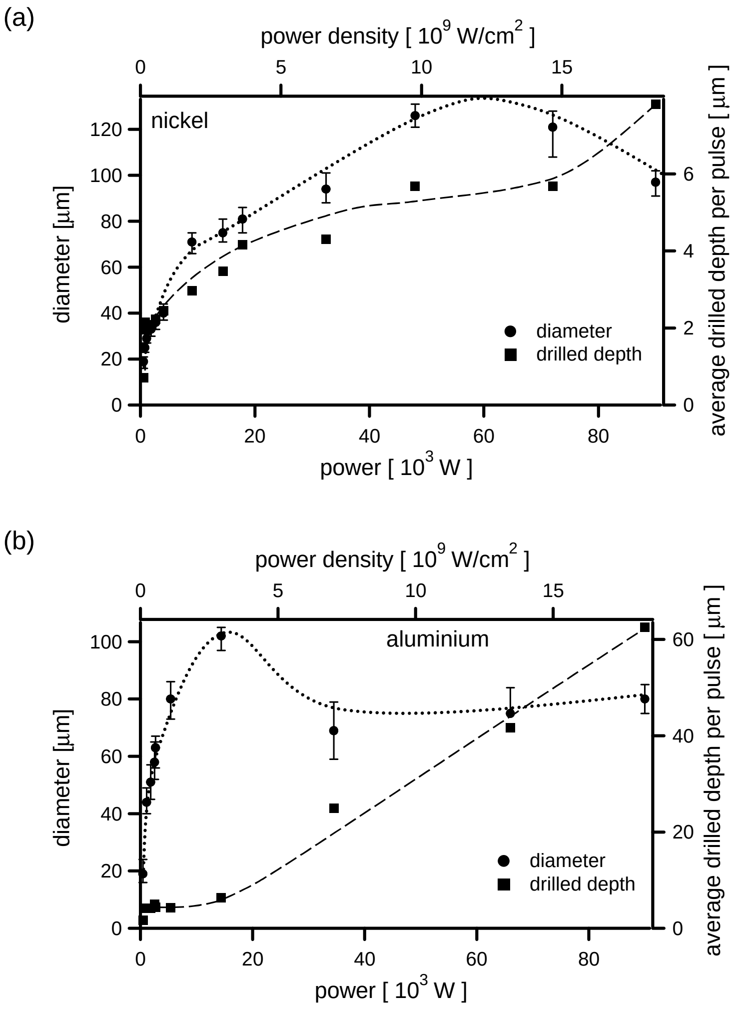

Figure 4.8: *The diameter of holes drilled with a pulse duration of 104 ns, measured at the top of the foil*
a.)   Holes drilled in 125 µm thick nickel.
b.)   Holes drilled in 125 µm thick aluminium.

2.4. In figure 4.7, however, can be seen that drilling with long pulses at power densities between 2 and 18 GW/cm^2 in the melt ejection regime does not lead to a decrease of the average drilled depth, indicating that for drilling with long pulses the beam energy is not strongly attenuated by the plume. A possible explanation for the absence of a strong attenuation in the experiments is that the plume absorbs laser energy and subsequently causes a secondary drilling process utilizing the energy absorbed by the plume. More about the role of the plume in the hole drilling process is found in chapter 5.

Removal of volume

For a similar description, in addition to the average drilled depth, the average removed volume per pulse is obtained. The SEM images in figure 4.10a and 4.10c show a larger diameter for the holes drilled with the long pulse than with the short pulse, which means that the removed volume can not be directly related to the drilled depth. Besides, it can be expected that the efficiency of the hole drilling process can be better described, for example, by the energy necessary per unit of removed volume, or per unit of removed mass. To obtain the removed volume, photographs of the beam entrance and exit side of the holes are made and the diameters of best-fit circles are measured (figure 4.8). The volume of the holes is then calculated by assuming cone-shaped holes having the measured entrance and exit diameters. In figure 4.9 the average removed volume per pulse versus the pulse power for 125 μm aluminium is shown. It can be seen that the long pulse removes, at a pulse power of 15 kW, $30 \cdot 10^3$ μm^3 per pulse compared to the short pulse removing $2 \cdot 10^3$ μm^3 per pulse, which is a factor of 15 more. Similar to the procedure described in comparing drilled depths a single long pulse is compared with a series of short pulses such that the power of the short pulses and the long pulse are the same and the series of short pulses contain the same cumulative energy as a single long pulse. In figure 4.9 the removed volume is shown for a series of 12 short pulses. In the figure is seen that for the same power the removed volume for a single long pulse is higher than for a series of short pulses.

Heat diffusion

A possible explanation for the observation that a series of short pulses drills deeper but a single long pulse removes more volume, when the pulse power and the energy are the same, is the following. The major amount of the material

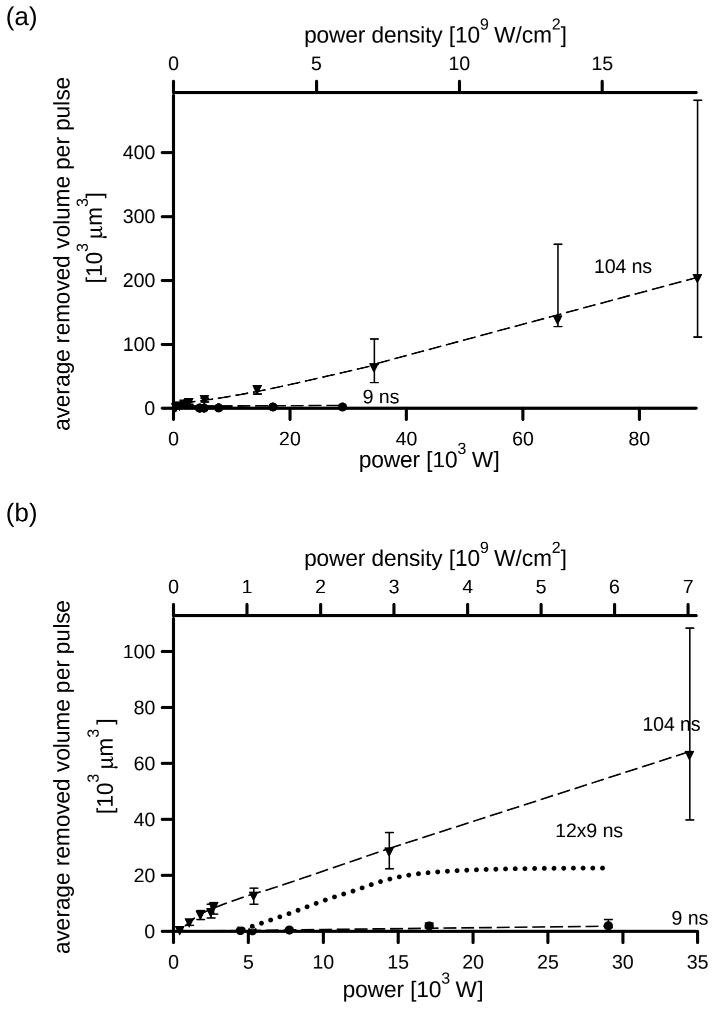

Figure 4.9:

- a.) *Average removed volume per pulse versus pulse power in 125 µm thick aluminium. Measurement points are shown for drilling holes with pulse durations of 9 and 104 ns.*
- b.) *Enlargement of figure a. The long pulses contain more energy. The dotted line shows the removed volume calculated for a series of 12 short pulses, with the same cumulative energy as a single long pulse.*

removed in each pulse is removed as melt and the major amount of the melt is ejected after the laser pulse, which is explained in further detail in chapter 5. When assuming that the melt layer will be completely ejected at the end of the laser pulse, the heat diffusion length can be considered as a qualitative measure for the drilled depth per pulse. Of course this is a very simple and idealized model, but it shows why it is expected that a series of short pulses drills deeper than a single long pulse. The heat diffusion length is approximately given by (Von Allmen and Blatter, 1995)

$$l_d(t) = 2\sqrt{at} \tag{4.2}$$

where $l_d(t)$ is the diffusion length, a is the thermal diffusivity and t is the diffusion time. Equation 4.2 shows that increasing the pulse duration 12 times gives an increase in diffusion depth of $\sqrt{12}$. Thus, it is expected that a single long pulse drills about a factor of $\sqrt{12}$ deeper than a single short pulse with the same power. For a series of 12 short pulses, with the same power and the same cumulative energy as a single 12 times longer pulse, the drilled depth would be roughly 12 times the drilled depth of a single short pulse. So, the series of short pulses will drill deeper than the long pulse on the basis of this simple model. On the other hand, the removed volume is larger for a single long pulse than a series of short pulses with similar power and cumulative energy. This is because the hole diameter for the long pulses is larger than for the short pulses. The reason for this could be the longer interaction time for both, the beam energy directly irradiating the target and for the laser energy absorbed by the plume.

4.2.2 Hole quality

The hole quality is the most important processing goal for most applications. In figure 4.10 SEM images of some typical holes are shown, which reveal a largely different quality. Figure 4.10a shows a hole drilled with a long pulse. Figure 4.10b shows a hole drilled with a short pulse with approximately the same energy ($\approx$ 0.2 mJ) as in a long pulse used to drill the hole in figure 4.10a, such that the power is accordingly higher. Figure 4.10c shows a hole drilled with a short pulse, but with approximately the same pulse power as the long pulse used to drill the hole of figure 4.10a, such that the pulse energy is accordingly lower. It can be seen that the hole diameter is smaller for the holes drilled with the short pulse. Also it can be seen that the hole quality is best for a long pulse with a power of 15 kW (figure 4.10d). Melt droplets are clearly visible in and around the holes of figure 4.10, thus the experiments obviously fall into the

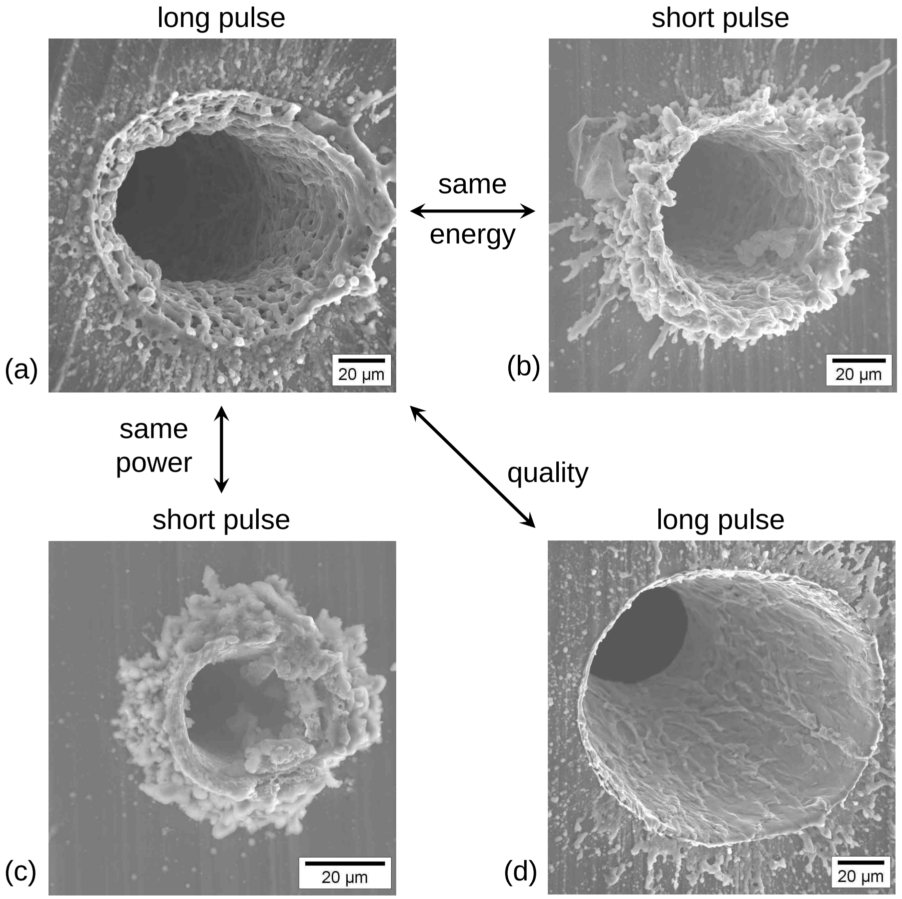

Figure 4.10: *SEM-pictures of holes drilled in 125 μm aluminium viewed at an angle of 19°.*
a.) Hole drilled with 104 ns pulse duration (pulse energy: 0.19 mJ, pulse power: 2kW).
b.) Hole drilled with 9 ns pulse duration (pulse energy: 0.26 mJ).
c.) Hole drilled with 9 ns pulse duration (pulse power: 5kW).
d.) Hole drilled with 104 ns pulse duration with better hole quality (pulse energy: 1.5 mJ, pulse power: 15 kW).

power regime where melt expulsion occurs as was mentioned above. Actually, such melt expulsion is expected to be the most efficient process for material removal because the energy per unit of mass required for melting is considerably less than for vaporization (Voisey *et al.*, 2002). Figure 4.10a, 4.10b, and 4.10c show that using a longer pulse improves the hole quality compared to a short pulse with the same pulse energy or power. Optimization for hole quality shows the best results for long pulses with higher pulse power (15 kW, figure 4.10d.).

4.2.3 Comparing different materials

As was argued in the end of section 4.2.1, the thermal diffusivity enables a qualitative comparison for the obtainable drilled depth per pulse in the lowest power range where the melt ejection process has fully developed. This assumption will be illustrated and further strengthened by experiments described in the following, in which holes are drilled in materials with different heat diffusion coefficients at a constant power and with a range of pulse durations. The used power is relative low compared with the experiments shown previously, e.g. those of figure 4.7, which has the expected advantage that minimal attenuation of the laser beam by the plume would occur. The low power is experimentally realized by using only the oscillator beam as described in section 3.1.2 for which further details are given in table 3.2. It is important to note that processing different materials results in a different absorbed fraction of energy A, i.e. although the power of the laser beam is constant, the absorbed laser power can be different for each material. In the experiments, iron, copper, titanium, nickel, and aluminium are examined. The average drilled depth per pulse versus the pulse duration for the examined materials is shown in figure 4.11. This figure shows that in these experiments the melt ejection process is fully developed for pulse durations longer than 25 ns, from which the drilled depth per pulse increases approximately linear with the pulse duration.

For a basic comparison between different materials with the simple model, equation 4.2 is used to calculate the heat diffusion lengths, which are shown in figure 4.11. It can be seen that the diffusion length tends to give an overestimation for Cu. Further, it can be seen that the experimentally drilled depth increases stronger with increasing pulse duration than the diffusion length. A reason for this is the significant amount of melt, leaving the hole before the end of the laser pulse, as will be investigated with a detailed numerical model in chapter 6, section 6.3.3. In essence, the diffusion length gives a first qualitative comparison

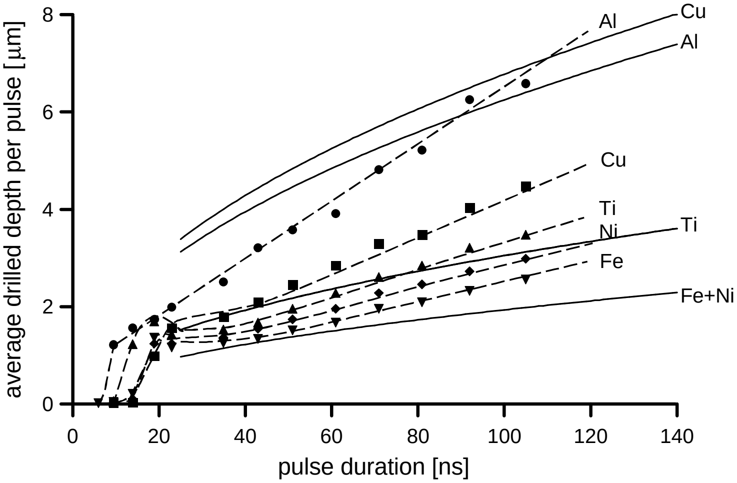

Figure 4.11: *Experimental results of drilling different materials, at a laser power of 2 kW and a power density of 0.25 GW, with a range of pulse durations. The calculated diffusion lengths are shown by the solid lines.*

of processing different materials, but seems not appropriate for a good understanding of the entire drilling process, especially when studying the influence of variations in power and pulse duration.

4.3 Summary and conclusions

It is shown that drilling of metals with a long pulse duration, high beam quality excimer laser is possible with respect to high drilling efficiency and high quality of the manufactured holes. The influence of the pulse duration on the drilling process is studied. This is done by using a pulse slicing method, which can provide a freely adjustable pulse duration while all other laser parameters, particularly the beam quality and shape, remain unchanged. The experiments are done in the power regime where melt expulsion occurs. Melt expulsion is expected to be the most efficient process for the material removal because the energy required for melting is less than for vaporization. It is shown that with a long pulse the drilling speed during the pulse is lower, but on the other hand, the removed volume is higher. The experiments indicate that for drilling with long pulses at higher power densities, the laser beam is not strongly attenuated by the plume. This could be caused by the following reasons or a combination of these. The first reason may be that for drilling with long pulses at these power densities, no strong absorption or scattering by the plume is present. The second reason may be that at high power densities the laser energy absorbed by the plume subsequently causes a secondary drilling process. In the power range used in the experiments drilling with long pulses gives a significant better hole quality than drilling with short pulses. From these experiments it is concluded that with the same power or the same energy a long pulse removes more material than a short pulse.

Chapter 5

Material removal mechanism

This chapter describes the temporal aspects of material removal during laser drilling and addresses the issue of the transparency of the plume for the drilling laser beam. A shadowgraphic imaging technique is used to study these topics. For aluminium and Hastelloy X shadowgraphic images are recorded of the material removal at times between 0 and 200 μs, which is up to 1000 times longer than the pulse duration. The material removal showed respectively vaporization, shockwave expansion and melt ejection. The transparency of the plume is studied by shadowgraphic imaging during the laser pulse for drilling of aluminium, copper, Hastelloy X, iron, nickel, titanium, alumina and silicon. The aluminium and titanium plumes are not fully transparent for the laser beam, but the other examined target materials showed a highly transparent plume between the target and the shockwave.

5.1 Experimental setup

The setup described in section 3.1.2 and shown in figure 3.7 is used to obtain a Gaussian beam. Further details of this setup were given in table 3.2. The beam energy is adjusted by using attenuators. The average power densities over the $1/e^2$ focus diameter are in the range from 1.1 to 34.9 GW/cm^2. The targets for hole drilling are placed under normal incidence in air at atmospheric pressure. Occasionally, other gasses are used. In this section the system used for shadowgraphic imaging is described.

The experimental configuration for shadowgraphic imaging is shown in figure 5.1 (Schittenhelm *et al.*, 1998; Breitling *et al.*, 1999; Yoo *et al.*, 2000;

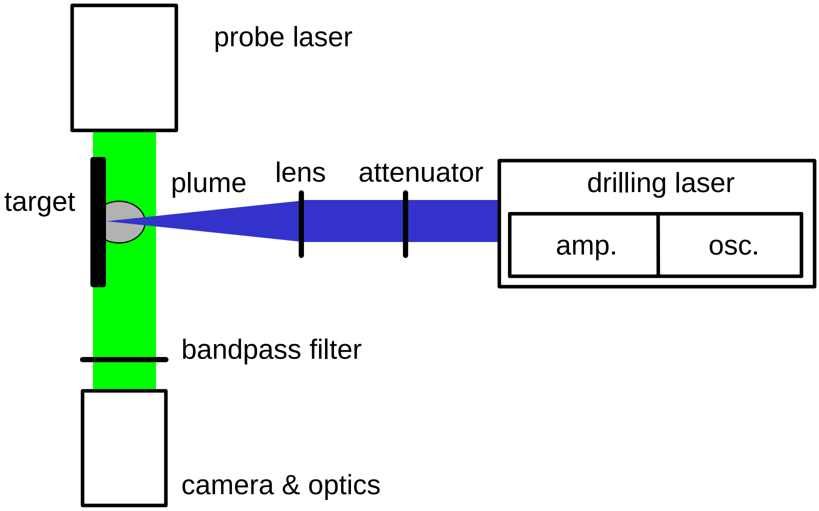

Figure 5.1: *The experimental setup for shadowgraphic imaging.*

Kokai *et al.*, 1999). For imaging a gated, intensified-CCD camera is used with a gate time of 10 ns. The camera is equipped with a microscope objective to image an area of 1 by 1 mm. The plume is illuminated with a probe beam, which is aligned parallel to the target surface and traversed the plume. The ejected material consisted of vapour, clusters formed by vapour condensation, and melt droplets (Yoo *et al.*, 2000; Schittenhelm *et al.*, 1996). This material can either absorb or scatter the probe beam and create a 'shadow' in the image. A bandpass filter, transparent for the wavelength of the probe beam, suppresses background illumination, which is caused mainly by the broadband light emitted by the hot plume.

Table 5.1: *Parameters used in the experiments.*

drilling λ [nm]	probe λ [nm]	time	material
308	308	during pulse	Al, Cu, Fe, Ni, silicon, Ti, alumina, Hastelloy X
308	532	during and after the pulse	Al, Hastelloy X

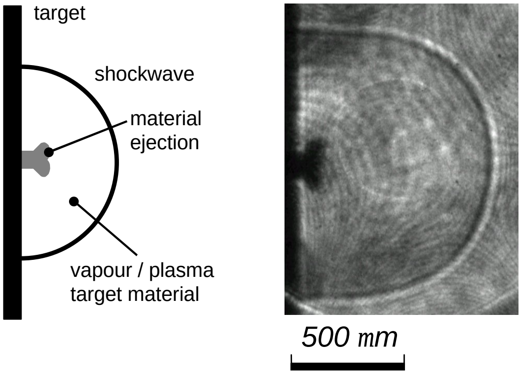

Figure 5.2: *A schematic view of a shadowgraphic image with the target on the left. The beam irradiates the target from the right. An example of a shadowgraphic image is shown, recorded with a probe laser wavelength of 532 nm at 500 ns after the start of the drilling pulse, for an aluminium foil. The residual concentric interference patterns are caused by spurious reflections of the used optics and provide no information about the process.*

Two probe beams with different wavelengths have been used. To study the transparency of the plume during and shortly after the drilling pulse a probe beam is used that is split off the 308 nm XeCl drilling beam. Therefore, it can be used only for imaging up to 350 ns after the start of the drilling pulse. To study the material removal at longer times, up to 200 μs after the start of the drilling pulse, a frequency doubled pulsed Nd:YAG laser is used as a probe laser with 532 nm wavelength, 50 μJ pulse energy, and 35 ns pulse duration.

A series of drilling pulses is used to drill a hole. Of this series of pulses, the camera can record only a single image per drilling pulse. With this setup, two sets of images are recorded. For the first set, images are recorded, at a fixed pulse in the series of pulses, for successive times after the start of the drilling pulse, e.g. images recorded at the second drilling pulse at 100 ns, 200 ns, 300 ns et cetera. For the second set, images are recorded at a fixed imaging delay for successive pulses, e.g. images at 100 ns for every pulse of the series of drilling pulses until break-through. Table 5.1 gives an overview of the most important parameters and the studied materials.

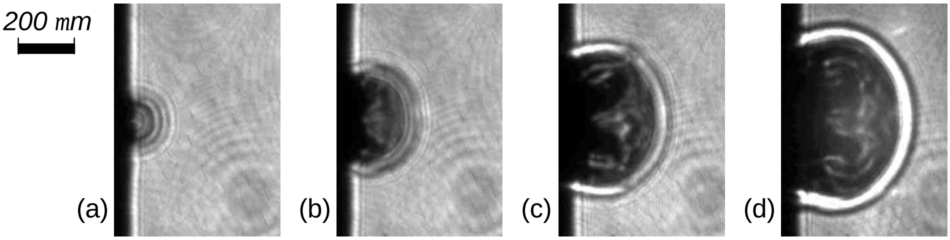

50 ns 150 ns 250 ns 350 ns

Figure 5.3: *Shadowgraphic images at different imaging delays after the start of the drilling pulse recorded with a 308 nm probe laser wavelength. For drilling through the 125 μm thick aluminium foil, 12 pulses are needed with a power density of 1.1 GW/cm^2. Images of the 1st drilling pulse are shown.*

5.2 Results and discussion

5.2.1 Plume development

The recorded pictures, such as in figure 5.2 and 5.3 show that the drilling process qualitatively proceed as follows. The material is heated by the laser irradiation and starts first to melt and then vaporizes. Heating the material at a high power density produces a strong vapour flow, which expands at a high speed. Therefore the surrounding gas becomes strongly compressed and heated by the expanding vapour (Bäuerle, 2000). Consequently a shockwave is formed. Changes in refractive index cause interference patterns, which visualise the shockwave (Breitling *et al.*, 1999).

Shadowgraphic images are recorded during drilling of 125 μm thick aluminium foil with a probe laser wavelength of 308 nm. These images are shown in figure 5.3. The expansion of the shockwave is clearly seen. The shockwave radii are measured at successive times and are shown in figure 5.4. The expansion of the shockwave may be described by a linear function for times between 50 and 350 ns after the start of the drilling laser pulse. The velocity of the shockwave for these times is estimated from figure 5.4 to be 800 m/s.

5.2.2 Transparency of the plume for the drilling beam

Absorption or scattering of the laser beam can influence the energy distribution in material processing. To investigate this, the transparency of the plume is studied by shadowgraphic imaging with the same probe laser wavelength and

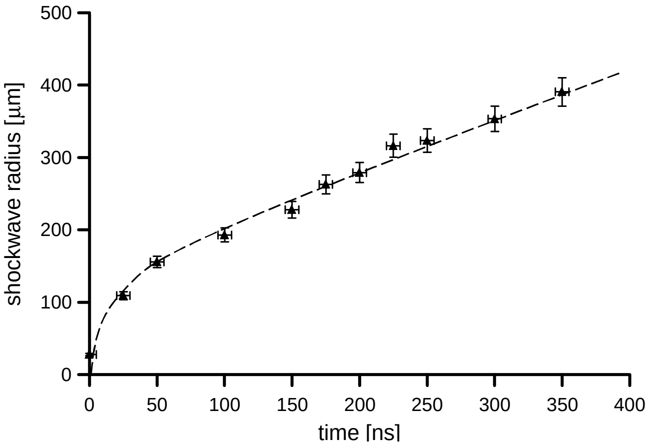

Figure 5.4: *The shockwave propagation distances at different times of the* 1^{st} *pulse during drilling of 125* μ*m thick aluminium foil with a power density of 1.1 GW/cm*^{2}.

drilling laser wavelength, i.e. 308 nm, because then a shadow in the image directly indicates that the plume is not fully transparent for the drilling wavelength.

Absorption by the plume

Shadowgraphic images, recorded at the end of the drilling pulse at 200 ns, are shown for different materials in figure 5.5. For each material in figure 5.5 the target and the shockwave are clearly visible. Remarkable is the dark area between the target and the shockwave during drilling of aluminium, alumina and titanium in respectively figure 5.5a, 5.5b and 5.5h. An explanation is absorption of the probe laser beam by the target material vapour, because aluminium and titanium have an absorption line at or close to the laser wavelength (Schittenhelm *et al.*, 1998). A free running XeCl oscillator emits mainly at 307.95 nm and 308.20 nm with line widths of 0.12 nm (Hofstra *et al.*, 1999). At one of the laser lines, neutral aluminium atoms have a strong absorption line at 308.22 nm (Handbook of Chemistry and Physics). Close to the other laser line, single ionised titanium has a strong absorption line at 307.86 nm. It is expected that there will be an overlap at high temperature and pressure due to broadening, of the titanium absorption line and the laser line. The images of aluminium and titanium show that the shockwave propagates closely in front of the target vapour. For the other investigated target materials (copper, iron, Hastelloy X, nickel, and silicon) the region between the target and the shockwave appeared transparent at the probe laser wavelength of 308 nm. Obviously, for these mate-

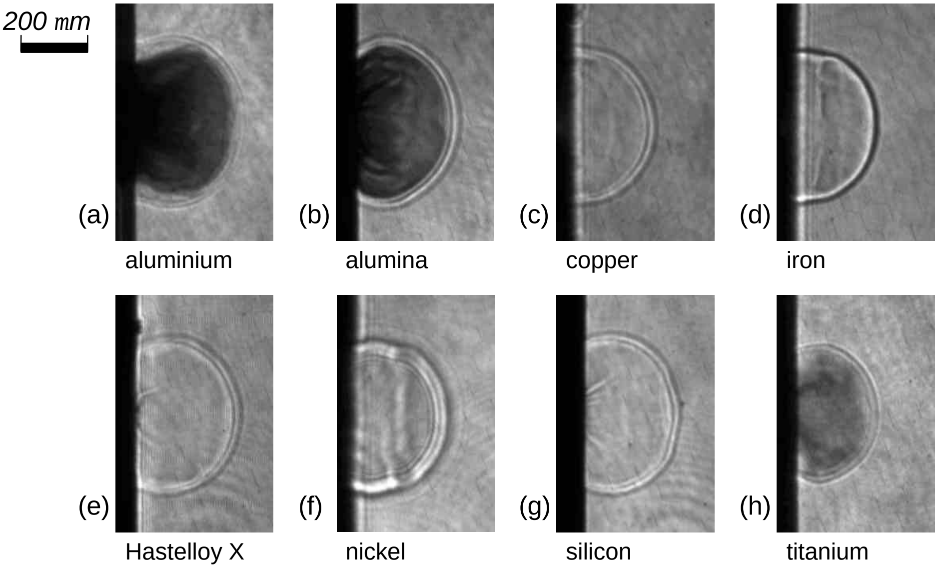

Figure 5.5: *Shadowgraphic images of drilling different materials recorded with a probe laser wavelength of 308 nm, at 200 ns after the start of the drilling pulse. Images of the* 2^{nd} *pulse of a series of pulses with a pulse energy of 1 mJ, and a power density of 1.1 GW/cm*^{2} *are shown.*

rials, no absorption lines exist close to the laser lines, as is also confirmed from spectroscopic tables (Handbook of Chemistry and Physics). The transparency of the plume seems to depend mainly on the absorption lines of the target material.

Ionization of the plume

Ionization of the vapour can strongly influence the transparency of the plume, which is illustrated with figure 5.6 for aluminium and titanium. The plume and the shockwave expand faster at the higher power density of figure 5.6b and 5.6d than at the lower power density of figure 5.6a and 5.6c. The faster expansion is expected due to an increase of the material removal per pulse. It was mentioned before, that a strong absorption line of neutral aluminium atoms exists at the drilling laser wavelength. At a relatively low power density, absorption is clearly visible as shown in figure 5.6a. Absorption of the laser energy can result in ionization. Absorption lines of multiple ionized aluminium do not exist at the drilling laser wavelength. Consequently, the laser beam is not strongly absorbed. This situation seems to be present in figure 5.6b, where the region between the target and the shockwave is clear. This effect is not visible for titanium (figure

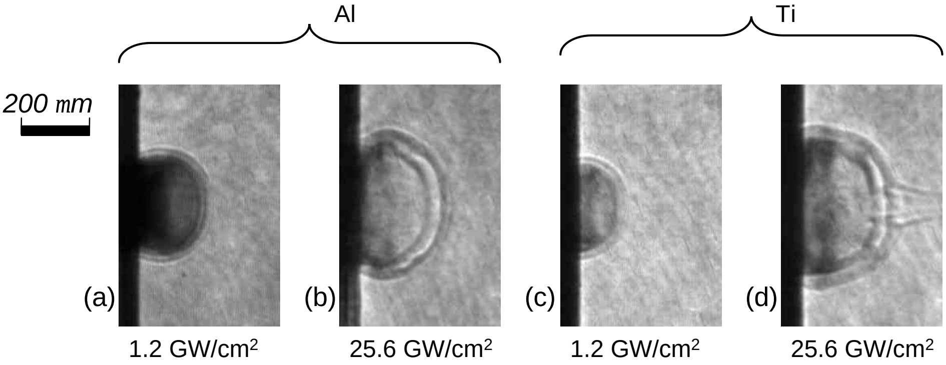

Figure 5.6: *Shadowgraphic images of drilling different materials, recorded with a probe laser wavelength of 308 nm, at 100 ns after the start of the drilling pulse are shown. The holes are drilled with different pulse energies. Images of the* 1^{st} *pulse of a series of pulses are shown.*

5.6c and 5.6d). It was mentioned before that an absorption line of singly ionized titanium exists at the drilling laser wavelength. The plumes as shown in figure 5.6c and 5.6d, seem to have a similar transparency for the low and high power density, which indicates that the absorption, of the drilling laser wavelength by the plume, does not change significantly. An interesting conclusion of this experiment is that with increasing power density, the attenuation of the plume can decrease, as is found here with aluminium.

Effect of the transparency of the plume

As discussed above, the plume that develops above the target, such a in figure 5.6, can influence the material removal rate, depending on whether the plume attenuates the laser beam at the drilling laser wavelength or not. The transparency of the plume depends on the processed material as was discussed in the previous section. Consequently, depending on the processed material, the removal rate may be strongly influenced. To illustrate the differences in material removal rate for some materials, the typical number of pulses required to drill through 125 μm foil are shown in table 5.2. At a power density of 1.1 GW/cm^2, the number of pulses necessary for drilling through iron and nickel is approximately twice the number of pulses for aluminium. In chapter 6, section 6.3.3 results of calculations with a 3-dimensional model will be given, which show that at relative low power densities the differences in removal rate are mainly caused by the thermophysical properties of the target material.

Table 5.2: *The number of pulses to drill through a 125 μm thick foil at different power densities.*

material	number of pulses at $I_{1/e^2} \approx 1.1$ GW/cm^2	number of pulses at $I_{1/e^2} \approx 18.7$ GW/cm^2
Al	12	2
Ni	22	14
Fe	28	
Cu	17	
Ti	17	

Experiments, performed at a high power density of 18.7 GW/cm^2 compared to a low power density of 1.1 GW/cm^2, show a much higher material removal for aluminium, but not for nickel (see also figure 4.8). An explanation may be that at higher power densities other than only thermal processes play an important role, which will be discussed here. The increased drilled depth per pulse for drilling aluminium at high power densities does not show saturation effects, which indicates that for drilling with long pulses the beam energy is not strongly attenuated by the plume, although the plume is not fully transparent as was seen in figure 5.5 and figure 5.6. Because of the restricted expansion, the vapour density in the hole is higher than outside the hole between the target and the shockwave. This may result in higher absorption of laser energy by the vapour, which subsequently causes a secondary drilling process, utilizing the energy absorbed by the plume (Abeln *et al.*, 1999; Treusch, 1985). The laser energy absorbed by the vapour inside the hole gives additional heating and expansion of the vapour, which will extend the drilling process by keeping the material longer in molten state, even after the laser pulse has ended. Furthermore, the extra heat input in the vapour increases the recoil pressure, which is the driving force for the ejection of molten material. These processes during drilling of aluminium are also expected to appear for titanium, but to a lesser extent because of the weaker absorption of the laser beam in the plume. It seems that a laser with a wavelength at or close to an absorption line of the drilled material improves the material removal process. Further study of these phenomena can be done by drilling with different wavelengths at the absorption lines of some metals (e.g. nickel, iron). However, this is beyond the scope of this thesis.

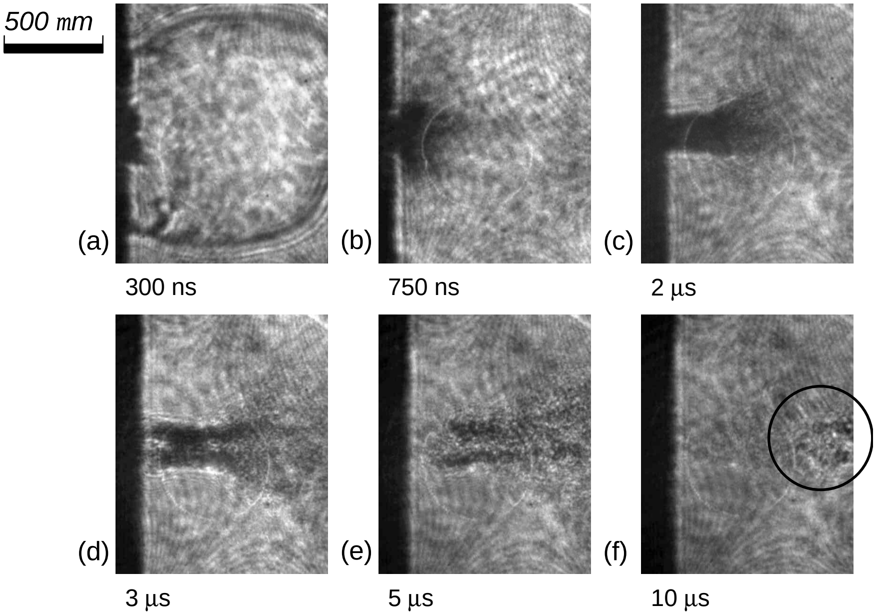

Figure 5.7: *Shadowgraphic images at different times after the start of the drilling pulse recorded with a probe laser wavelength of 532 nm. For drilling through the 500 μm thick aluminium foil, 8 pulses are needed. The images of the 6^{th} pulse with a power density of 29.0 GW/cm^2 are shown.*

5.2.3 Material removal development in time

Shadowgraphic images recorded after the pulse are shown in figure 5.7 at successive imaging times up to 10 μs after the start of the drilling pulse when drilling 500 μm thick aluminium foil at a power density of 29.0 GW/cm^2. Note that shadowgraphic images at successive times, for the same pulse number, have to be recorded during drilling of different holes. In figure 5.7a the shockwave is still in the field of view and a dark shadow of removed material starts to be visible. The images of figure 5.7 are recorded with a probe laser wavelength of 532 nm, at which aluminium vapour shows no significant absorption. In figure 5.5 was shown that the shockwave propagates closely in front of the target vapour for times up to 350 ns, from which is already known that the volume between target and shockwave in figure 5.7a is filled with vapour, although a shadow is not visible. What is seen, however, is a small dark region of material particles like vapour, clusters, and melt droplets. The density of this material is high enough to block the light from travelling through the plume. Figures 5.7b and 5.7c show the temporal development of material removal. In figures 5.7d and 5.7e it is seen that material is concentrated like a 'tube' around the hole centre.

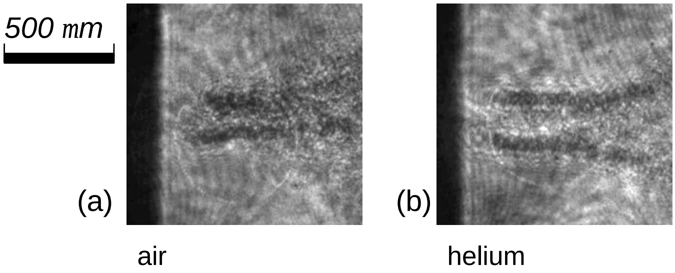

Figure 5.8: *Shadowgraphic images of a target which is placed in respectively air and helium. The image in air was shown before as figure 5.7e. Both images are recorded at 5 μs after the start of the drilling pulse with a probe laser wavelength of 532 nm. For drilling through the 500 μm thick aluminium foil, 8 pulses are needed. The images of the 4^{th} pulse with a power density of 34.9 GW/cm^2 are shown.*

This indicates melt ejection by the pressure build-up by vaporisation. In a simple model, as proposed by Von Allmen and Blatter (1995), this can be explained as caused by the expanding vapour, which exerts a pressure on to the melt. This pressure ejects the melt out of the hole with the walls as guidance. The ejection of material concentrated like a 'tube' like shown in figure 5.7e is even better visible when the target is placed in helium at atmospheric pressure (figure 5.8). This may be explained as follows. The inertial resistance of the environment to expansion is less with helium because of the lower mass of He with regard to N or O molecules. As a result, the ejection of the melt is more pronounced.

According to figures 5.7d and 5.7e material is leaving the hole long after the drilling pulse, at least up to times of 3 μs. The ejected material cloud shows clusters and droplets after a few μs. Figure 5.7f shows an encircled small ejected material cloud in the field of view up to 10 μs. The times at which a dark shadow of removed material is visible show that the main amount of the material is removed after the end of the 175 ns long drilling pulse.

The material removal development in time is compared for two power densities, 1.2 GW/cm^2 and 29.0 GW/cm^2. For both power densities a series of images is shown in figure 5.9. Comparison of figure 5.9e and 5.9a shows a stronger vaporisation resulting in a faster moving shockwave for the higher power density. In figure 5.9f and 5.9b, the dark region seems to be a combination of vapour, clusters formed by vapour condensation, and melt droplets. In figure 5.9c and 5.9d, droplets are becoming clearly visible. With the higher power, the ejected material cloud is denser as shown in figure 5.9g and 5.9h compared with 5.9c and 5.9d. Remarkable is the similar size of the ejected material cloud even al-

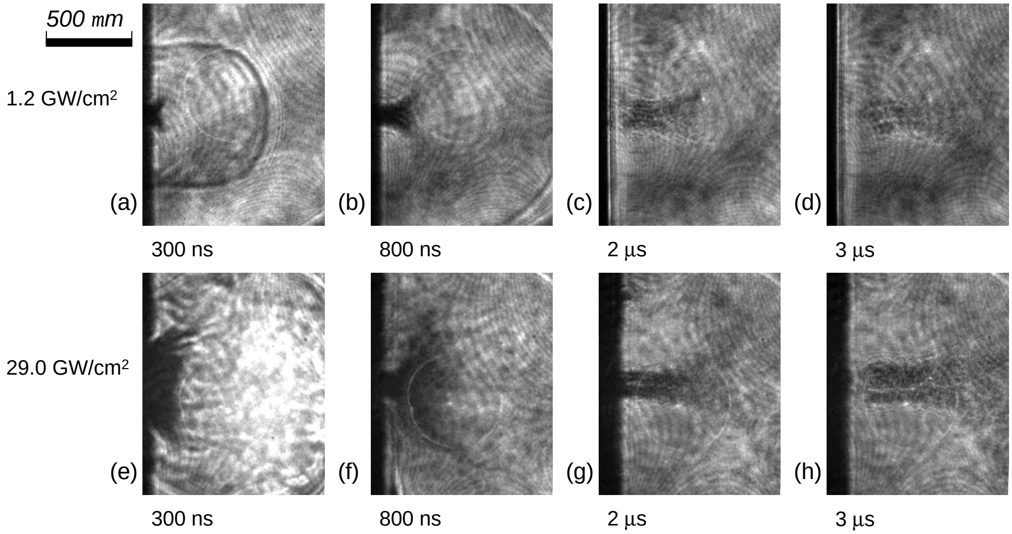

Figure 5.9: *Shadowgraphic images at different imaging delay times after the start of the drilling pulse recorded with a probe laser wavelength of 532 nm. Images are shown for two power densities for a drilling pulse starting at a similar depth. Images a to d, are recorded for 125 μm thick aluminium foil. The 7^{th} pulse is shown of 8 pulses which are needed for drilling through the foil. Images e to h, are recorded for 500 μm thick aluminium foil. The 2^{nd} pulse is shown of 8 pulses which are needed for drilling through the foil.*

though the power densities are largely different. This indicates that the velocity of the larger particles is similar in both cases. It seems that there is a maximum velocity that can be reached for the larger particles, independent of the power density. This maximum velocity was obtained to be about 300 m/s from the propagation of the front of the ejected material cloud as shown in figure 5.9b and 5.9c. A similar velocity is found from evaluating figures 5.9f and 5.9g. The time during which material is leaving the hole seems to be independent of the power density, similar as was found for the velocity. This is illustrated by comparing figure 5.9c with figure 5.9h, where, respectively, the material has ended leaving the hole after 2 μs for the power density of 1.2 GW/cm^2, and after 3 μs for the power density of 29.0 GW/cm^2. The long time during which material is leaving the hole compared with the pulse duration, indicates that the walls of the hole remain in molten state relatively long.

5.2.4 Material removal development at successive laser pulses

To study the material removal development during a series of pulses, images are recorded at a fixed imaging time at successive pulses for drilling a single

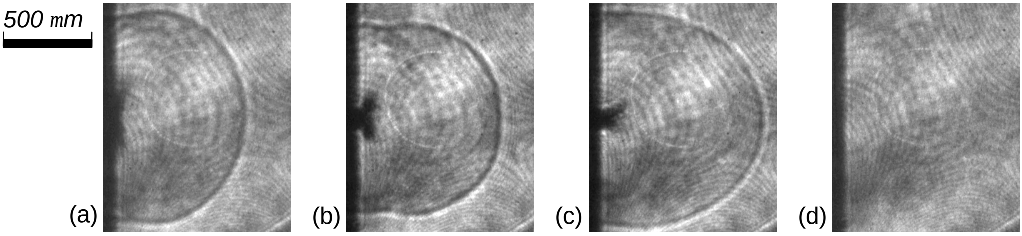

1st pulse 5th pulse 10th pulse 11th pulse

Figure 5.10: *Shadowgraphic images at successive drilling pulses with a probe laser wavelength of 532 nm. For drilling through the 125 μm thick aluminium foil, 10 pulses are needed. Images at 400 ns after the start of the drilling pulse are shown for a power density is 1.4 GW/cm^2. Note that the 11^{th} pulse is recorded after break-through.*

hole. Images of drilling 125 μm thick aluminium foil are shown in figure 5.10. Figure 5.10 shows, as an example, images of the 1^{st}, 5^{th}, 10^{th} and 11^{th} pulse. Figure 5.10a shows the material flow at the first of a series of drilling pulses, which irradiated the material at a flat surface. The vapour expanded for this first pulse mostly in radial direction, because at the first pulse the material flow is not influenced by a hole formed by previous pulses. The subsequent drilling pulses irradiate the target mainly at the bottom of an already formed hole, for example the fifth drilling pulse, which is shown in figure 5.10b. At first the material flows straight out of the hole, but shortly after leaving the hole the flow is bent sidewards. This effect is expected to be caused by rapid expansion of the material that leaves the hole. Figure 5.10c is recorded at the last drilling pulse before break-through and shows similar behaviour as figure 5.10b. Figure 5.10d shows the first pulse after drilling through the foil, hence no material removal is seen. A comparison of figure 5.10a, 5.10b and 5.10c shows that the sidewards bending of the flow occurs further away from the target when the hole is deeper. This shows that for increasing pulse numbers the removal of material is increasingly influenced by the walls of the hole formed during previous pulses. From this is expected that more energy is needed to eject the material from the deeper holes.

5.2.5 Material removal for different materials

In this section the results are described of studying the differences in material removal for materials with different properties. Because it is impractical to do experiments with all materials of interest, two materials with largely different properties were chosen for comparison, namely, aluminium and Hastelloy X (ap-

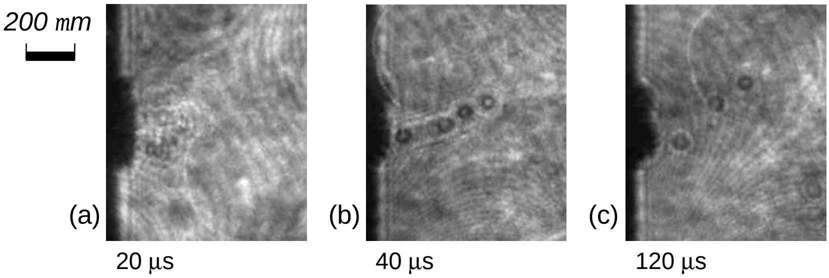

Figure 5.11: *Shadowgraphic images for drilling 650 μm thick Hastelloy X, recorded with a probe laser wavelength of 532 nm. For drilling through the foil, 80 pulses are needed. The power density is 34.9 GW/cm^2. Images are shown of pulses halfway the target at different times after the start of the drilling pulse.*

pendix B. Shadowgraphic images for Hastelloy X are shown in figure 5.11. In the first few microseconds after the drilling pulse, no ejected material is visible. Figure 5.11 shows that large particles are ejected at much later times between 10 and 100 μs after the drilling pulse. For aluminium, smaller particles are observed only within a few microseconds after the drilling pulse (figure 5.7). For Hastelloy X, particle velocities are obtained from the images to range from 5 to 20 m/s, which is 15 to 60 times slower than the velocity found for aluminium. Comparing the results of drilling, as shown in figures 5.7 and 5.11, the average drilled depth per pulse for aluminium is 8 times larger than for Hastelloy X at comparable pulse powers. The difference in the average drilled depth seems to be the result of the difference in the velocity of the material ejection. The larger velocity of the aluminium particles is expected to be caused by differences in thermophysical properties and also because differences in absorption of the laser beam by the vapour. As mentioned in section 5.2.2, it is expected for aluminium that a strong absorbing vapour inside the hole causes a secondary drilling process and an increase of the recoil pressure by utilizing the absorbed energy.

5.3 Summary and conclusions

In this chapter the results are described of studying the material removal during laser drilling and the optical transmission properties of the plume at the wavelength of the drilling laser. The results will be applied in the next chapter dealing with modelling of the drilling process.

For studying the material removal after the drilling pulse, holes are drilled with series of pulses in aluminium, and in Hastelloy X. The main amount of material removal in the experiments is seen at times relatively long after the end of the 175 ns long drilling pulse, e.g. for drilling 500 μm thick aluminium, the material removal ended after 3 μs. For drilling 650 μm thick Hastelloy X, the material removal ended after 100 μs. The drilled depth per pulse for aluminium is 8 times larger than for Hastelloy X at the same power density. The aluminium particle velocity is found to be at most 300 m/s, which is an order of magnitude higher than the Hastelloy X particle velocity of 5 to 20 m/s. A comparison of different materials showed that the drilling process has to be optimised for each material independently.

The optical transmission of the plume for the drilling laser wavelength is examined for aluminium, alumina, titanium, nickel, iron, silicon, copper and Hastelloy X. The shockwave propagates closely in front of the target vapour. Aluminium and titanium vapours are not fully transparent for the laser beam, which can be accounted for, by the existence of absorption lines of the processed material at the laser wavelength. The other examined target materials showed highly transparent vapour between the target and the shockwave. With the vapour being not fully transparent, aluminium drills for the given parameters the most efficient in comparison with the other studied materials. A possible explanation of this is that the vapour inside the hole supports the drilling process by additional heating, and by an increase of the recoil pressure, both, due to laser energy which is absorbed by the vapour. Furthermore, an interesting conclusion of this experiment is that with increasing power density, the attenuation of the plume can decrease.

Chapter 6

Modelling

In this chapter a theoretical, numerical model is described, which was developed to describe, quantify, and better understand the phenomena which have been experimentally observed in laser drilling of metals as described in the previous chapters. Existing sub-routines for modelling of keyhole development during laser welding (de Lange *et al*., 2003) are used to create the drilling model. The experimental observations described in the previous chapters led to a general idea of the laser drilling process and gave an impression of the various, involved physical phenomena. However, in experiments it is usually difficult to distinguish between the many processes that occur, even when a single experimental parameter is varied systematically. Modelling is an effective way to provide a better understanding of the influence of the different parameters on the process. Another issue is that, although experiments deliver a good insight into the overall process, experiments are sometimes difficult to perform or not possible for studying the dynamics on nanosecond timescales and micrometer spatial scales. This chapter will end with a comparison of the theoretical modelling with the experimental results.

Energy and mass balances were obtained to gain insight in the influence of the power, the pulse duration and the material properties on the drilling process. In figure 6.1 it is schematically shown for a typical situation how the energy of the laser beam is distributed in the hole drilling process. The energy in the laser beam, E_{laser}, is possibly attenuated by the plume, before it reaches the target surface. The amount of the energy not reaching the target, because of this attenuation, is called E_{att}. Part of the energy reaching the target is reflected and called E_{ref}. Material is removed by vaporization and as melt, for which respectively E_{vap} and E_{melt} are used. More energy is required for vaporization of a

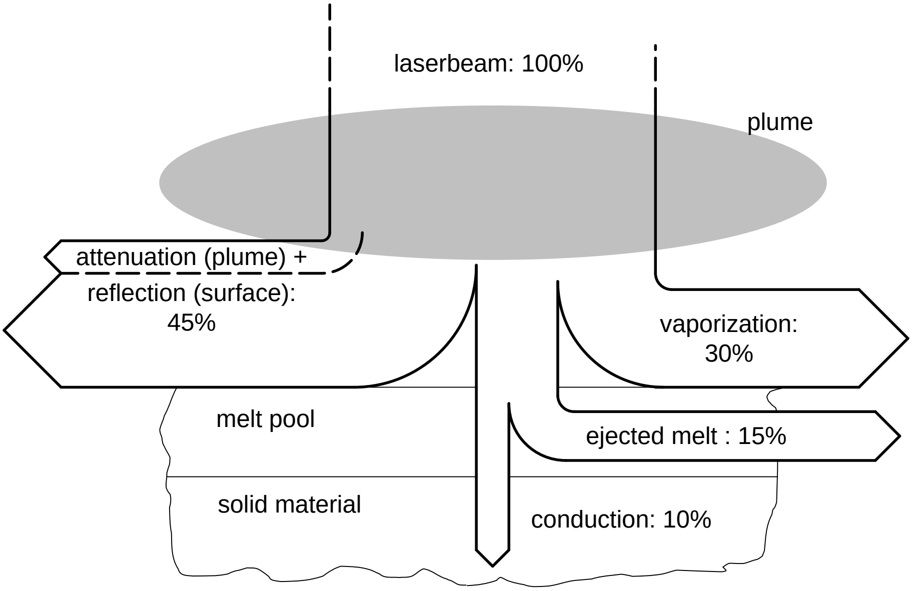

Figure 6.1: *Schematic view of the energy balance for a typical situation. This is the result for drilling of nickel with 150 ns pulse duration, 0.3 mJ laser pulse energy and a relative low power density of 0.25 GW/cm*^{2}. *The corresponding parameters and results can be found respectively in table 6.4 and figure 6.27.*

given volume of material than for melting and then ejecting the melt, because the specific enthalpy for melting is much lower than for vaporization. Although, more energy is used to remove material as vapour than as melt in the example of figure 6.1, the mass removed as melt is larger than the mass removed as vapour. The energy which heats the surrounding material by conduction is named E_{con}. The different fractions of the pulse energy are given in the energy balance of equation 6.1. However, the values for these fractions also strongly depend on the processing parameters, which will be discussed in further detail in this chapter.

$$E_{att} + E_{ref} + E_{con} + E_{melt} + E_{vap} = E_{laser}. \tag{6.1}$$

6.1 Modelling method

The model to be described here contains two major physical processes during laser drilling. These two are heat transfer and melt flow. Heat transfer by radiation, conduction and convection are considered. In figure 2.1 a schematic view of the laser drilling process was shown. The amount of the laser energy, absorbed by the target, heats the material and leads to melting and vaporization. The latter results in the build up of a recoil pressure, which ejects the melt like a piston, along the walls of the hole. For modelling of this complicated process the target material is divided in spatial domains that correspond to the 3 different phases of the material, i.e., the solid, liquid, and gaseous phase. These domains Ω are, called respectively, the solid, melt, and plume domain, indicated with Ω_s, Ω_m and Ω_p. In the solid domain, the main mechanism that needs to be taken into account is conduction. In the melt domain both heat transfer and melt flow need to be included. The plume domain consist of vapour, clusters formed by vapour condensation, and melt droplets (Yoo *et al.*, 2000; Schittenhelm *et al.*, 1996). In the model described in this chapter, the plume domain is not treated explicitly, although the relevance of the interaction between the plume and melt domain, will be discussed in section 6.3 where the results are presented. Furthermore, the boundary conditions for the melt domain are based on processes occurring at the melt-plume interface. On its turn the surrounding domain, e.g. air at atmospheric pressure, influences the expansion of the plume. The goal of modelling is to perform numerical calculations of the temporally dependent locations of the solid-liquid and liquid-vapour interface, as well as the velocity distribution in the melt, from which the shape of the drilled holes can be obtained.

6.1.1 Physical processes

Heat transfer

In general, heat can be transferred by three physical processes, which are transfer by radiation, conduction and convection. For the studied parameter range, it turns out, that heat transfer within the solid and melt are dominated by conduction and convection because of optical opacity of liquid and solid metal for the wavelength of the drilling-laser. Even at the liquid-vapour-interface conduction and convection are dominant. To verify this, the heat flow rate per surface unit and the energy of blackbody radiation, emitted from the liquid-vapour interface, during the drilling were estimated with the Stefan-Boltzmann law (Bejan, 1993). The radiated energy was found to be small, compared to the energy of the incoming laser pulse and can therefore be neglected. The remaining heat transfer processes of conduction and convection in the melt, can be described by the fundamental energy conservation law, which is derived and explained in more detail in appendix C. This equation is

$$c\,\rho\frac{\partial T}{\partial t} = \nabla \cdot k\nabla T - c\,\rho\,\vec{\mathbf{v}} \cdot \nabla T \tag{6.2}$$

where c is the specific heat, ρ is the density, T is the temperature, k is the thermal conductivity, t is the time and $\vec{\mathbf{v}}$ is the velocity of the melt. The left hand side of equation 6.2 represents the change of the accumulated heat in the material by a temperature rise. The first term on the right hand side represents conduction as caused by a temperature gradient. The second term on the right hand side represents convection of heat by material flowing with $\vec{\mathbf{v}}$. To be able to solve equation 6.2 for a laser beam irradiating the surface, it is necessary to apply proper boundary conditions and to calculate the velocity distribution $\vec{\mathbf{v}}$ of the melt.

Melt flow

To calculate the velocity distribution of the melt flow, both the momentum principle and the principle of mass conservation can be applied. The resulting momentum conservation equations, assuming a constant mass density ρ and a constant dynamic viscosity η can be described as

$$-\nabla p + \eta \nabla^2 \vec{\mathbf{v}} + \overrightarrow{\mathcal{F}_v} = \rho \left(\frac{\partial \vec{\mathbf{v}}}{\partial t} + (\vec{\mathbf{v}} \cdot \nabla)\, \vec{\mathbf{v}} \right) \tag{6.3}$$

which is derived and explained in more detail in appendix C. The left hand side of equation 6.3 represents the forces per unit volume working on the fluid, respectively through a pressure gradient ∇p, the viscous forces and external forces $\mathcal{F}_v$. In the cases studied in this thesis, an external force is gravity. However, the gravity turns out to be much weaker than the first two forces on the left hand side of equation 6.3 and is neglected in the model. The right hand side of equation 6.3 gives the change of momentum or in other words, the acceleration of the melt. Equation 6.3 is known as the Navier-Stokes equation for incompressible media (Bejan, 1993). Finally, the conservation of mass, assuming again a constant mass density ρ, is expressed as

$$\nabla \cdot \vec{\mathbf{v}} = 0. \tag{6.4}$$

6.1.2 Latent heat for melting

For a suitable model of hole drilling the phase transitions between the different states of the material have to be taken into account, which considerably modifies the heat transfer processes as described by equation 6.2. For the phase transition from the solid to the liquid state, as depicted in figure 2.1, a relatively large amount of heat is required per unit mass, which is called the latent heat for melting L_m. For pure materials this phase transition occurs at a rather sharply defined specific temperature T_m, which is called the melt temperature. For alloys, this phase transition occurs gradually over a finite temperature range. The modelling of a phase transition of pure material is relatively complicated with numerical methods, because of its discontinuous character. In the model the phase transition is taking place over a finite temperature range, which has been termed the ”continuous melt front model” as proposed by de Lange *et al.* (2003). In this approach the latent heat is described as a smoothly varying specific heat $c(T)$, versus temperature, which shows a peak of finite height and within a finite temperature interval $[T_m - \frac{1}{2}\Delta T, T_m + \frac{1}{2}\Delta T]$. Then, by reducing the size of the interval (while maintaining the area of $c(T)$) it is possible to gradually approach and approximate the melting also of pure materials. Within the melting temperature interval, the latent heat for melting is distributed with a smooth, continuous function, with a continuous derivative. A possible functional form for $c(T)$ is a cosine-shaped peak centred around T_m

$$c(T) = c + \frac{L_m}{\Delta T}\left(1 + \cos\left(\frac{2\pi}{\Delta T}(T - T_m)\right)\right). \tag{6.5}$$

Note that other functional forms may be selected, as long as the integral over $c(T)$ in the melt temperature interval is equal to the latent heat for melting L_m.

6.1.3 Solid-liquid interface

For describing the solid-liquid interface the transition from the non-moving solid material to a moving melt has to be defined. This can be depicted as a transition from an infinitely high viscosity in the solid domain to a finite value for the viscous flow of material in the melt domain. An indirect way to model this change from the melt domain to the solid domain is to assign to the material a viscosity with a smooth but rapid increase to infinity when the temperature is reduced to below the melt temperature. This method of modelling can be called indirect because the viscous force is actually proportional to the second derivatives of the velocity field, as is seen in equation 6.3, while there is no explicit temperature dependence of η in equation 6.3. However, setting the velocity to zero at high viscosity converges only slowly in the numerical solutions. A more direct approach is used, which yields the same physical effects and leads to a much faster numerical convergence. An artificial external force $\vec{\mathcal{F}}_\mathrm{v}$, sets the material velocity to zero below the melt temperature. This models the increase of viscosity to infinite below the melt temperature via the so-called ’stick-condition’, e.g. that the velocity of a liquid at an interface with a solid becomes equal to the velocity of the solid (in the case of a clamped target, as is used in the experiments, the velocity of the solid is zero). The temperature dependent external force function $\vec{\mathcal{F}}_{\mathrm{v}}(T)$ used for this method is

$$\vec{\mathcal{F}}_{\mathrm{v}}(T) = -f_f(T)\,\vec{\mathrm{v}} \tag{6.6}$$

where $f_f(T)$ attains high values below the melt temperature and becomes zero above the melt temperature. Again, this transition at the melt temperature is smoothed over a certain finite temperature range, as was described above for the specific heat. It was decided to do this with a smoothed Heaviside function. The advantage of this method is that the location of the solid-liquid interface does not have to be tracked, during the numerical solving of equations 6.2, 6.3 and 6.4. Instead, the solid-liquid interface is simply the isotherm surface that lies at the melt temperature, T_m, as shown in figure 6.2 as the dashed line.

6.1.4 Boundary conditions

Before numerically solving the equations 6.2, 6.3 and 6.4 for heat transfer and melt flow, all the initial values and the boundary conditions for all variable parameters need to be prescribed. These boundary conditions are chosen to match the time dependent physical conditions of the target. The equations are solved in cylindrical coordinates with axi-symmetry around the axis of the incoming laser beam. With this approach modelling is restricted to the description of drilling round holes with axi-symmetric vertically incident laser beams. Subsequently, the heat transfer and melt flow are assumed to be axi-symmetric and can be considered in a two-dimensional plane instead of a three-dimensional space such that the equations become numerically solvable in several days on a fast PC.

The labeling of the various domains and boundaries in the model are shown in figure 6.2 with r the radial coordinate and z the axial coordinate. The heat transfer is calculated in the melt domain Ω_m and the solid domain Ω_s with boundaries $\delta\Omega_1$, $\delta\Omega_2$, $\delta\Omega_3$, $\delta\Omega_4$, $\delta\Omega_5$, $\delta\Omega_6$ and $\delta\Omega_7$. Melt flow is only calculated in the melt domain Ω_m with boundaries $\delta\Omega_1$, $\delta\Omega_2$, $\delta\Omega_7$ and $\delta\Omega_8$. The solid-liquid interface will be located inside the melt domain Ω_m, and is indicated by the melt temperature T_m in figure 6.2. For solving the equations 6.2, 6.3 and 6.4, two different types of boundary conditions are used, the Dirichlet type, e.g., a specified pressure, and the Neumann type, e.g., a specified heat flow (Bejan, 1993).

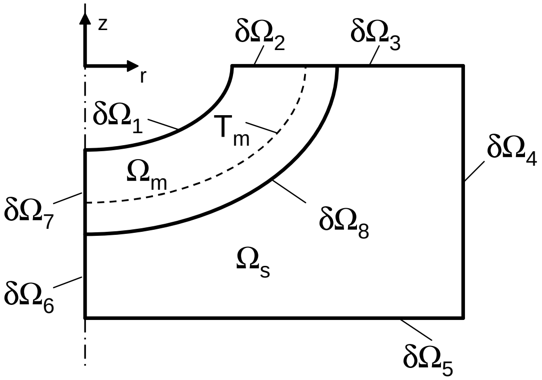

Figure 6.2: *The computational domain and the boundaries.*

6.1.4.1 Boundary conditions for heat transfer

For heat transfer the Neumann type of boundary conditions are described along the entire outside boundary, which can be written as

$$k\frac{\partial T}{\partial n} = q(s,t) \tag{6.7}$$

in this expression n is the coordinate in the direction normal to the surface. The coordinate s gives the position along the boundary and is defined perpendicular to the direction of n. $q(s,t)$ is a function which prescribes a heat flow rate per surface unit as function of s, and the time t. The boundary $\delta\Omega_6$ and $\delta\Omega_7$ form the symmetry axis. Therefore, the heat flow across this axis is zero which can be imposed by setting $q(s_{6,7},t) = 0$. At boundaries $\delta\Omega_4$ and $\delta\Omega_5$ is no laser irradiation and the dimensions of the domains are chosen in such a way, that heating by conduction is not significant during the time intervals in which calculations were performed. Therefore, $q(s_{4,5},t) = 0$ is prescribed at the boundaries $\delta\Omega_4$ and $\delta\Omega_5$. The heat flow rate per surface unit, $q(s_{1,2,3},t)$, on boundaries $\delta\Omega_1$, $\delta\Omega_2$ and $\delta\Omega_3$ is a result of the irradiation by the laser beam. Specifically, $q(s_{1,2,3},t)$ is the net absorbed heat flow rate per surface unit, which is the absorbed heat flow rate supplied by the laser beam, q_l, i.e. with attenuation and reflection taken into account, reduced by the heat flow rate required for vaporization, q_v. This is expressed in the following equation

$$q(s_{1,2,3},t) = q_l(s_{1,2,3},t) - q_v(s_{1,2,3},t). \tag{6.8}$$

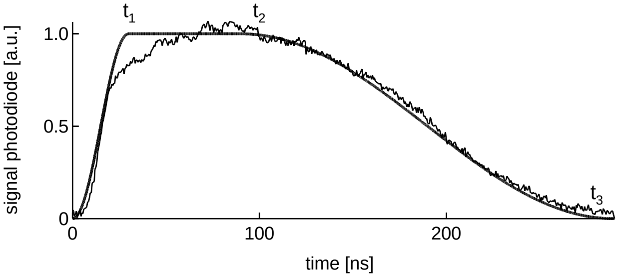

Figure 6.3: *Measured pulse and pulse used in modelling, both with 175 ns FWHM pulse duration.*

Laser beam

To obtain the absorbed heat flow rate supplied by the laser, first the power density distribution of the laser beam itself is discussed, which is modelled as a Gaussian distribution function

$$I(r,t) = f_p\,(t)\,I_0\,e^{-2\left(\frac{r}{w}\right)^2} \tag{6.9}$$

where I_0 is the maximum laser beam power density at the axis where $r = 0$, w is the radius of the Gaussian beam and $f_p(t)$ is a function which represents the temporal shape of the laser pulse. The function $f_p(t)$ is composed of three parts, respectively an increasing power density described by a cosine function from $t = 0$ to $t = t_1$, a steady power density from $t = t_1$ to $t = t_2$, and a decreasing power density described by a cosine function from $t = t_2$ to $t = t_3$. In figure 6.3 both the measured temporal pulse shape and the shape used in the model are shown. In figure 3.5 was already shown that the radial power density distribution is in good agreement with a Gaussian distribution function. The power density distribution in space and time is scaled with the pulse energy E_{laser} which was measured experimentally. The pulse energy in the model is calculated by integration of equation 6.9 which relates I_0 with the experimental pulse energy E_{laser} as

$$I_0 = \frac{4E_{laser}}{\pi w^2\,(t_2 + t_3 - t_1)}. \tag{6.10}$$

In section 2.1 was already discussed that many parameters influence the fraction of absorbed energy A. This can be expressed as $A(p_1, p_2, p_3, ...)$, where $p_1, p_2, p_3, ...$ are the parameters which A depends on. Using equation 6.9 and without multiple reflections, which is the case for shallow holes, this can be combined to

$$q_l = A(p_1, p_2, p_3, ...)\,n_z\,I_0\,e^{-2\left(\frac{r}{w}\right)^2} \tag{6.11}$$

where n_z is the component of the local outward normal vector of the boundary in the z-direction.

Vaporization

The vaporization at the surface leads to a heat flow rate leaving with the vapour. The theory behind it was already discussed in section 2.2.2 and is valid in the temperature range from the boiling temperature T_b almost up to the critical temperature T_c. The expression for the vaporized mass flow rate $\dot{m}_v$ was given in equation 2.13. Together with the vaporized mass flow rate a heat flow rate leaves the surface. This heat flow rate can be calculated with the enthalpy $H(T)$ to be

$$q_v = 0.82\, H(T)\, \dot{m}_v. \tag{6.12}$$

6.1.4.2 Boundary conditions for melt flow

For the melt flow, both Neumann and Dirichlet boundary conditions have been used. The melt flow is only calculated in the melt domain Ω_m, so, boundary conditions have to be prescribed on the boundaries $\delta\Omega_1$, $\delta\Omega_2$, $\delta\Omega_7$ and $\delta\Omega_8$. On the symmetry axis $\delta\Omega_7$ the symmetry boundary condition is applied, which implies that the normal velocity component (r-direction) and the tangential component (z-direction) of the viscous force are zero.

$$\vec{\mathbf{n}} \cdot \vec{\mathbf{v}} = 0 \tag{6.13}$$

$$\vec{\mathbf{t}} \cdot \vec{\mathbf{K}} = 0. \tag{6.14}$$

In these two boundary conditions, $\vec{\mathbf{n}}$ and $\vec{\mathbf{t}}$ are respectively the unit normal vector and the unit tangential vector. The viscous force per unit area $\vec{\mathbf{K}}$ is defined as

$$\vec{\mathbf{K}} = \vec{\mathbf{n}} \cdot \eta \nabla \vec{\mathbf{v}}. \tag{6.15}$$

For $\delta\Omega_8$ the velocity in all directions is zero, which is prescribed as

$$\vec{\mathbf{v}} = \vec{\mathbf{0}}. \tag{6.16}$$

At boundaries $\delta\Omega_1$ and $\delta\Omega_2$ the viscous forces are zero

$$\vec{\mathbf{K}} = \vec{\mathbf{0}}. \tag{6.17}$$

At boundaries $\delta\Omega_1$ and $\delta\Omega_2$ the vaporization leads to a pressure distribution which drives molten material out of the melt pool. For this pressure, the recoil pressure p_r as was given in equation 2.16 was used, resulting in the following boundary condition

$$p(T) = p_r. \tag{6.18}$$

6.2 Implementation

This section gives an overview about how the equations presented in section 6.1 are implemented in a software model. The practical implementation of the numerical method is based on the Finite Element approach for which the FemLab$^{\text{TM}}$ code was used (Comsol AB, 2001). FemLab$^{\text{TM}}$ is a general purpose FEM package which is based on MatLab$^{\text{TM}}$, a general engineering/mathematical software package. These combined packages provide a relatively open structure, with good options to implement other software codes, also codes written in other programming languages. For modelling the cylindrical coordinate system of figure 6.2 was used.

6.2.1 Moving boundary

Hole geometry

The liquid-vapour interface is tracked as a moving free surface, driven by the recoil pressure. The treatment of the moving boundary within a FEM code designed for fixed geometries, is done by converting the moving problem into a problem in a fixed geometry. For this, the differential equations 6.2 and 6.3, describing the problem in a fixed coordinate system are converted into equations that are valid for a deforming system. For this conversion, in principle, an arbitrary deformation velocity field can be chosen. In this model the deformation velocity was chosen to be equally to the material velocity.

For a deforming system, the ∇ operator is different from that for a fixed coordinate system, e.g., $\partial/\partial z$ changes because ∂z changes during each time interval of the calculation. Instead of taking this into account in the equations, the problem is solved for small subintervals of time, such that, within these, the deformations remain small. After each subinterval, the calculation is continued on a new mesh, in which the deformations have been taken into account. As with this method the movement of the material is followed, the free surface shape is automatically calculated, following the shape of the deforming boundary. As the deformation speed equals the material speed, there is no material transport across the boundary $\delta\Omega_1$. This implies that in the present model the vaporized mass is neglected. This approximation is justified, because the vaporized mass is small compared to the mass ejected as melt. As a further validation test for this assumption, the vaporized mass was calculated by integrating the vaporized mass flow rate $\dot{m}$, as given in equation 2.15, over the liquid-vapour interface. It showed indeed that even for the higher power densities, the vaporized mass remains below a level of about 10% of the ejected mass. It should be noted that, although the vaporized mass flow rate is neglected, the associated heat flow rate is large and is appropriately taken into account by the term q_v in equation 6.8.

Melt rim

Once the melt is pushed out above the original material surface at $z = 0$, it is decided to cut the melt domain off at this level, which gives the boundary $\delta\Omega_2$ a flat shape. The boundary conditions applied to this boundary are valid for an open, irradiated boundary. In reality, it is an internal boundary, which is covered by the ejected material. However, comparison with a model in which the ejected material was not cut off, showed that the solution is hardly influenced by the removal of the ejected material. This is because the power density in the region where the melt is ejected is relative low compared to the region of the melt pool itself, and therefore the results are hardly influenced by the laser irradiation on the edge of the hole.

6.2.2 Scaling

To obtain well scaled variables for numerically solving the equations for heat transfer and melt flow (6.2 and 6.3), the equations are made dimensionless by scaling (see table 6.1). The temperature T is scaled with the melt temperature T_m of the target material, the time t is scaled with a typical pulse duration t_p for the excimer laser used in the experiments. Similarly, the typical length scale L_0 was set to a value of the order of the focussed laser spot radius w_0. The typical velocity v_0 is then simply the ratio of the typical length and time scale. Scaling and rewriting of equation 6.2 gives

$$\frac{1}{Fo}\frac{\partial T}{\partial t} = \nabla \cdot k^* \nabla T - \frac{1}{Fo}\vec{\mathbf{v}} \cdot \nabla T \tag{6.19}$$

where T, t and v are now the scaled variables. The coefficient k^* is the thermal conductivity scaled with a typical value k_0, resulting in a function which is of

Table 6.1: *Scaling factors.*

scaling factor	order of magnitude	value
L_0	w_0	10 μm
t_0	t_p	200 ns
T_0	T_m	melt temperature
v_0	L_0/t_0	50 m/s

the order of unity, but taking possible temperature dependencies into account properly. Fo in equation 6.19 is the dimensionless Fourier function, which is a measure of the ratio between the conduction term and the time dependent term. This Fourier function is defined as

$$Fo = \frac{k_0\, t_0}{\rho\, c(T)\, L_0^2}. \tag{6.20}$$

As $c(T)$ is strongly temperature dependent, the resulting Fo function shows a strong change of its magnitude near T_m.

In a similar way the Navier-Stokes equations can be scaled to a dimensionless form

$$-\nabla p + \frac{1}{Re}\nabla^2\vec{\mathbf{v}} + \overrightarrow{\mathcal{F}_v} = \frac{\partial \vec{\mathbf{v}}}{\partial t} + (\vec{\mathbf{v}}\cdot\nabla)\,\vec{\mathbf{v}} \tag{6.21}$$

where p and $\overrightarrow{\mathcal{F}_v}$ are scaled with $1/(\rho\, v_0^2)$ and $L_0/(\rho\, v_0^2)$, respectively. Re is the dimensionless Reynolds number which is obtained with the scaling factors used as characteristic values (Bejan, 1993) and is

$$Re = \frac{\rho L_0 v_0}{\eta} = 10^3 \tag{6.22}$$

which is a measure for the ratio of the convective term in comparison with the viscous (frictional) term. The Reynolds number is lower than the critical value of $Re = 5\cdot 10^5$ for the transition from laminar to turbulent flow on a flat plate. Therefore, on the assumption of the flat plate flow a laminar flow can be expected in the studied parameter range, such that convection dominates well over friction (Bejan, 1993). The scaled expression for the conservation of mass, equation 6.4 is

$$\nabla\cdot\vec{\mathbf{v}} = 0. \tag{6.23}$$

6.2.3 Settings

Mesh and time intervals

The mesh is (re)generated in each time subinterval in the calculation, by making the local element size a function of the local temperature, found from the previous step. The mesh generation function has a minimum at the melt temperature, to obtain a refined mesh near the melt isotherm, where the non-linearity's of the coefficients and velocity gradients are strong. The strong non-linearity's are a result of taking into account the latent heat within the specific heat (equation 6.5) and the definition of an artificial external force $\vec{\mathcal{F}}_{\mathbf{v}}$ for setting the material velocity to zero below the melt temperature (equation 6.6). The correct choice of the numerical value of ΔT and the force coefficient function $f_f(T)$ respectively for equation 6.5 and 6.6 depends on the local temperature gradient and the mesh size near the T_m isotherm. These are chosen such that the change of the coefficients can be represented accurately enough in the numerical solving process.

To obtain an accurate calculation of the moving boundary (section 6.2.1), the length of the time subintervals is based on a mesh displacement criterion. This criterion is determined such that the mesh displacement during the time subinterval stays below a certain user defined value, which is a fraction of the minimum element size (typically between 0.1 and 0.25). This implies that calculations, in which larger material velocities are developed, will be solved with a larger number of time subintervals.

Numerical stability of the calculations

For higher power densities an increasing tendency for the formation of oscillations of the free surface was found. For modelling in the studied parameter range, it is necessary to take care of the numerical stability (Ruf *et al.*, 2003). These instabilities can be explained considering the free surface as an ordinary mass-spring system, with a negative damping which is caused by the time delay necessary for building up of the pressure. It is expected that this instability will be reduced if the plume domain and the resulting pressure field is taken into account. In order to suppress this oscillatory instability, some temperature dependent artificial damping was applied in the region of the free surface. Comparision of calculations with different damping values shows no large influence on the characteristic quantities of the ejection process, such as the drilled depth and the typical velocities.

Parameters

An overview of the parameters used for the calculations is given in appendix B. The material parameters are more or less dependent on the physical material conditions, especially on the temperature. This is relatively easy to include, e.g., the temperature dependency in the calculations. But, temperature dependent material data in a large temperature range, from room temperature up to the critical temperature, is scarcely available. For the materials of interest for modelling, a good overview of thermophysical properties up to temperatures slightly above the melting temperature is given by Mills (2002). For the calculations as presented in this thesis, constant material parameters are used.

6.2.4 Post processing

A typical result of a calculation during the laser pulse irradiation is shown in figure 6.4 for a better understanding of the following sections about the results of the calculations (parameters indicated as B22 in table 6.3). Figure 6.4a shows the calculated temperature and velocity field in the material at 10 ns after the start of the laser pulse. The temperature is represented by isotherms and the velocity field is represented by arrows. The room temperature $T(t=0)$, of 293 K, was taken as initial temperature in the calculations. The laser irradiates the moving boundary $\delta\Omega_1$. The solid and melt domain, respectively Ω_s and Ω_m are shown in the figure. Soon after the laser pulse starts, a melt layer is formed, and the surface temperature increases above the normal boiling temperature. In figure 6.4a the isotherm at the melt temperature of 933 K is the middle of three lines, indicated with T_m. The two outside lines are the isotherms for a temperature of respectively 50 K lower and 50 K higher than the melt temperature. The region between the moving boundary $\delta\Omega_1$ and the melt isotherm, indicated with T_m, is the melt pool. In figure 6.4b the isotherm at the normal boiling temperature of 2730 K is indicated with T_b, and an isotherm at T = 5000 K is shown. The maximum temperature at the surface, T_s = 7300K, is found at r = 0. The high temperature at the surface results in strong vaporization and consequently a recoil pressure builds up. This causes the melt to accelerate outwards, to a velocity that increases up to a value which depends on the power and dimensions of the laser beam. The velocity field is calculated only in domain Ω_m and shown in figure 6.4 by means of arrows. The directions of the arrows represent the direction of the melt flow and the lengths of the arrows represent the absolute value of the velocity. After the laser pulse has ended, the driving pressure disappears within

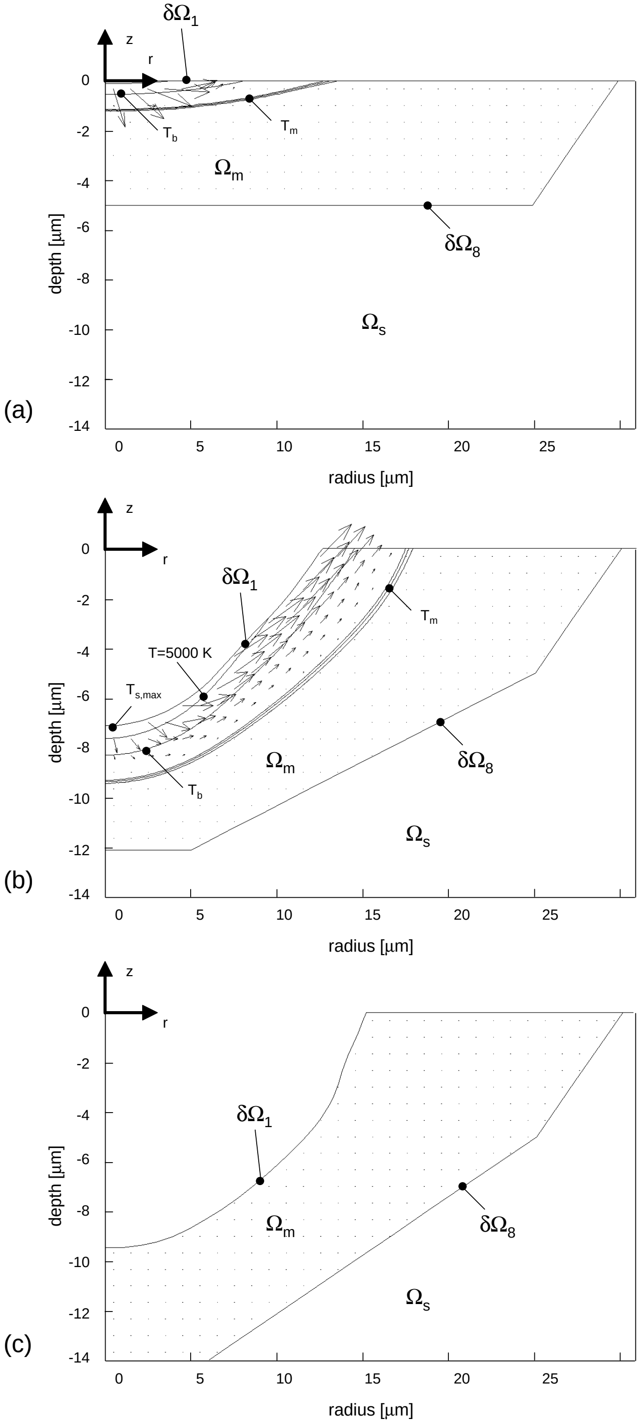

Figure 6.4: *Typical result of a simulation showing the shape, the temperature and the velocity field of an irradiated piece of aluminium at 10 and 100 ns after the start of the pulse (respectively figure a and b) and after resolidification and cooling down of the melt pool, figure c.*

a few nanoseconds. In contrast to this, the velocity of the melt ejection reduces more gradually, by the viscous effects, within a few hundreds of nanoseconds. The melt, which already gained velocity, keeps moving outwards after the end of the laser pulse until it cools down and solidifies. The final result is shown in figure 6.4c.

6.3 Results & Discussion

A series of calculations was performed to study the influence of some of the most important parameters involved in the hole drilling process. In this section an overview is given of the results of these calculations, which are compared with corresponding experiments. In a broad outline this section consists of three subsections. The first subsection deals with calculations for increasing power. The second subsection discusses the influence of the pulse duration and the third subsection is about processing different materials. The parameters that were used for the calculations are shown in a table at the start of each subsection. The material parameters are given in appendix B.

6.3.1 Calculations for increasing power

To study hole drilling with different powers, calculations were performed with the parameters as shown in table 6.2. The experimental setup for the corresponding experiments is described in section 3.1.2.

6.3.1.1 Heating, recoil pressure and melt flow

The laser irradiation heats the surface. The maximum temperatures are found at the symmetry axis, where the highest power density is found for a Gaussian distribution. The maximum temperature versus the power is shown in figure 6.5 and the maximum temperature versus the time is shown figure 6.6. Note that it is described in section 2.1 and shown in figure 6.1 that the available laser energy is attenuated by the plume and only a part of the energy passing through the plume is absorbed. Consequently, it was chosen to show in figure 6.5 to 6.17 the absorbed power and not the power in the laser beam. In figure 6.5 and figure 6.6 is shown that for an absorbed power of 57 W at the surface, a temperature is reached slightly above the boiling temperature, T_b, of 2730 K for aluminium. In the absorbed power range from 57 W to 143 W the heat flow rate leaving with

Table 6.2: *Parameters used for the calculations with increasing power, P. The calculations are done for aluminium, for which material parameters are given in appendix B. The focus diameter d_0 is 25 μm. The pulse duration (FWHM) is 175 ns and the pulse shape is described by t_1 = 30 ns, t_2 = 90 ns, and t_3 = 290 ns (figure 6.3). The separate calculations are numbered from A1 to A7.*

	P [W] (absorbed)	E_{puls} [μJ] (absorbed)	I [MW/cm^2] (absorbed)	depth [μm]
A1	29	5	6	0
A2	57	10	12	0.4
A3	143	25	29	6.3
A4	286	50	58	11.2
A5	571	100	116	17.7
A6	857	150	175	24.0
A7	1143	200	233	25.9

the vapour is still low. This results in a strong increase of the temperature with increasing absorbed power as is shown in figure 6.5. Above 143 W the heat flow rate leaving with the vapour increases strongly. As a result the temperature increases less steep with a further increasing absorbed power. Figure 6.6 shows that for higher absorbed powers, e.g. 286 W, a steady temperature is reached shortly after the start of the laser pulse. For low absorbed powers such a steady level is not reached during the pulse. At absorbed powers above 571 W, surface temperatures are reached above the critical temperature, T_c, of 8560 K for aluminium. This implies that, for modelling the laser drilling process at higher powers, the vaporization mechanism would have to include additional processes that occur above the critical temperature.

As soon as the temperature exceeds the boiling temperature, the vaporization rate is high enough to generate a recoil pressure, according to equation 6.18, which accelerates the melt into some transverse direction. In figure 6.7 the recoil pressure as function of time is shown for some of the absorbed powers which are shown in figure 6.6 and given in table 6.2. For an absorbed power of 29 W, the

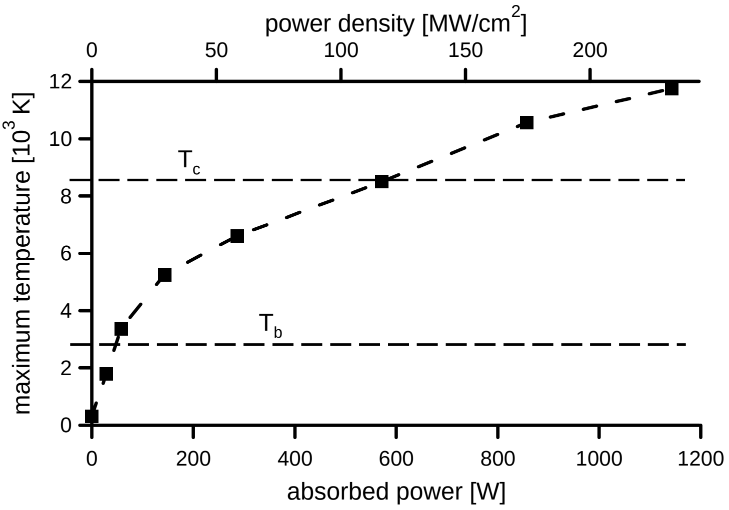

Figure 6.5: *The calculated maximum temperature versus the absorbed power (parameters of table 6.2). The line is constructed by interpolation between the calculated points, which are represented by the symbols.*

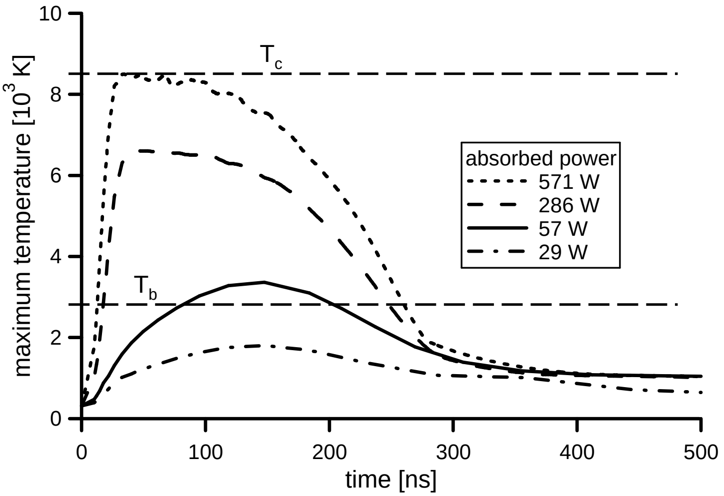

Figure 6.6: *The calculated maximum temperature versus the time for different absorbed powers (parameters of table 6.2, nr. A1, A2, A4 and A5).*

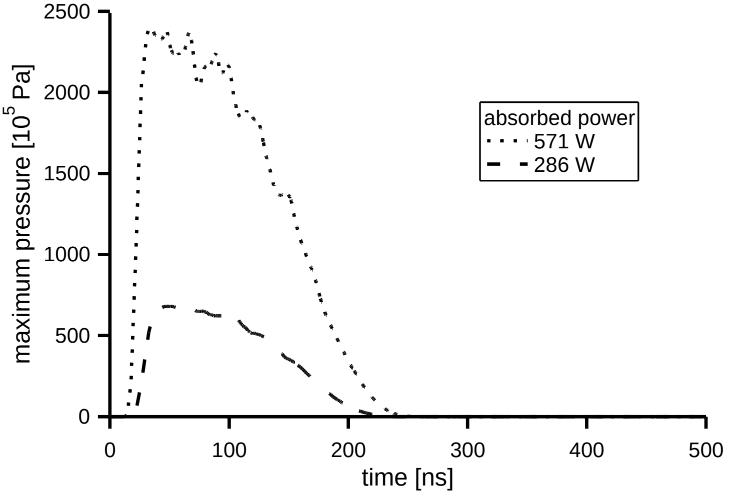

Figure 6.7: *The calculated recoil pressure versus the time for different absorbed powers (parameters of table 6.2, nr. A2, A4 and A5).*

boiling temperature is not reached and no recoil pressure is generated. For an absorbed power of 57 W, the boiling temperature is just exceeded and a very low recoil pressure of 10^5 Pa is generated, too low to be visible in figure 6.7.

After the end of the laser pulse, the recoil pressure almost immediately disappears. The velocity decreases more gradually because of inertial effects (i.e. the momentum of the moving melt maintains the velocity of the melt). However, friction leads to a gradual decrease, until the melt cools down and resolidifies. The maximum velocities are found in the region where the melt leaves the hole, as shown in figure 6.4. In figure 6.8 the maximum velocity of the ejected melt versus the time is plotted. The maximum velocity of the ejected melt versus the power is shown in figure 6.9. In figure 6.9 it can be seen that for increasing absorbed powers, the calculated velocities increase linearly. In contrast to this, in the experiments as described in section 5.2.3 the velocity of the melt was found to become independent of the laser power when the power density increased beyond some GW/cm^2. At the power densities around 1 GW/cm^2 at which experimental data of the melt velocity is available a comparison with the calculations can be made. The experiments show a maximum velocity of 300 m/s. The velocity of the melt in the model is found to be around 300 m/s for an absorbed power at which the surface reaches the critical temperature. Thus, it seems that the velocity of the melt reaches a maximum when the critical temperature is reached. A possible explanation is that above the critical temperature it is not possible to

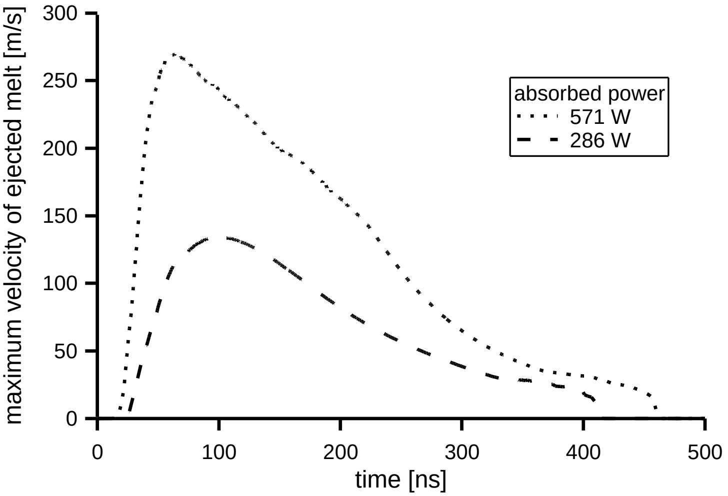

Figure 6.8: *The calculated maximum velocity versus the time for different absorbed powers (parameters of table 6.2, nr. A4 and A5).*

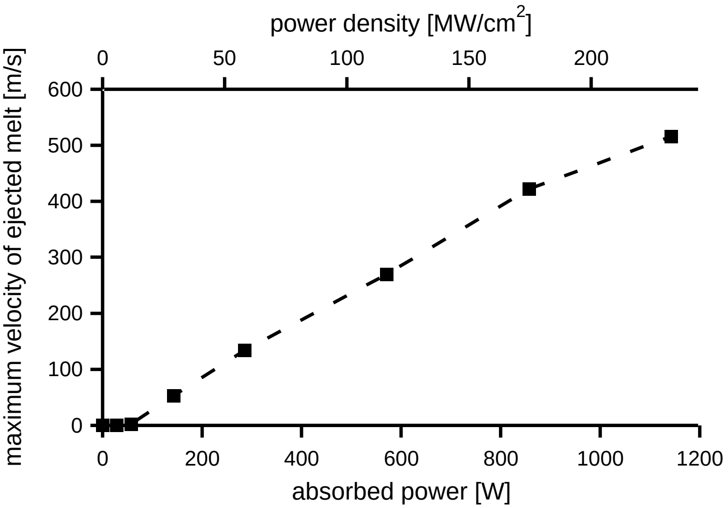

Figure 6.9: *The calculated maximum velocity versus the absorbed power (parameters of table 6.2). The dashed line is constructed by interpolation between the calculated points, which are represented by the symbols.*

distinguish between melt and vapour. The theory used for the modelling is based on a phase-equilibrium at the liquid-vapour interface (section 2.2.2). It seems that this assumption is no longer valid when the surface temperature is close to or above the critical temperature. Although the vapour pressure can still be high at these temperatures, the pressure gradients do not seem to increase, such that also the driving force for the melt flow does not increase further. Without an increase of the driving forces, consequently, there is no further acceleration of the melt.

6.3.1.2 Drilled depth versus power

The goal of the calculations is to understand the experimentally found correlation between the process parameters and the removal of material. This correlation will be explained with the help of figure 6.10 in which the drilled depth per pulse is shown, which is calculated as a function of the absorbed power. Plotting the drilled depth and the maximum temperature at the surface in one figure (figure 6.11) suggests a linear correlation between these two. The drilled depth per pulse is roughly proportional to the maximum temperature found at the surface of the melt pool in the centre of the laser beam. This proportionality is found, as soon as the temperature at the surface exceeds the boiling temperature, T_b, and the melt ejection mechanism has fully developed. An explanation, based on the model, is given in the remainder of this section.

In the calculations, the temperature gradient over the melt layer with thickness h is proportional to the velocity v_{sl} by which the solid-liquid interface moves into the material

$$v_{sl} \sim \frac{T_s - T_m}{h} \tag{6.24}$$

where T_s is the temperature at the surface and T_m is the temperature of the solid-liquid interface, which is the melt temperature. In other words, the temperature gradient determines how quick the heat, which is necessary for melting the material at the solid-liquid interface (the latent heat), can be transported through the melt layer and consequently how fast the interface propagates into the material.

Besides the velocity by which the solid-liquid interface moves into the material, the surface temperature strongly influences the vaporization rate and by that the recoil pressure, which drives the melt out of the hole, i.e., an increasing power leads to an increasing recoil pressure and an increasing

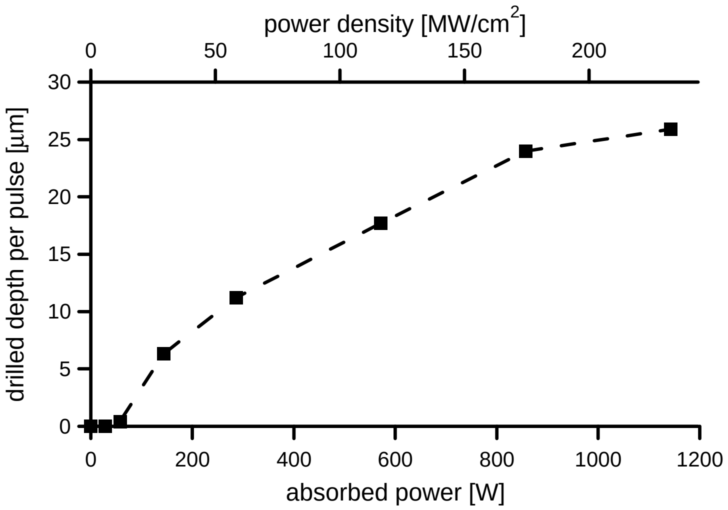

Figure 6.10: *The calculated drilled depth versus the absorbed power (parameters of table 6.2). The dashed line is constructed by interpolation between the calculated points, which are represented by the symbols.*

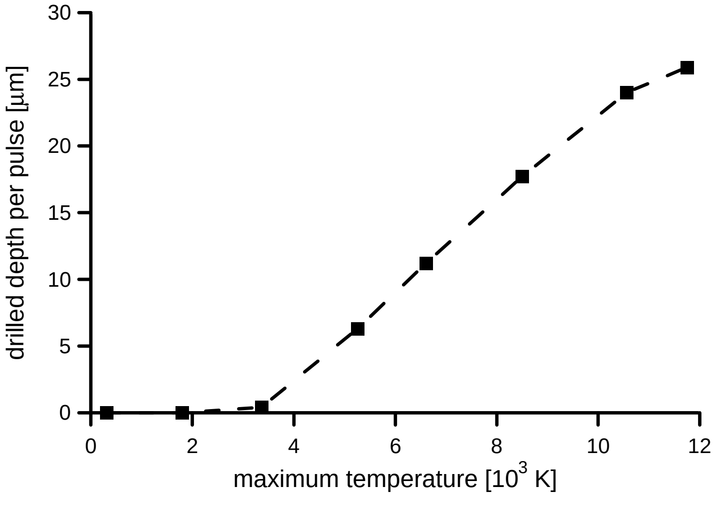

Figure 6.11: *The calculated drilled depth per pulse versus the maximum temperature at the surface (parameters of table 6.2). The dashed line is constructed by interpolation between the calculated points, which are represented by the symbols.*

velocity of the melt flow. The velocity of the solid-liquid interface and the velocity of the melt flow determine together the thickness of the melt layer at the bottom of the hole. The calculations show that the melt layer thickness increases at the start of the laser pulse up to a rather stable thickness of about 2 μm during the pulse, in the range from 30 to 175 ns, as is shown in figure 6.12. After the pulse has ended, the overheated melt provides the latent heat for further melting which increase the melt layer thickness. In the previous section it is already mentioned that the recoil pressure almost immediately disappears after the end of the laser pulse. For the absorbed power range in the calculations not all the material molten after the end of the laser pulse is sufficiently accelerated to leave the hole before the melt resolidifies.

Comparing calculations with different powers shows that the melt layer thickness remains of the same order of magnitude, during the pulse. This is illustrated in figure 6.12 for laser drilling with three powers. At a relatively low power of 286 W the melt layer thickness is 2.5 μm. With increasing power the melt layer thickness does not change significantly in the range from 30 to 175 ns. This leads to the following line of thoughts. The increase of the melt ejection velocity is such that, although the velocity of the solid-liquid interface increases, the melt layer thickness is only weakly influenced by the power. This indicates, according to equation 6.24, that the velocity of the solid-liquid interface depends mainly on the surface temperature. Consequently, the velocity of the solid-liquid interface determines the drilled depth. This line of thoughts may be the explanation for the proportionality between the surface temperature and the drilled depth in the calculations as depicted in figure 6.11. Note, however, that this proportionality and explanation are only found in the power regime with fully developed melt ejection.

6.3.1.3 Energy balance and mass balance

In this section the energy balance for the calculations with the parameters of table 6.2 is discussed, to gain a better insight into the relative importance of the different material removal processes for hole drilling. The absorbed energy from the laser beam is used to heat the solid, to melt material and to vaporize material. Part of the melt is ejected and part of it resolidifies after the laser pulse has ended. The different fractions of the pulse energy versus the absorbed power are shown in the energy balance of figure 6.13. For a clearer description of the energy balance, the relative fractions of the pulse energy are shown in figure

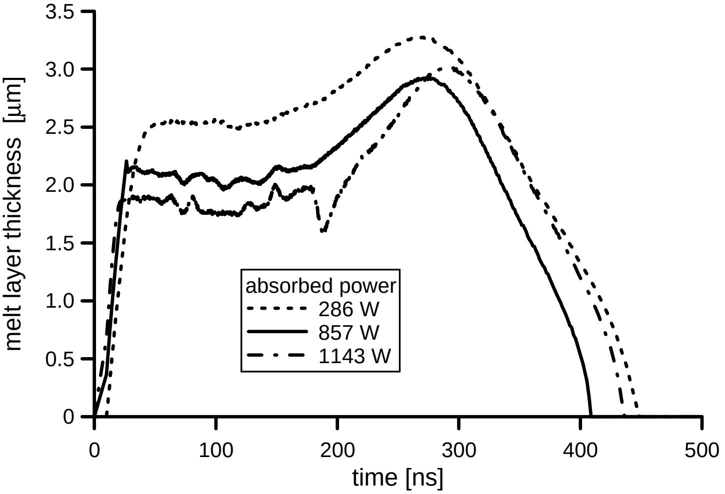

Figure 6.12: *The melt layer thickness at $r = 0$ versus the time (parameters of table 6.2, nr. A4, A5 and A7).*

6.14. This figure shows for powers up to 57 W no material removal and that all of the absorbed laser energy is used to heat the solid. The relative fraction of the pulse energy in the ejected melt, increases to 40% for powers between 57 W and 286 W, while the relative fraction of the pulse energy for vaporization increases to 10%. For further increasing powers, the relative fraction of the energy for both, the ejected melt and the vapour increases to respectively 50% and 25% at a power of 857 W. This results in a decrease of the relative fraction of the energy in the solid to 25%. Beyond the power of 857 W the relative fraction of the energy in the ejected melt reduces slightly from 50% to 45% by the increase of the relative fraction of the energy used for vaporization. Figure 6.14 shows that the maximum calculated relative fraction of the energy leaving with the melt is 50%.

The ratio between the removed mass as melt and as vapour is completely different from the ratio between the fraction of the pulse energy leaving with the melt and leaving with the vapour. To illustrate this, the energy balance is considered together with the mass balance. The absolute and relative mass balance are respectively shown in figure 6.15 and 6.16. In figure 6.14 is shown that at the power of 857 W, 50% of the absorbed energy is found in the ejected melt and 25% is found in the vapour. In figure 6.16 this corresponds with 90% of the material removed by melt ejection and 10% removed as vapour. This shows that for material removal only a small vaporized mass is sufficient to eject a relative

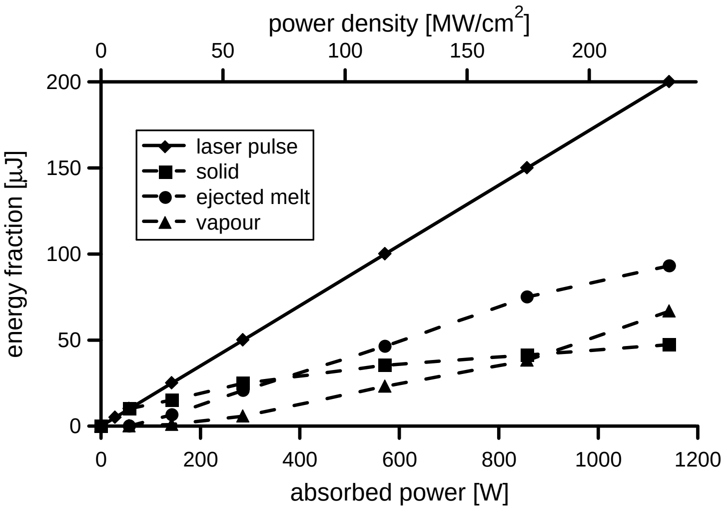

Figure 6.13: *The absorbed pulse energy and the fractions of the absorbed pulse energy used for respectively heating of the solid, ejection of the melt and vaporization versus the absorbed power (parameters of table 6.2). The lines are constructed by interpolation between the calculated points, which are represented by the symbols.*

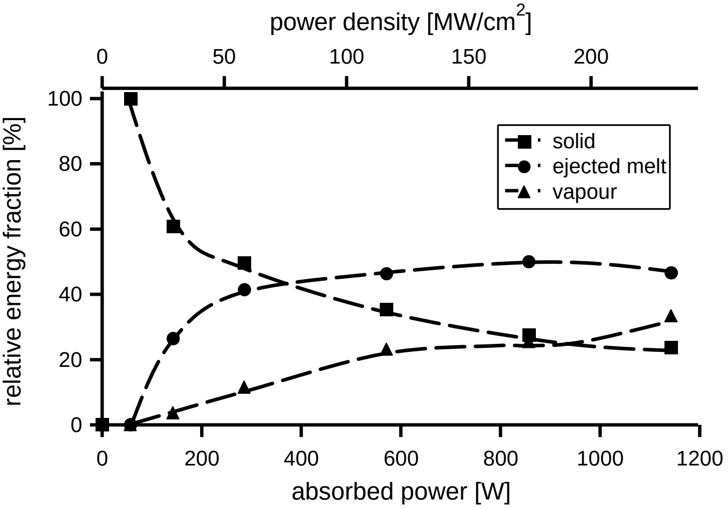

Figure 6.14: *The relative fractions of the absorbed pulse energy used for respectively heating of the solid, ejection of the melt and vaporization versus the absorbed power (parameters of table 6.2). The dashed lines are constructed by interpolation between the calculated points, which are represented by the symbols.*

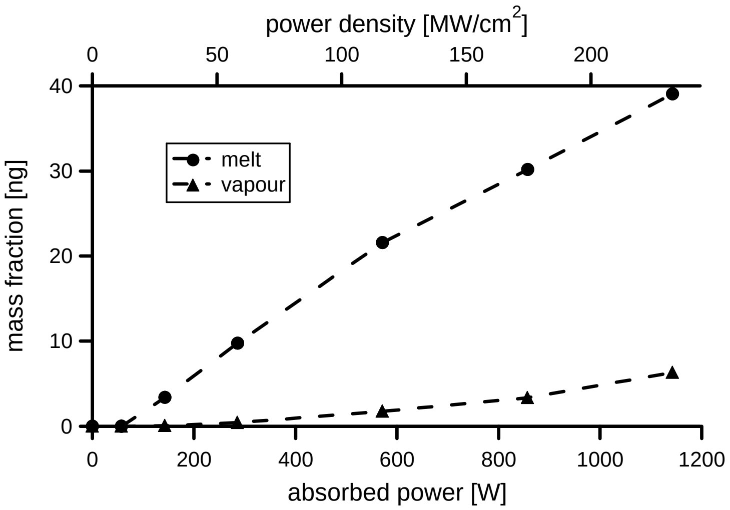

Figure 6.15: *The fractions of the mass removed by melt ejection and vaporization versus the absorbed power (parameters of table 6.2). The dashed lines are constructed by interpolation between the calculated points, which are represented by the symbols.*

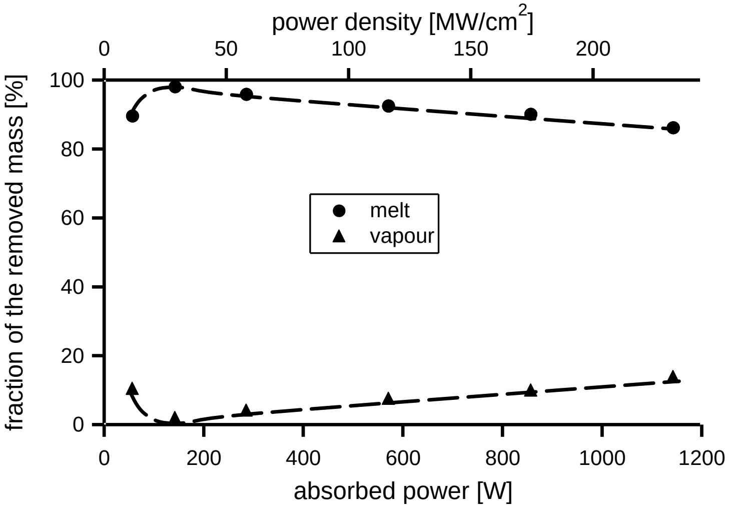

Figure 6.16: *The relative fractions of the mass removed by melt ejection and vaporization versus the absorbed power (parameters of table 6.2). The dashed lines are constructed by interpolation between the calculated points, which are represented by the symbols.*

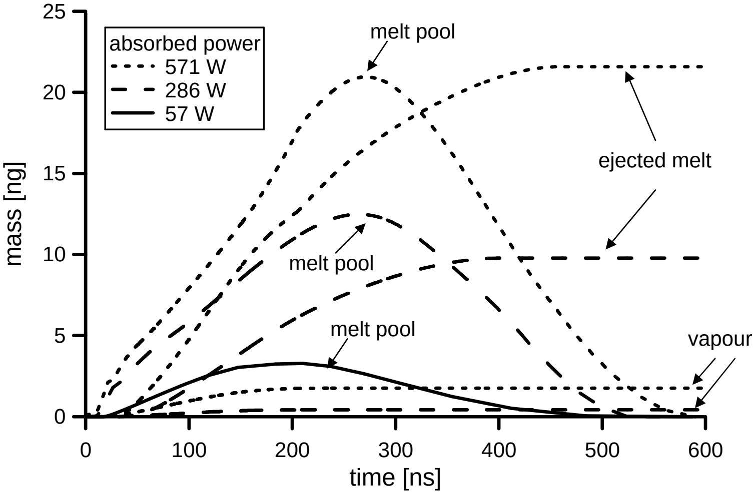

Figure 6.17: *The temporal development of the mass removed by vaporization and removed by melt ejection and the amount of molten material which resolidifies on the walls of the hole (parameters of table 6.2).*

large mass of melt. It also shows that a relative large fraction of the pulse energy is necessary for vaporization even when only a relative small mass is removed as vapour.

In figure 6.17 for some power densities the mass of the ejected melt, the mass of the vapour and the mass of the melt which is still in the hole are shown. It can be seen that a relative large amount of material is molten and resolidifies in the hole, because, after the laser pulse has ended, the recoil pressure almost immediately disappears as was shown in figure 6.7.

6.3.1.4 Comparison with experimental results

In this section, the calculations are compared with experiments. The available laser energy is attenuated by the plume and only a part of the energy passing through the plume is absorbed. This has to be taken into account in comparing the model results with the experimental results. In figure 6.5 to 6.17 the absorbed power was shown and not the power in the laser beam. In the experiments the beam energy was measured and the corresponding power in the laser beam was obtained with the pulse duration. To facilitate the comparison, the difference between the absorbed energy and the energy in the laser beam, which represents attenuation by the plume and reflection at the surface, is estimated.

For this estimation, a model is developed which describes the attenuation of the laser beam by the plume. The absorptivity (section 2.1) is taken as a constant, and only depends on material and wavelength. The used absorptivity for aluminium, A_0= 0.14, can be found in appendix B. The simplification of taking a constant value for A_0 is justified because the calculations are performed for the first pulse on a flat surface, such that effects of multiple reflections and large incident angles can be safely neglected (section 2.1). A simplified model of the attenuation by the plume is based on the Lambert-Beer's exponential law with an attenuation coefficient, based on the amount of particles in the plume characterized by the average vaporized mass flow rate $\dot{m}_{av}$. The attenuation of the plume for a large vapour flow is expected to be maximized at a certain level, because a vapour flow remains necessary to maintain the plume.

All this together is expressed in an overall absorptivity at the surface, $A(\dot{m}_{av})$, as function of the average vaporized mass flow rate

$$A(\dot{m}_{av}) = A_0 \left(c_1 + (1 - c_1) e^{-c_2 \dot{m}_{av}} \right) \tag{6.25}$$

where c_1 and c_2 are coefficients and $\dot{m}_{av}$ is the net vaporized mass flow rate, $\dot{m}$, averaged over the pulse duration. The coefficient c_1 maximizes the plume attenuation. In equation 6.25 the attenuation is zero when the vaporized mass flow rate is zero. The exponential term describes the attenuation of the laser beam passing through the vapour. The attenuation coefficient ($c_2 \dot{m}_{av}$) is assumed to increase linearly with the average vaporized mass flow rate $\dot{m}_{av}$ by multiplying this with a factor c_2.

In figure 6.18, the calculated drilled depth versus the absorbed power is shown once again. The overall absorptivity is calculated from equation 6.25, based on this case with $A_0 = 0.14$, $c_1 = 0.4$ and $c_2 = 5 \cdot 10^5 (m^2 s)/kg$. The coefficients, c_1 and c_2 are chosen such, that the calculations fit with the experimental results as shown in table 6.2. In figure 6.19 the calculated drilled depth is shown while taking into account the overall absorptivity from equation 6.25. Only three experimental points are shown, which is enough to explain the principle. In section 6.3.2 and section 6.3.3 of this thesis, comparison with more experimentally measured data is presented, which provides a further validation of the assumptions made in the model. As explained, equation 6.25 provides the

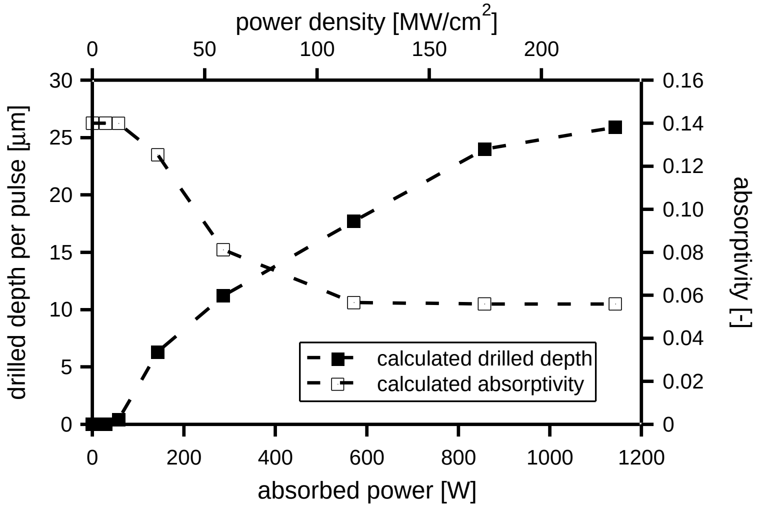

Figure 6.18: *The calculated drilled depth versus the absorbed power and the overall absorptivity (parameters of table 6.2). The dashed lines are constructed by interpolation between the calculated points, which are represented by the symbols.*

derived scaling, namely that now the x-axis of the figure shows the laser power instead of the absorbed power.

The estimation of the laser power enables to show the experimentally obtained drilled depth in the same figure as the calculated drilled depth as in figure 6.19. Comparing both drilled depths, shows good agreement between them. In section 6.3.2 and section 6.3.3 of this thesis, comparisons of the model results with more experimentally measured data is presented, also with good agreement. The explained inclusion of the overall absorptivity results in a realistic model that can be used to calculate the efficiency of the drilling process.

This efficiency is expressed as the specific energy necessary to remove material and is shown in figure 6.20. At a laser power of 1.1 kW the vaporization is large enough to generate a recoil pressure which results in fully developed melt ejection. At this power the vaporization is still low and consequently there is a minimal attenuation of the laser beam by the plume. For increasing powers, the attenuation of the laser beam by the plume results in an increase of the specific energy and therefore a lower efficiency. But, in the laser power range from 10 to 20 kW, the specific energy remains similar, which can be understood from figure 6.18 which shows that the attenuation by the plume does not increase anymore in the mentioned laser power range. For the case of figure 6.18, it is clear that

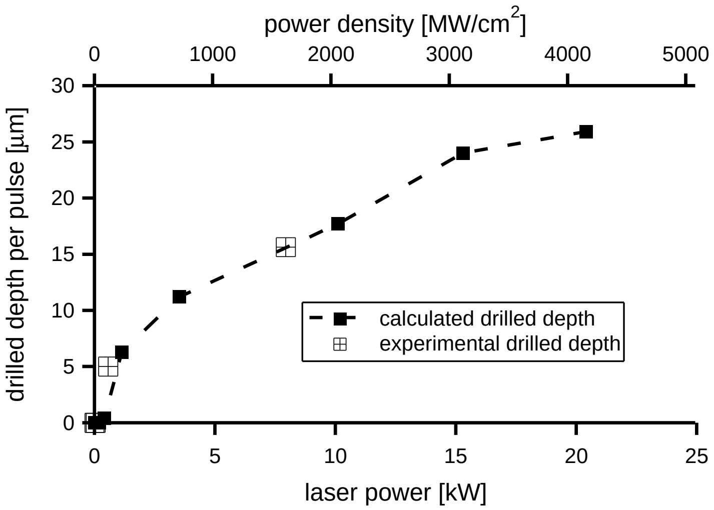

Figure 6.19: *The calculated drilled depth and the experimentally measured drilled depth per pulse versus the laser power (parameters of table 6.2). The dashed line is constructed by interpolation between the calculated points, which are represented by the symbols.*

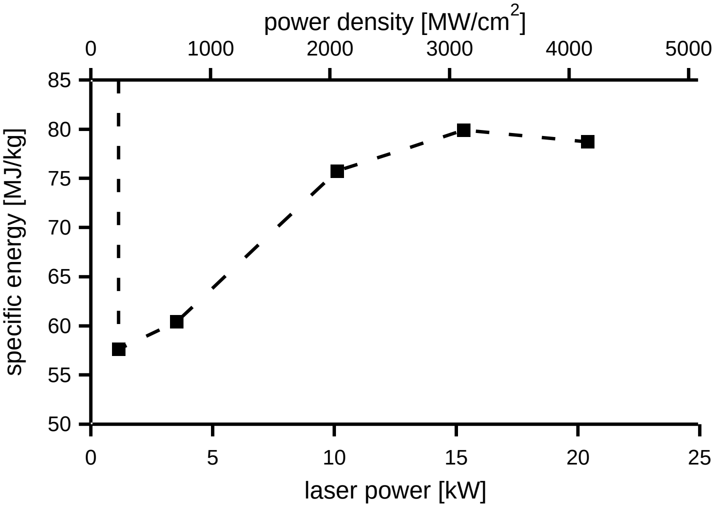

Figure 6.20: *The calculated specific energy versus the laser power (parameters of table 6.2). The dashed line is constructed by interpolation between the calculated points, which are represented by the symbols.*

the material removal process is the most efficient in terms of the necessary specific energy around a laser power of 1 kW. At this laser power the vaporized mass flow rate is still low, but the vaporization is large enough to eject the melt. The low vaporized mass flow rate results in low attenuation of the laser beam by the plume. A more general conclusion is that the process is the most efficient for the laser power at which melt ejection has just fully developed.

Summary

- The velocity of the melt reaches a maximum when the critical temperature is reached.
- The obtainable drilled depth depends strongly on the surface temperature of the target, which is directly related to the heat conductivity of the material. This implicates that the heat conduction determines the obtainable drilling velocity.
- The drilling process is the most efficient for the laser power at which melt ejection has just fully developed.
- For drilling of aluminium, a model for attenuation of the laser beam by the plume gives a good explanation for the experimentally measured drilled depth.

6.3.2 Influence of the pulse duration

To study the influence of the pulse duration on the hole drilling process, calculations were performed for drilling with different pulse durations. Calculations were performed with the parameters as shown in table 6.3. The experimental setup for the corresponding experiments was described in section 3.1.2. These calculations were done to compare the drilled depth calculated by the model with the experimental data of figure 4.6. In figure 6.21 the calculated drilled depth per pulse versus the power is shown for four different pulse durations between 9 and 104 ns.

To obtain a better understanding of the processes playing a role, the calculated relative fractions of the energy for the different processes are shown separately in figure 6.22 for a pulse duration of 9 and 104 ns. With the low powers, up to

Table 6.3: *Parameters used for the calculations with different pulse durations, t_p. The calculations are done for aluminium, for which material parameters are given in appendix B. The focus diameter d_0 is 25 μm. The pulse duration (FWHM) is described by t_1, t_2, and t_3 (figure 6.3). The separate calculations are numbered from B1 to B24.*

	t_p [ns]	t_1 [ns]	t_2 [ns]	t_3 [ns]	E_{puls} [μJ] (absorbed)	P [W] (absorbed)	I [MW/cm^2] (absorbed)	depth [μm]
B1	9	9	9	18	2.2	240	49	0
B2	”	”	”	”	4.3	481	98	0.9
B3	”	”	”	”	8.7	962	196	2.0
B4	”	”	”	”	17.3	1923	392	2.6
B5	”	”	”	”	26.0	2885	588	2.9
B6	21	10	21	31	2.0	96	20	0
B7	”	”	”	”	5.4	240	49	1.2
B8	”	”	”	”	10.1	481	98	2.4
B9	”	”	”	”	20.2	962	196	3.7
B10	”	”	”	”	40.4	1923	392	4.6
B11	”	”	”	”	60.6	2885	588	2.9
B12	48	10	48	58	2.3	48	10	0
B13	”	”	”	”	4.6	96	20	0.3
B14	”	”	”	”	11.5	240	49	3.1
B15	”	”	”	”	23.1	481	98	4.8
B16	”	”	”	”	46.1	962	196	7.0
B17	”	”	”	”	92.3	1923	392	8.9
B18	”	”	”	”	138.5	2885	588	10.0
B19	104	10	104	114	105	48	10	0
B20	”	”	”	”	10	96	20	2.7
B21	”	”	”	”	25	240	49	6.3
B22	”	”	”	”	50	481	98	9.5
B23	”	”	”	”	100	962	196	14.1
B24	”	”	”	”	200	1923	392	17.2

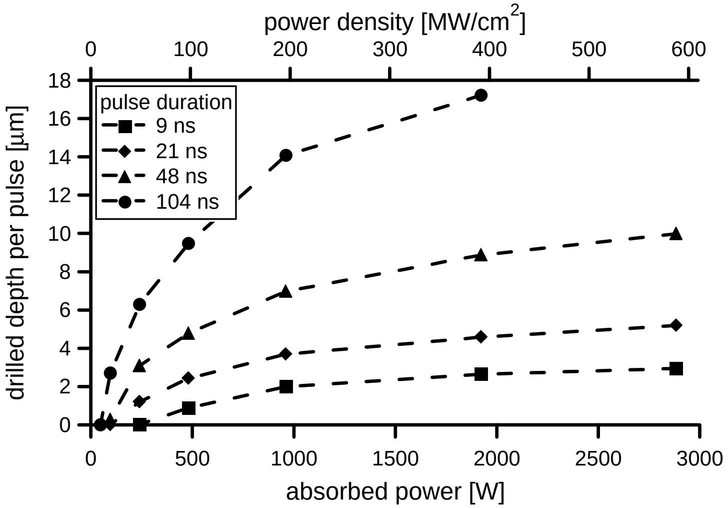

Figure 6.21: *The calculated drilled depth versus the absorbed power for a pulse duration of 9, 21, 48 and 104 ns (parameters of table 6.3). The dashed lines are constructed by interpolation between the calculated points, which are represented by the symbols.*

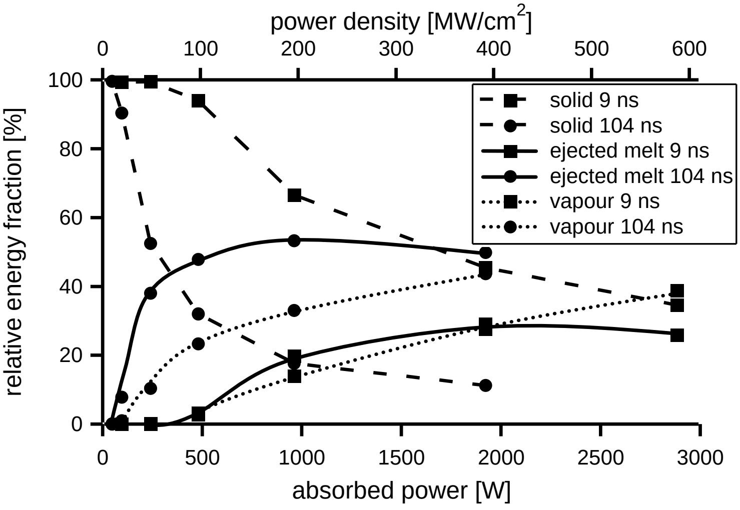

Figure 6.22: *The fractions of the absorbed pulse energy used for respectively heating of the solid, ejection of the melt and vaporization versus the absorbed power for a pulse duration of 9 and 104 ns (parameters of table 6.3, nr. B1-B5 and B19-B24). The lines are constructed by interpolation between the calculated points, which are represented by the symbols.*

48 W for the 104 ns pulse duration and up to 96 W for the 9 ns pulse duration, no material is removed and all the laser energy is used to heat the solid. Comparing the short pulse of 9 ns with the long pulse of 104 ns for the increasing powers, shows that with the short pulse a large fraction of the absorbed energy heats the solid material. This is expected for the 9 ns pulse because the time to ’prepare’ the material by heating it up to temperatures where the material starts to be removed by vaporization and melt ejection is relatively long compared to the pulse duration. This is shown in figure 6.23 in which the temperature decreases after the end of the pulse for the 9 and 21 ns pulse before a steady temperature is reached. In figure 6.24 is shown that the maximum velocity reached during the pulse, increases with the pulse duration. Besides the increase of the velocity, the material remains longer in a molten state, which gives the melt more time to leave the hole. For the long pulse of 104 ns is shown in figure 6.22 that the fraction of the energy used for melt ejection increases strongly, up to a value of 50% at an absorbed power of 1 kW. For even higher powers, the energy fraction in the ejected melt reduces somewhat by the rapid increase of the energy fraction used for vaporization. For the long pulse of 104 ns, the fraction of the energy used for vaporization is higher than for the short pulse of 9 ns. Since the mass flow rate associated with vaporization is much less than that for melt ejection, figure 6.22 suggest that long pulses will be more efficient for drilling than shorter pulses. This was already experimentally found in chapter 4 and will be considered in more detail at the end of this section.

For the confirmation of the in the model described behaviour of the drilling process for different pulse durations, a comparison is made between the calculations and the experimental results which where shown in figure 4.6. For this comparison both the calculated drilled depths per pulse and the experimentally obtained average drilled depths per pulse are shown in figure 6.25. The calculated drilled depths are shown versus the laser power, which includes the absorptivity of the target surface and the attenuation of the laser beam by the plume. The laser power is obtained according to equation 6.25 with $A_0 = 0.14$, $c_1 = 0.4$ and $c_2 = 5 \cdot 10^5 (m^2 s)/kg$, the same absorptivity and coefficients as used to construct figure 6.19. In figure 6.25 it is clearly seen that the calculations and experiments agree rather well for the range of powers (more than 2 orders of magnitude) and for the range of pulse durations (more than one order of magnitude).

As for the results shown in figure 6.19 the results in figure 6.25 are used to calculate the efficiency of the drilling process. To study the efficiency of

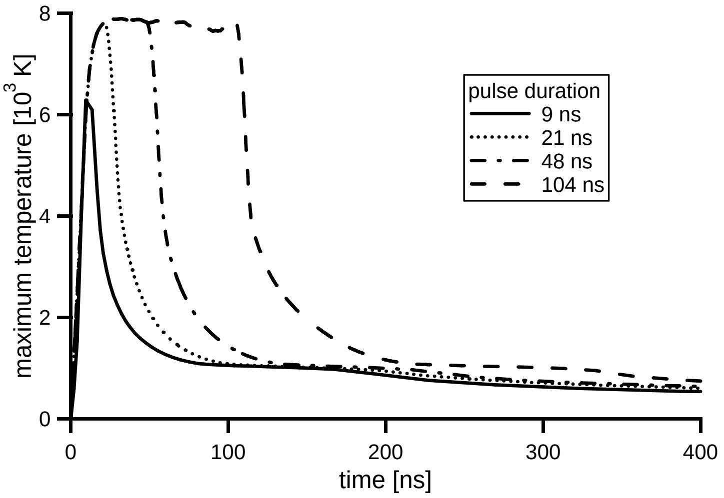

Figure 6.23: *The calculated maximum temperature versus the time for an absorbed power of 481 W for pulse durations of 9, 21, 48 and 104 ns (parameters of table 6.3, nr. B2, B8, B15 and B22).*

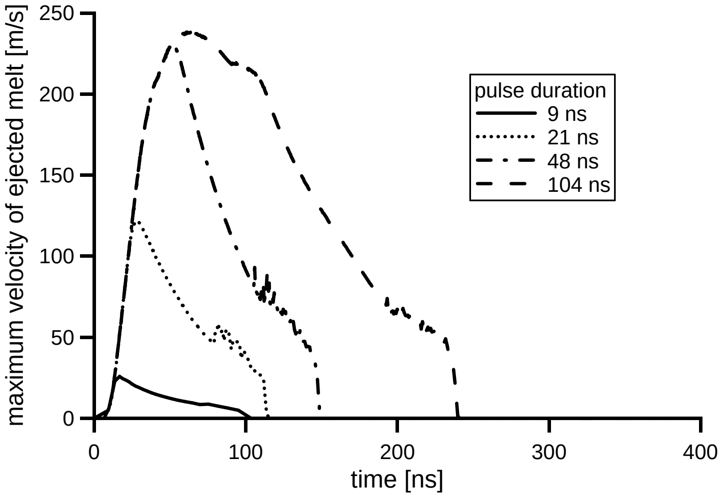

Figure 6.24: *The calculated maximum velocity versus the time for an absorbed power of 481 W for pulse durations of 9, 21, 48 and 104 ns (parameters of table 6.3, nr. B2, B8, B15 and B22).*

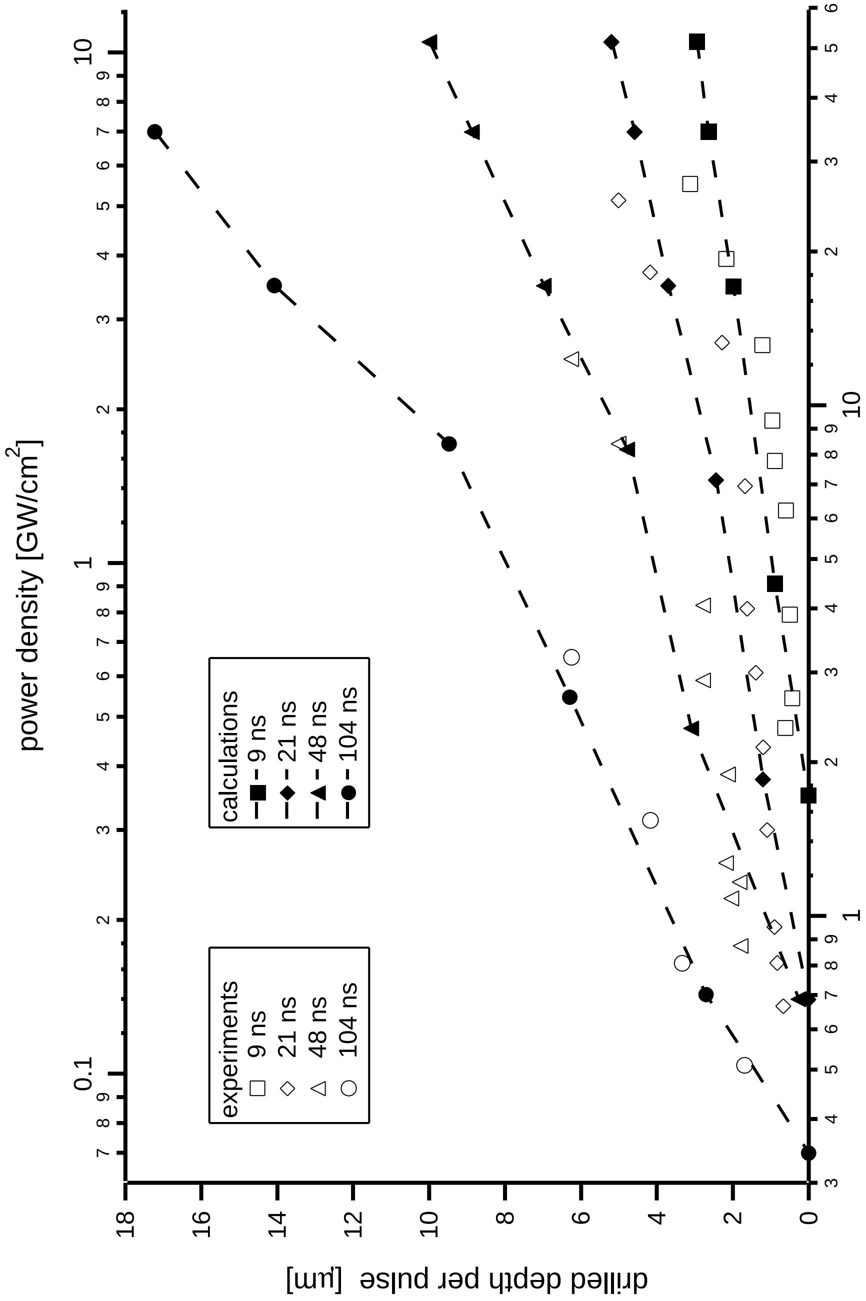

Figure 6.25: *The calculated drilled depth and the experimentally measured drilled depth per pulse versus the laser power for a pulse duration of 9, 21, 48 and 104 ns. (parameters of table 6.3). The dashed lines are constructed by interpolation between the calculated points, which are represented by the symbols.*

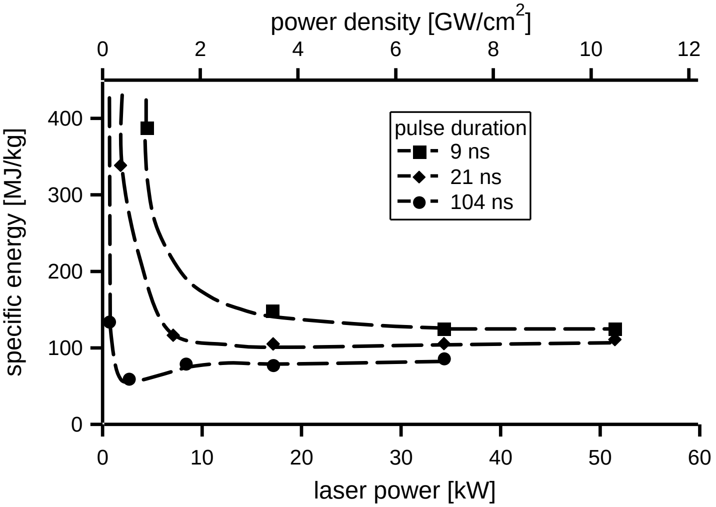

Figure 6.26: *The calculated specific energy versus the laser power (parameters of table 6.3, nr. B1-B11 and B19-B24). The dashed lines are constructed by interpolation between the calculated points, which are represented by the symbols.*

the laser drilling process for different pulse durations, the specific energy is calculated with inclusion of the absorptivity of the target surface and the attenuation of the laser beam by the plume. The results of these calculations are shown in figure 6.26 for three pulse durations of 9, 21 and 104 ns. With increasing power, for each of the pulse durations the specific energy decreases strongly and subsequently remains reasonably constant. It can be seen that the lowest specific energy, i.e., the highest efficiency can be found for the longest pulse of 104 ns around a laser power of 3 kW. Note that this behaviour was also found in the experiments described in section 4.2.1.

Summary

- For the studied range of powers (more than 2 orders of magnitude) and for the range of pulse durations (more than one order of magnitude) the calculations give a good explanation of the relevant processes in the experiments.

- This leads to the conclusion that the main physical processes involved in the hole drilling experiments have been properly taken into account in the model.
- For the higher power densities the drilled depth per pulse is still increasing.
- In the studied power range, long pulses use the pulse energy more efficiently for drilling than short pulses.

6.3.3 Calculations for different materials

In the experiments, besides aluminium, hole drilling in other application relevant target materials is studied. A comparison of experimental results with calculations is performed with the goal to justify the validity of the theoretical model for other materials. Calculations were performed with different pulse durations for two additional materials, iron and nickel. The parameters for these calculations are shown in table 6.4. The calculated and experimentally obtained drilled depths are shown in figure 6.27. The drilled depths per pulse were calculated for a constant laser power, to be able to make a fair comparison with experimental results. The laser power is assumed to be low enough to allow neglecting the attenuation of the laser beam by the plume, which is the situation that was found from the experimental data and will be verified by the calculations.

For the calculations the absorptivity (section 2.1) is taken as a constant, which only depends on the type of material and the wavelength of the laser used for drilling (compare with section 6.3.1.4). The simplification of taking a constant value for A_0 is justified because the calculations are performed for the first pulse on a flat surface, such that effects of multiple reflections and large incident angles can be safely neglected (section 2.1). The absorptivities, determined from the experimentally observations as shown in figure 6.27, while neglecting attenuation of the laser beam by the plume, are respectively A_0= 0.2, A_0= 0.55, and A_0= 0.55 for aluminium, nickel and iron. These values are compared with the absorptivities found in literature at room temperature for aluminium, nickel and iron, which are respectively A_0= 0.14, A_0= 0.55, and A_0= 0.56 (appendix B). For nickel and iron, the experimentally found absorptivities are in good agreement with the values found in the literature, which founds the assumption that attenuation of the laser beam by the plume can be safely neglected for the laser power in this experiment. For aluminium the absorptivity of A_0= 0.2,

Table 6.4: *Parameters used for the calculations with different materials for which material parameters are given in appendix B. The focus diameter* d_0 *is 32* μ*m. The pulse durations (FWHM) are varied and these are described by* t_1 *= 10 ns,* $t_2 = t_p$ *ns, and* $t_3 = t_p$ *+ 10 ns (figure 6.3). The laser power* P *= 2 kW. The separate calculations are numbered from C1 to C21.*

	target	t_p [ns]	E_{puls} [μJ] (laser)	E_{puls} [μJ] (absorbed)	P [W] (absorbed)	I [MW/cm^2] (absorbed)	depth [μm]
C1	Al	10	20	4	400	50	0.03
C2	”	25	50	10	”	”	1.61
C3	”	50	100	20	”	”	3.29
C4	”	75	150	30	”	”	4.71
C5	”	100	200	40	”	”	6.12
C6	”	125	250	50	”	”	7.43
C7	”	150	300	60	”	”	8.69
C8	Ni	10	20	11	1100	137	0.19
C9	”	25	50	27.5	”	”	0.70
C10	”	50	100	55	”	”	1.40
C11	”	75	150	82.5	”	”	2.07
C12	”	100	200	110	”	”	2.70
C13	”	125	250	137.5	”	”	3.42
C14	”	150	300	165	”	”	4.07
C15	Fe	10	20	11.2	1120	139	0.22
C16	”	25	50	28	”	”	0.76
C17	”	50	100	56	”	”	1.49
C18	”	75	150	84	”	”	2.19
C19	”	100	200	112	”	”	2.88
C20	”	125	250	140	”	”	3.60
C21	”	150	300	168	”	”	4.29

found from the experimental observations, is higher than the absorptivity found in literature. This can be expected because of the absorption of the laser beam by the plume for aluminium, even at low power, as was discussed in section 5.2.2.

Comparing the calculated drilled depths with the experimentally obtained drilled depths as shown in figure 6.27 shows the validity of the model for several metals. For nickel and iron, the influence of the plume can be safely neglected at the low powers in this experiment. The model gives a good estimation for the drilled depth for several materials in the studied pulse duration range.

Summary

- The achieved drilled depth per pulse depends mainly on the material properties for relative low powers.
- For drilling with low powers processes in the plume play a minor role.
- The validity of the developed model for laser drilling is demonstrated for aluminium, nickel and iron.

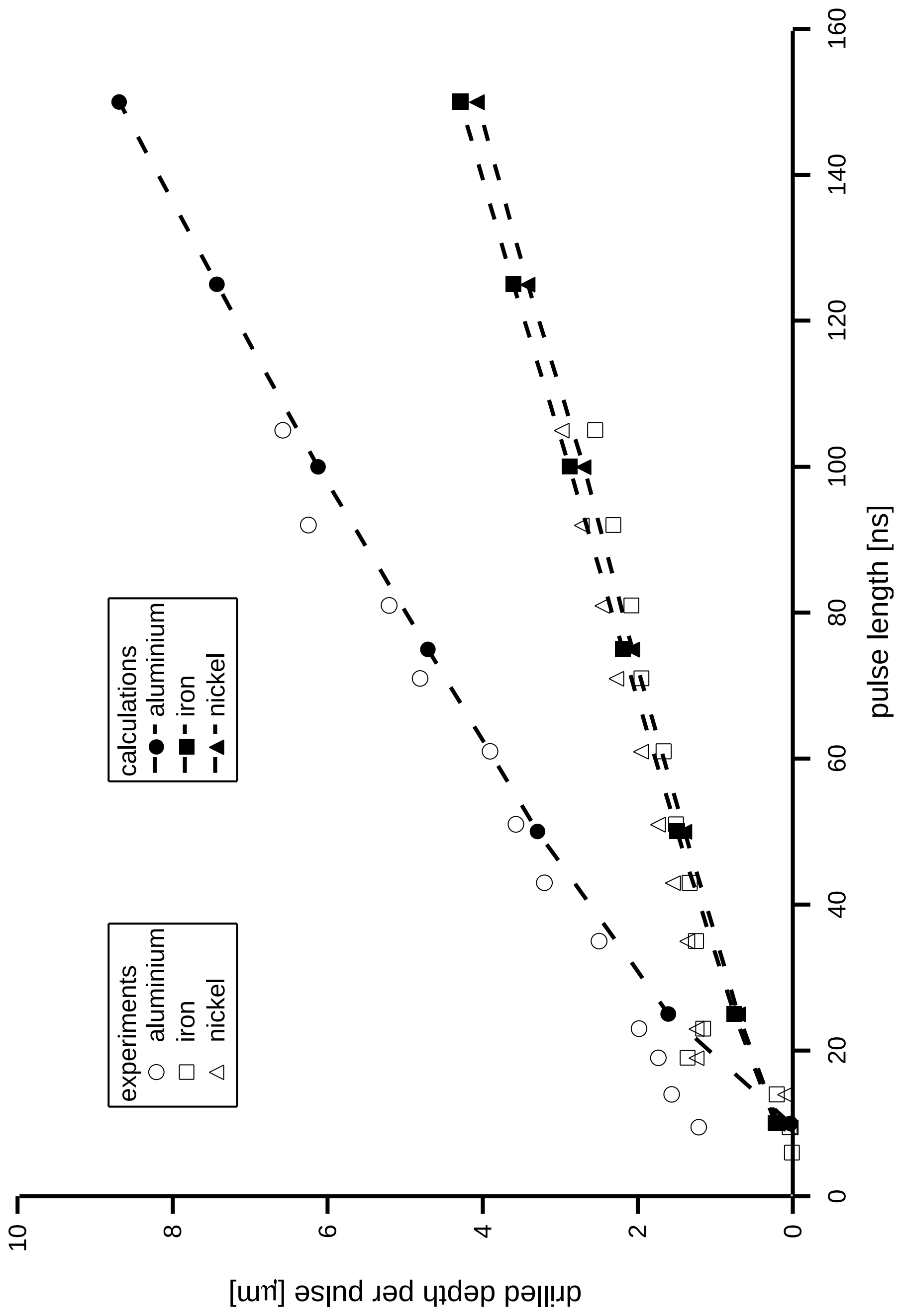

Figure 6.27: *The calculated and experimentally obtained drilled depth per pulse versus the pulse duration for aluminium, iron and nickel (parameters of table 6.4). The dashed lines are constructed by interpolation between the calculated points, which are represented by the symbols.*

Chapter 7

Summary

This thesis is about laser drilling with a unique excimer laser with a nearly diffraction-limited beam and relatively long optical pulse duration of 175 ns. The combination of high processing speed and high processing quality suitable for industrial applications can be obtained because the excellent beam quality enables usage of the entire beam instead of using mask projection techniques, which is common for excimer lasers. The research described in this thesis contributes to the fundamental understanding of the underlying processes for drilling metals with such a novel excimer laser, which is essential to achieve the highest processing speed and to control the quality of the drilled holes.

The thesis starts with a description of the different processes which play an important role: the heating of the material by the laser beam, the melting and evaporation, the build-up of recoil pressure as a consequence of the evaporation, and the interaction of the laser beam with the cloud of vapour and melt above the hole. The most important studied subjects are the influence of the laser pulse duration on the drilling process, the material removal during laser drilling, and the transparency of the plume at the wavelength of the drilling laser. Furthermore, a model of the laser drilling process is presented.

The experiments are done in the power regime where melt expulsion occurs, which is expected to be the most efficient process for the material removal. Material removal was experimentally studied for aluminium and Hastelloy X. The main amount of material removal in the experiments is seen at times relatively long after ending of the drilling pulse. The velocity of the melt reaches a maximum when the critical temperature is reached at the surface of the target. Calculations lead to the conclusion that the drilled depth depends strongly on the surface temperature of the target, which is directly related to the heat conductivity of the material. This implicates that heat conduction is an important parameter for the obtainable drilled depth. Furthermore, the surface temperature is strongly influenced by the attenuation of the laser beam by the plume. For drilling of aluminium, a simple model for attenuation of the laser beam by the plume gives a good explanation for the experimentally measured drilled depth. The validity of the developed model for laser drilling is demonstrated for aluminium, nickel and iron, which shows that the main physical processes involved in the hole drilling experiments have been properly taken into account in the model. With respect to efficiency, the drilling process is found to be the most efficient for a laser power at which melt ejection has just fully developed.

The optical transmission of the plume for the drilling laser is examined for aluminium, alumina, titanium, nickel, iron, silicon, copper and Hastelloy X. Aluminium and titanium vapours are not fully transparent for the laser beam, which can be accounted for, by the existence of absorption lines of the processed material at the laser wavelength. The other examined target materials showed highly transparent vapour between the target and the shockwave. For drilling with low powers processes in the plume play a minor role. The experiments indicate that for drilling with long pulses at higher power densities, the laser beam is not strongly attenuated by the plume, and even, the attenuation of the plume can decrease. This could be caused by absence of strong absorption or scattering by the plume at these power densities. Another reason may be that the vapour inside the hole supports the drilling process by additional heating, and by an increase of the recoil pressure, both, due to laser energy which is absorbed by the vapour.

The influence of the pulse duration on the drilling process is studied. The experimental work was done by using a pulse slicing method, which can provide an adjustable pulse duration while all other laser parameters, particularly the beam quality and shape, remain unchanged. It is found that with a long pulse, compared with a short pulse, the drilling speed during the pulse is lower, but on the other hand the holes are wider, so, the removed volume is higher. Calculations are performed with the developed model and are found to give a good explanation for the drilled depths measured in the experiments. As a conclusion for the influence of the pulse duration can be stated that long pulses use the pulse energy more efficiently for drilling than short pulses.

Bibliography

T. Abeln, J. Radtke, and F. Dausinger. High precision drilling with short-pulsed solid-state lasers. In *Proceedings of ICALEO 1999*, volume 88, pages 195–203, 1999.

M. von Allmen and A. Blatter. *Laser-Beam Interactions with Materials*. Springer, 2^{nd} edition, 1995.

S. Amoruso, R. Bruzzese, N. Spinelli, and R. Velotta. Characterization of laser-ablation plasmas. *J. Phys. B: At. Mol. Opt. Phys.*, 32:R131–R172, 1999.

S.I. Anisimov. Vaporization of metal absorbing laser radiation. *Soviet Physics JETP*, 27(1):182–183, 1968.

P.W. Atkins. *Physical Chemistry*. Oxford University Press, 3^{rd} edition, 1986.

N.G. Basov, V.A. Danilychev, and Y.M. Popov. Stimulated emission in the vacuum ultraviolet region. *Soviet Journal of Quantum Electronics*, 1(1):18–22, 1971.

D. Basting. *Excimer Laser Technology: laser sources, optics, systems and applications*. Lambda Physik AG, 2001.

D. Bäuerle. *Laser Processing and Chemistry*. Springer, 3^{rd} edition, 2000.

A. Bejan. *Heat transfer*. John Wiley and Sons, Inc., 1993.

J. Bell. Industrial 1 kW excimer moves into production. *OLE*, pages 15–19, June 1996.

D. Breitling, A. Ruf, P.W. Berger, F.H. Dausinger, S.M. Klimentov, P.A. Pivovarov, T.V. Kononenko, and V.I. Konvov. Plasma effects during ablation and drilling using pulsed solid-state lasers. In *Proceedings of Laser Processing of Advanced Materials and Laser Microtechnologies*, volume 5221, pages 24–33, 2003.

D. Breitling, H. Schittenhelm, P. Berger, F. Dausinger, and H. Hügel. Shadowgraphic and interferometric investigations on Nd:YAG laser-induced vapor/plasma plumes for different processing wavelengths. *Appl. Phys. A*, 69: S505–S508, 1999.

X. Chen and X. Liu. Short pulsed laser machining: How short is short enough? *J. Laser Appl.*, 11(6):268–272, 1999.

Comsol AB. Manuals FemLab. (http://www.femlab.com).

F. Dausinger. Drilling of high quality micro holes. In *Proceedings of ICALEO 2000*, volume 89B, pages 1–9, 2000.

F. Dausinger, T. Abeln, D. Breitling, J. Radtke, V.I. Konov, S.V. Garnov, S.M. Klimentov, T.V. Kononenko, and O. Tsarkova. Drilling of ceramics with short-pulsed solid-state lasers. *LaserOpto*, 31(3):78–85, 1999.

P.E. Dyer and J. Sidhu. Spectroscopic and fast photographic studies of excimer laser polymer ablation. *J. Appl. Phys.*, 64(9):4657–4663, 1988.

A. Einstein. Zur Quantentheorie der Strahlung. *Physikalische Zeitschrift*, 18: 121–128, 1917. In German.

J.P. Gordon, H.J. Zeiger, and C.H. Townes. The maser - new type of microwave amplifier, frequency standard, and spectrometer. *Physical Review*, 99:1264–1274, 1955.

D.G. Gray. *American Institute of Physics Handbook*. McGraw-Hill Book Company, 3^{rd} edition, 1972.

P.M. Gresho and R.L. Sani. *Incompressible Flow and the Finite Element Method*. John Wiley and Sons, Inc., 1998.

Handbook of Chemistry and Physics. *Handbook of Chemistry and Physics*. CRC press Inc., 66^{th} edition, 1985.

E. Hecht. *Optics*. Addison Wesley Longman, Inc., 3^{rd} edition, 1998.

R.M. Hofstra. *On the optical performance of the long pulse XeCl* excimer laser*. PhD thesis, University of Twente, 1999.

R.M. Hofstra, J.C.M. Timmermans, and H.J.G. Van Heel. On the optical quality of NCLR's 1 kW, 1 kHz XeCl excimer laser. In *Proceedings of Advanced High-Power Lasers*, volume 3889, pages 388–395, 2000.

R.M. Hofstra, F.A. van Goor, and W.J. Witteman. Beam divergence studies on hard edge unstable resonators for a long pulse XeCl excimer laser. *Optics Communications*, 144:43–49, 1997.

R.M. Hofstra, F.A. van Goor, and W.J. Witteman. Linewidth reduction of a long-pulse, low-gain XeCl* laser with intracavity etalons. *J. Opt. Soc. Am. B*, 16 (7):1068–1071, 1999.

R.M. Hofstra, M.J. Zwegers, F.A. van Goor, and W.J. Witteman. On the beam pointing variation of a long pulse XeCl* excimer laser fitted with unstable resonators. *Optics Communications*, 157:121–127, 1998.

T. Iida and R.I.L. Guthrie. *The physical properties of liquid metals*. Oxford University Press, 1988.

T.E. Itina, H. Hermann, Ph. Delaporte, and M. Sentis. Combined continuous-microscopic modeling of laser plume expansion. *Appl. Surf. Sci.*, 208-209: 27–23, 2003.

A. Kar and J. Mazumder. Mathematical model for laser ablation to generate nanoscale and submicrometer-size particles. *Phys. Rev. E*, 49(1):410–419, 1994.

A. Kar, T. Rockstroh, and J. Mazumder. Two-dimensional model for laser-induced materials damage: Effects of assist gas and multiple reflections inside the cavity. *J. Appl. Phys.*, 6:2560–2569, 1992.

I.G. Karasev, V.M. Kirillov, V.É. Norskii, V.I. Samoilov, and P.I. Ulyakov. Disintegration of metals by a laser beam. *Soviet Physics - Technical Physics*, 15 (9):1523–1527, 1971.

H. Ki, P.S. Mohanty, and J. Mazumder. Multiple reflection and its influence on keyhole evolution. *Journal of Laser Applications*, 14(1):39–45, 2002.

C.J. Knight. Theoretical modeling of rapid surface vaporization with back pressure. *AIAA J.*, 17(5):519–523, 1979.

F. Kokai, K. Takahashi, K. Shimizu, M. Yudasaka, and S. Iijima. Shadowgraphic and emission imaging spectroscopic studies of the laser ablation of graphite in an Ar gas atmosphere. *Appl. Phys. A*, 69:S223–S227, 1999.

G. Koren, R.J. Baseman, A. Gupta, M.I. Lutwyche, and R.B. Laibowitz. Particulates reduction in laser-ablated $YBa_2Cu_3O_{7-\delta}$ thin films by laser induced plume heating. *Appl. Phys. Lett.*, 56(21):2144–2146, 1990.

G. Lang. Kritische Temperaturen und Temperaturkoeffizienten der Oberflächenspannung flüssiger Metalle. *Z. Metallkde.*, 68:213–218, 1977. In German.

D.F. de Lange, S. Postma, and J. Meijer. Modelling and observation of laser welding: The effect of latent heat. In *Proceedings of ICALEO 2003 (on CD)*, volume Section C, pages 154–162, 2003.

T.H. Maiman. Stimulated optical radiation in ruby. *Nature*, 187:493–494, 1960.

T.J. McKee. Optical cavity design for long pulse excimer lasers. *Appl. Opt.*, 30: 635–644, 1991.

G. Mehlman, D.B. Chrisey, P.G. Burkhalter, J.S. Horwitz, and D.A. Newman. Vacuum ultraviolet spectroscopy study of excimer-laser-generated plasmas. *J. Appl. Phys.*, 74:53–61, 1993.

L. Migliore. *Laser materials processing*. Marcel Dekker, Inc., 1996.

J. Milewski and E. Sklar. Modelling and validation of multiple reflections for enhanced laser welding. *Modelling Simul. Mater. Sci. Eng.*, 4:305–322, 1996.

K.C. Mills. *Recommended values of thermophysical properties for selected commercial alloys*. Woodhead Publishing Limited, 2002.

A. Miotello and R. Kelly. Laser-induced phase explosion: new physical problems when a condensed phase approaches the thermodynamic critical temperature. *Appl. Phys. A*, 69:S67–S73, 1999.

A.A. Morozov. Thermal model of pulsed laser ablation: back flux contribution. *Appl. Phys. A*, 79:997–999, 2004.

R. Niedrig and O. Bostanjoglo. Imaging and modeling of pulse laser induced evaporation of metal films. *J. Appl. Phys.*, 81(1):480–485, 1997.

A.M. Prokhorov, V.I. Konov, I. Ursu, and I.N. Mihăilescu. *Laser Heating of Metals*. Adam Hilger, 1990.

J.F. Ready and D.F. Farson. *LIA Handbook of Laser Materials Processing*. Laser Institute of America, 2001.

W.M. Rohsenow and H.Y. Choi. *Heat, Mass, Momentum transfer*. Prentince-Hall, Inc., 1961.

A. Ruf, D. Breitling, P. Berger, F. Dausinger, and H. Hügel. Hydrodynamical modeling of laser drilling with short and ultrashort pulses. In *Proceedings of 12th International School on Quantum Electronics: Laser Physics and Applications*, volume 5226, pages 367–371, 2003.

A. Ruf, G. Callies, P. Berger, and H. Hügel. Influence of multiple reflections on hole shape during laser drilling. In *Proceedings on M^4PL14 The 14th Meeting on Mathematical Modelling of Materials Processing with Lasers*, volume 6, 1999.

A.L. Schawlow and C.H. Townes. Infrared and optical masers. *Physical Review*, 112:1940–1949, 1958.

H. Schittenhelm, G. Callies, P. Berger, and H. Hügel. Investigations of extinction coefficients during excimer laser ablation and their interpretation in terms of rayleigh scattering. *J. Phys. D: Appl. Phys.*, 29:1564–1575, 1996.

H. Schittenhelm, G. Callies, A. Straub, P. Berger, and H. Hügel. Measurements of wavelength-dependent transmission in excimer laser-induced plasma plumes and their interpretation. *J. Phys. D: Appl. Phys.*, 31:418–427, 1998.

V.V. Semak, J.T. Schriempf, G.A. Knorovsky, and D.O. MacCallum. Application of melt ejection criterion in simulation of micromachining with laser. In *Proceedings of Photon Processing in Microelectronics and Photonics II*, volume 4977, pages 530–541, 2003.

E. Sicard, C. Boulmer-Leborgne, C. Andreazza-Vignolle, and M. Frainais. Excimer laser surface treatment of aluminium alloy in nitrogen. *Appl. Phys. A*, 73:55–60, 2001.

A.E. Siegman. *Lasers*. University Science Books, 1986.

P. Solana and G. Negro. A study of the effect of multiple reflections on the shape of the keyhole in the laser processing of materials. *J. Phys. D: Appl. Phys.*, 30:3216–3222, 1997.

K.H. Song and X. Xu. Explosive phase transformation in excimer laser ablation. *Appl. Surf. Sci.*, 127-129:111–116, 1998.

W.M. Steen. *Laser material processing*. Springer, 3^{rd} edition, 1998.

J.C.M. Timmermans. *Double discharge XeCl-laser*. PhD thesis, University of Twente, 1995.

J.C.M. Timmermans, R.M. Hofstra, J. Couperus, R. Kleijhorst, H. Prins, G. Oude Meijers, and H.J.G. Van Heel. Development of NCLR's 1 kW XeCl laser. In *Proceedings of Advanced High-Power Lasers*, volume 3889, pages 360–367, 2000.

H.G. Treusch. *Geometrie und Reproduzierbarkeit einer Plasmaunterstützten Materialabtragung durch Laserstrahlung*. PhD thesis, Technischen Hochschule Darmstadt, 1985. In German.

K. Ujihara. Reflectivity of metals at high temperatures. *J. Appl. Phys.*, 43(5): 2376–2383, 1972.

O. Uteza, N. Destouches, Ph. Delaporte, B. Fontaine, and M. Sentis. Nanosecond high-energy oscillator: regenerative amplifier excimer laser system. In *Proceedings of Advanced High-Power Lasers*, volume 3889, pages 368–378, 2000.

K.T. Voisey, T. Klocker, and T.W. Clyne. Measurement of melt ejection velocities during laser drilling of steel, using a novel droplet stream interception technique. *Acta Mater.*, 50:4219–4230, 2002.

K.T. Voisey, W. Rodden, D. Hand and T.W. Clyne. Melt ejection characteristics during laser drilling of metals. In *Proceedings of ICALEO 2001 (on CD)*, 2001.

S.W. Williams, P.J. Marsden, N.C. Roberts, J. Sidhu, and M.A. Venables. Excimer laser beam shaping and material processing using diffractive optics. In *Proceedings of High power Laser Ablation*, volume 3343, pages 205–211, 1998.

J.H. Yoo, S.H. Jeong, R. Greif, and R.E. Russo. Explosive change in crater properties during high power nanosecond laser ablation of silicon. *J. Appl. Phys.*, 88(3):1638–1649, 2000.

Appendix A

List of symbols

symbol	quantity	unit
		-
A	absorbed fraction of energy	-
A_0	absorbed fraction of energy at room temperature	-
A_c	cross-sectional area	m^2
a	thermal diffusivity $= k/(\rho\, c)$	m^2/s
c	specific heat	J/(kg K)
c_1	constant	-
c_2	constant	kg/(s m^2)
c_p	specific heat at constant pressure	J/(kg K)
D	beam diameter	m
d_0	spot diameter in focus	m
E	energy	J
E_{att}	attenuated part of the laser energy	J
E_{con}	conducted energy	J
E_{laser}	energy of the laser beam	J
E_{melt}	energy necessary for melting	J
E_{puls}	pulse energy	J
E_{ref}	reflected laser energy	J
E_{vap}	energy necessary for vaporization	J
F	force	N
F_b	boundary force	N
F_l	fluence	J/m^2
F_v	volume force	N

$\vec{\mathcal{F}}_v$	external or volume force	N/m^3
Fo	Fourier number	-
f	focal length	m
f_f	external force function	
f_p	pulse shape function	
$H(T)$	enthalpy as function of the temperature	J/kg
$H_{v,m}$	molar entropy of the vapour	J/mol
h	thickness	m
I	power density	W/m^2
I_0	power density at $r = 0$	W/m^2
I_{1/e^2}	average power density over the $1/e^2$ spot diameter	W/m^2
$\vec{\mathbf{K}}$	viscous force per unit area	N/m^2
k	thermal conductivity	W/(m K)
k^*	scaled thermal conductivity	-
k_0	scaling factor for the thermal conductivity	W/(m K)
k_B	Bolzmann constant ($1.38 \cdot 10^{-23}$)	J/K
L	length	m
L_0	scaling factor for the length	m
L_m	latent heat for melting	J/kg
L_v	latent heat for vaporisation	J/kg
l_d	diffusion length	m
l_α	absorption length	m
m	mass	kg
$\dot{m}$	net vaporized mass flow rate	kg/(s m^2)
$\dot{m}_{av}$	average vaporized mass flow rate	kg/(s m^2)
$\dot{m}_v$	vaporized mass flow rate	kg/(s m^2)
n	integer	-
n	coordinate in the direction normal to the surface	m
$\vec{n}$	normal vector	
n_1	refractive index	-
n_2	extinction coefficient	-
$\vec{\mathbf{n}}_r$	complex index of refraction (n$_1$ + i n$_2$)	
P	power	W
p	pressure	Pa
p_0	vapour pressure under normal conditions ($1 \cdot 10^5$)	Pa
p_r	recoil pressure	Pa
Q	internal heat generation	W/m^3
$\vec{q}$	heat flow rate per surface unit	W/m^2
q_l	heat flow rate supplied by the laser beam	W/m^2

q_m	mass flow rate	kg/s
q_v	heat flow rate necessary for vaporization	W/m^2
q_x	heat flow rate per surface unit in Cartesian coordinates	W/m^2
q_y	heat flow rate per surface unit in Cartesian coordinates	W/m^2
q_z	heat flow rate per surface unit in Cartesian coordinates	W/m^2
R	reflectivity	-
R_1, R_2	mirror radius	m
R_m	molar gas constant = 8.314	J/(mol K)
Re	Reynolds number	-
r	radial coordinate	m
r_m	radius melt pool	m
S_m	molar entropy	J/(mol K)
s	coordinate along the boundary	m
T	temperature	K
T_0	scaling factor for the temperature	K
T_b	boiling temperature at normal pressure	K
T_c	critical temperture	K
T_m	melting temperature	K
t	time	s
$\vec{t}$	tangential vector	-
t_0	scaling factor for the time	s
t_1	parameter for temporal pulse shape (figure 6.3)	s
t_2	parameter for temporal pulse shape (figure 6.3)	s
t_3	parameter for temporal pulse shape (figure 6.3)	s
t_{ej}	time until ejection of melt	s
t_m	time between melting and solidification of the material	s
t_p	pulse duration	s
V_m	molar volume	m^3/mol
$\vec{\mathbf{v}}$	velocity vector	m/s
v_0	scaling factor for the velocity	m/s
v_m	melt velocity	m/s
v_{sl}	velocity of the solid-liquid interface	m/s
v_x	velocity in Cartesian coordinates	m/s
v_y	velocity in Cartesian coordinates	m/s
v_z	velocity in Cartesian coordinates	m/s
w	radius of a Gaussian beam	m
w_0	waist radius of a Gaussian beam	m
x	Cartesian coordinate	m
y	Cartesian coordinate	m

z	axial position in cylindrical coordinates	m
z_R	Rayleigh length	m
Z_w	number of collisions	1 /(s m^2)

Greek

α	optical absorption coefficient	1/m
$\delta\Omega$	boundary	
η	dynamic viscosity	Ns/m^2
θ_d	divergence	rad
θ_i	incidence angle	degree
λ	wavelength	m
Φ	heat flow rate	W
ρ	mass density	kg/m^3
σ	normal stress	N/m^2
σ_n	standard deviation	-
τ	tangential stress	N/m^2
Ω	domain	
Ω_s	solid domain	
Ω_m	melt domain	
Ω_m	plume domain	

Abbreviations

FWHM	Full Width at Half Maximum
MOPA	Master Oscillator, Power Amplifier
SEM	Scanning Electron Microscope

Appendix B

Material parameters

Table B.1 shows the material parameters used in this thesis. Generally, these parameters are according to Bäuerle (2000), otherwise, the source is indicated with a small number, respectively (1) for Ready and Farson (2001), (2) for Lang (1977), (3) for Iida and Guthrie (1988), and (4) for Mills (2002). For the specific heat, c, the specific heat at constant pressure, c_p, is used. The absorptivity A_0 is given for a wavelength λ of 305 nm.

Table B.1: *Material parameters.*

symbol	unit	Al	Ni	Cu	Fe	Ti	Hast-X
ρ	kg/m^3	2700	8900	8940	7860	4520	8240(4)
a	10^{-4} m^2/s	1.03	0.24	1.14	0.23	0.094	
k	W/(m K)	237	89	400	84	22	10(4)
c_p	J/(kg K)	900	440	390	460	520	439(4)
L_m	10^6 J/kg	0.41	0.31	0.20	0.27	0.41	
L_v	10^6 J/kg	10.75	6.4	4.7	6.3	8.8	
$H_{v,m}$	10^3 J/mol	290	307	300	350	420	
T_m	K	933	1727	1357	1808	1933	1260-1355(4)
T_b	K	2730	3095	2840	3023	3560	
T_c(2)	K	8560	10770	8990	10430	12560	
η	10^{-3} Ns/m^2	2(3)	5.5(3)		7(3)		7.5(4)
A_0		0.14	0.55(1)	0.75(1)	0.56(1)		

Appendix C

Heat transfer and melt flow

In this appendix the equations used for calculations of heat transfer and melt flow are derived.

C.1 Heat transfer

The first law of thermodynamics states the conservation of energy (Bejan, 1993). Taking into account the heat transfer by conduction and by convection the heat balance for an infinitesimal volume element can be written in accordance with this law as:

$$\Phi_{(el)} + \Phi_{(cond,in)} - \Phi_{(cond,out)} + \Phi_{(conv,in)} - \Phi_{(conv,out)} = 0 \tag{C.1}$$

with $\Phi_{(el)}$ the change of internal energy per unit of time for the total element. $\Phi_{(cond,in)}$ and $\Phi_{(cond,out)}$ are respectively the heat flow rate into and the heat flow rate out of the element through the boundaries by conduction. $\Phi_{(conv,in)}$ and $\Phi_{(conv,out)}$ are respectively the heat flow rate into and the heat flow rate out of the element with the material crossing the boundaries by convection. The equations are derived for incompressible flow. The different terms will be derived.

Internal energy

The internal energy dE of an infinitesimal volume element is

$$dE = dm\, c T = \rho\, c T\, dx\, dy\, dz \tag{C.2}$$

where dm is the mass of the element, c is the specific heat, T is the temperature, ρ is the mass density, and x, y and z are the cartesian coordinates. The change

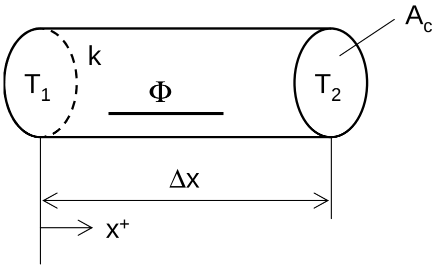

Figure C.1: *Heat transfer by one-dimensional conduction.*

of the internal energy, per unit of time t, for the element is

$$\Phi_{(el)} = \frac{\partial E}{\partial t} = \rho\, c\, \frac{\partial T}{\partial t} dx\, dy\, dz. \tag{C.3}$$

Heat transfer by conduction

The second and third term on the right side of equation C.1 take into account the heat transfer rate by conduction, which occurs under influence of a temperature gradient. Consider for example the cylinder of figure C.1, which is isolated at the casing. A_c is the cross-sectional area. The temperature gradient over a distance Δx is $\Delta T = T_2 - T_1$. The Fourier law of heat conduction defines the heat flow rate Φ in the x-direction (Bejan, 1993)

$$\Phi_{x(cond)} = -A_c\, k \frac{\Delta T}{\Delta x} \tag{C.4}$$

where k is the thermal conductivity. The heat flow rate into the element through the boundary in the x-direction of the element by conduction is

$$\Phi_{x(cond,in)} = q_{x(cond)}(x, y, z) dy\, dz \tag{C.5}$$

with q the density of heat flow rate, i.e, the heat flow rate per surface unit. The heat flow rate out of the element through the boundary in the x-direction of the element by conduction, developed in a first order Taylor series gives

$$\begin{aligned} \Phi_{x(cond,out)} &= q_{x(cond)}(x + dx, y, z) dy\, dz \qquad \text{(C.6)} \\ &= \left(q_{x(cond)}(x, y, z) + \frac{\partial q_{x(cond)}(x, y, z)}{\partial x} dx \right) dy\, dz. \end{aligned}$$

In analogy, the sum of the heat flow rate in all three directions through the element boundaries by conduction is

$$\begin{aligned}
&\Phi_{(cond,in)} - \Phi_{(cond,out)} \qquad \text{(C.7)}\\
&= -\left(\frac{\partial q_{x(cond)}}{\partial x} + \frac{\partial q_{y(cond)}}{\partial y} + \frac{\partial q_{z(cond)}}{\partial z}\right) dx\,dy\,dz\\
&= -\nabla\cdot\vec{\mathrm{q}}_{(cond)}\,dx\,dy\,dz\\
&= -\nabla\cdot\left(-k\left(\frac{\partial T}{\partial x},\frac{\partial T}{\partial y},\frac{\partial T}{\partial z}\right)\right) dx\,dy\,dz\\
&= -\nabla\cdot(-k\nabla T)\,dx\,dy\,dz.
\end{aligned}$$

Heat transfer by convection

The heat flow rate into the element with the material crossing the boundaries in the x-direction of the element by convection $\Phi_{x(conv,in)}$, is

$$\Phi_{x(conv,in)} = c\,\rho\,T(x,y,z)\,v_x(x,y,z)\,dy\,dz \qquad \text{(C.8)}$$

where v is the velocity. The heat flow rate out of the element with the material crossing the boundaries in the x-direction of the element by convection, $\Phi_{x(conv,out)}$, developed in a first order Taylor series is

$$\begin{aligned}
\Phi_{x(conv,out)} &= c\,\rho\,T(x+dx,y,z)\,v_x(x+dx,y,z)\,dy\,dz \qquad \text{(C.9)}\\
&= c\,\rho\left(T(x,y,z) + \frac{\partial T(x,y,z)}{\partial x}dx\right)\left(v_x(x,y,z) + \frac{\partial v_x(x,y,z)}{\partial x}dx\right) dy\,dz.
\end{aligned}$$

The heat flow rate into the element $\Phi_{x(conv,in)}$ minus the heat flow rate out of the element $\Phi_{x(conv,out)}$ with the material crossing the boundaries in the x-direction of the element by convection is

$$\begin{aligned}
&\Phi_{x(conv,in)} - \Phi_{x(conv,out)} \qquad \text{(C.10)}\\
&= -c\,\rho\left(T(x,y,z)\frac{\partial v_x(x,y,z)}{\partial x} + v_x(x,y,z)\frac{\partial T(x,y,z)}{\partial x}\right.\\
&\left. + \frac{\partial v_x(x,y,z)}{\partial x}\frac{\partial T(x,y,z)}{\partial x}dx\right) dx\,dy\,dz.
\end{aligned}$$

This equation can be simplified. First of all, the last term between the brackets in equation C.10 is a second derivative and small compared to the other terms and will be neglected. For incompressible flow, the total mass flow rate into the element has to be equal to the total mass flow rate out of the element, known as the mass conservation principle (Bejan, 1993). The mass flow rate into the element $q_{m,x(in)}$ in the x-direction is

$$q_{m,x(in)} = \rho\, v_x(x,y,z)\, dy\, dz. \tag{C.11}$$

The mass flow rate out of the element $q_{m,x(out)}$ in the x-direction, developed in a Taylor series while leaving out the higher order terms, is

$$q_{m,x(out)} = \rho\, v_x(x+dx,y,z)\, dy\, dz = \rho \left(v_x(x,y,z) + \frac{\partial v_x(x,y,z)}{\partial x} dx \right) dy\, dz. \tag{C.12}$$

The mass conservation principle after summation of the mass flow rates in all three directions can be written as

$$\begin{aligned} & q_{m(in)} = q_{m(out)} && \text{(C.13)} \\ ,[1ex] \qquad & \frac{\partial v_x}{\partial x} + \frac{\partial v_y}{\partial y} + \frac{\partial v_z}{\partial z} = 0, \\ & \nabla \cdot \vec{\mathbf{v}} = 0. \end{aligned}$$

This equation is used to simplify equation C.10. The sum of the heat flow rate in all directions of the material crossing the element boundaries by convection can now be written as

$$\begin{aligned} & \Phi_{(conv,in)} - \Phi_{(conv,out)} && \text{(C.14)} \\ & = -c\,\rho \left(v_x \frac{\partial T}{\partial x} + v_y \frac{\partial T}{\partial y} + v_z \frac{\partial T}{\partial z} \right) dx\, dy\, dz = -c\,\rho\, \vec{\mathbf{v}} \cdot \nabla T\, dx\, dy\, dz. \end{aligned}$$

Inserting equations C.3, C.7 and C.14 into equation C.1 gives

$$c\,\rho \frac{\partial T}{\partial t} = \nabla \cdot (k \nabla T) - c\,\rho\, \vec{\mathbf{v}} \cdot \nabla T. \tag{C.15}$$

This equation is the basis for calculating the heat transfer in an incompressible, liquid medium subjected to a given temperature distribution and flow distribution. In this equation the term on the left hand side represents the change of the accumulated heat in the material. The first term on the right hand side represents heat conduction under the influence of a temperature gradient. The second term on the right side represents heat transport by convection through a flow of the medium. In this thesis two axisymmetric coordinates instead of Cartesian coordinates were used for the calculations, in order to provide a significant increase of the speed of the numerical simulations.

C.2 Navier Stokes equations

In this section the equations used for modelling the melt flow are explained briefly. These equations will be derived to make clear which aspects of melt flow are taken into acount in the calculations in this thesis. The resulting equations are named the Navier Stokes equations (Bejan, 1993). The second law of Newton and the mass conservation principle (Bejan, 1993) are the basics used for derivation of these equations. The fluid flow is described with macroscopic and continuous quantities such as pressure, temperature and velocity, which is the result of the mean behaviour of large quantities of atoms or molecules. For this, an infinitesimal element is considered, with enough atoms or molecules to consider it as a continuum. The fluid is considered as incompressible, i.e., changes in pressure cause no changes in mass density.

The second law of Newton in Cartesian coordinates can be written as

$$\Sigma\vec{\mathbf{F}} = \frac{d(m\vec{\mathbf{v}})}{dt} \tag{C.16}$$

where $\Sigma\vec{\mathbf{F}}$ is the sum of the forces working on the element and the right hand side of equation C.16 is the resulting change of momentum of the element. The forces can be divided in volume forces (or external forces) and in boundary forces. The external forces work without contact, such as gravity and electro-magnetic forces. The surface forces act on the boundaries of the elements by direct contact. To obtain the surface forces working on the infinitesimal element, the forces per surface unit, the stresses, are considered. There is a difference in how solids and fluids withstand tangential stresses. Solid material can withstand a tangential stress with a limited deformation. A fluid under the influence of a constant tangential stress reaches a dynamic equilibrium, where it reacts to the tangential stress with a velocity of deformation. The velocity of deformation at a given tangential stress, τ, depends on the material. For many fluids, the magnitude of the tangential stress is proportional with the velocity of deformation, dv/dx. These fluids are named ’Newtonian fluids’. The proportionality constant is named the dynamic viscosity η. In one-dimensional form the viscosity law of Newton is (Rohsenow and Choi, 1961)

$$\tau = \eta \frac{dv}{dx} \tag{C.17}$$

In three dimensions, the stress acting on the element can be written as a stress tensor

$$\begin{bmatrix} \sigma_{xx} & \tau_{xy} & \tau_{xz} \\ \tau_{yx} & \sigma_{yy} & \tau_{yz} \\ \tau_{zx} & \tau_{zy} & \sigma_{zz} \end{bmatrix} \tag{C.18}$$

where the symbol σ is used for normal stress from forces working perpendicular on the considered plane, and where τ is used for tangential stress from forces working within the considered plane. The first subscript denotes the plane on which the stress acts, and the second subscript gives the direction on that face. The sum of the forces in the x-direction ΣF_x is the sum of the boundary forces $F_{b,x}$ and the volume forces $F_{v,x}$ in this direction

$$\Sigma F_x = \Sigma F_{b,x} + \Sigma F_{v,x} \tag{C.19}$$

Boundary forces

The sum of the boundary forces in x-direction is

$$\begin{aligned} \Sigma F_{b,x} &= \sigma_{xx}(x,y,z)\,dy\,dz - \sigma_{xx}(x+dx,y,z)\,dy\,dz \\ &+\tau_{yx}(x,y,z)\,dx\,dy - \tau_{yx}(x,y+dy,z)\,dx\,dy \\ &+\tau_{zx}(x,y,z)\,dx\,dz - \tau_{zx}(x,y,z+dz)\,dx\,dz \end{aligned} \tag{C.20}$$

This expression can be simplified using a first order Taylor series expansion

$$\Sigma F_{b,x} = -\left(\frac{\partial \sigma_{xx}}{\partial x} + \frac{\partial \tau_{yx}}{\partial y} + \frac{\partial \tau_{zx}}{\partial z}\right) dx\,dy\,dz \tag{C.21}$$

For Newtonian fluids, normal and tangential stresses in terms of the velocity are (Rohsenow and Choi, 1961)

$$\sigma_{xx} - p = -2\eta \frac{\partial v_x}{\partial x} + \frac{2}{3}\eta \left(\frac{\partial v_x}{\partial x} + \frac{\partial v_y}{\partial y} + \frac{\partial v_z}{\partial z}\right) \tag{C.22}$$

$$\tau_{yx} = \eta \left(\frac{\partial v_x}{\partial y} + \frac{\partial v_y}{\partial x}\right) \tag{C.23}$$

$$\tau_{zx} = \eta \left(\frac{\partial v_x}{\partial z} + \frac{\partial v_z}{\partial x} \right) \tag{C.24}$$

Because $\nabla \cdot \vec{\mathbf{v}} = 0$ (equation C.13) for incompressible fluids, equation C.21 can be written as

$$\Sigma F_{b,x} = -\left(\frac{\partial}{\partial x} \left(p - 2\eta \frac{\partial v_x}{\partial x} \right) \right. \tag{C.25}$$
$$\left. +\eta \left(\frac{\partial v_x}{\partial y} + \frac{\partial v_y}{\partial x} \right) + \eta \left(\frac{\partial v_x}{\partial z} + \frac{\partial v_z}{\partial x} \right) \right) dx\, dy\, dz$$

The same can be done for the y and z-direction. The equations for all three directions can be written in short form

$$\overrightarrow{\Sigma F_b} = -\left(\nabla p - \nabla \cdot \eta \left(\nabla \vec{\mathbf{v}} + (\nabla \vec{\mathbf{v}})^T \right) \right) dx\, dy\, dz \tag{C.26}$$

where $(\nabla \vec{\mathbf{v}})^T$ is the transposed of $(\nabla \vec{\mathbf{v}})$. For constant viscosity equation C.26 can be written as (Gresho and Sani, 1998)

$$\overrightarrow{\Sigma F_b} = -\left(\nabla p - \eta \left(\nabla^2 \vec{\mathbf{v}} + \nabla \left(\nabla \cdot \vec{\mathbf{v}} \right) \right) \right) dx\, dy\, dz \tag{C.27}$$
$$= -\left(\nabla p - \eta \nabla^2 \vec{\mathbf{v}} \right) dx\, dy\, dz$$

Volume forces

The external or volume forces, such as $F_{v,x}$ acting in the x-directon in equation C.19, can be generalized for all directions as $\overrightarrow{F_v}$. The volume force can contain, for example, gravity or magnetic forces working on the fluid.

Momentum

Because of the principle of conservation of mass equation C.16 can be written as

$$\Sigma \vec{\mathbf{F}} = \frac{d(m\vec{\mathbf{v}})}{dt} = m\frac{d\vec{\mathbf{v}}}{dt} = \rho\, dx\, dy\, dz\, \frac{d\vec{\mathbf{v}}}{dt} \tag{C.28}$$

where the velocity vector field in the medium, $\vec{\mathbf{v}}$, is a function of x, y, z and t. Therefore, the time derivative of the velocity in x-direction v_x is

$$\frac{dv_x}{dt} = \frac{\partial v_x}{\partial t} + \frac{\partial v_x}{\partial x}\frac{dx}{dt} + \frac{\partial v_x}{\partial y}\frac{dy}{dt} + \frac{\partial v_x}{\partial z}\frac{dz}{dt}. \tag{C.29}$$

Because the time derivatives of the coordinates are the components of the velocity vector, this can be written as

$$\frac{dv_x}{dt} = \frac{\partial v_x}{\partial t} + v_x \frac{\partial v_x}{\partial x} + v_y \frac{\partial v_x}{\partial y} + v_z \frac{\partial v_x}{\partial z}. \tag{C.30}$$

Equation C.30 is named the substantial derivative (Rohsenow and Choi, 1961). For all three directions, written in short form, it becomes

$$\frac{d(m\vec{\mathbf{v}})}{dt} = \rho \left(\frac{\partial \vec{\mathbf{v}}}{\partial t} + (\vec{\mathbf{v}} \cdot \nabla)\, \vec{\mathbf{v}} \right) dx\, dy\, dz. \tag{C.31}$$

Inserting equations C.16, C.27, and C.31, and by using

$$\overrightarrow{\mathcal{F}_v} = \frac{\overrightarrow{F_v}}{dx\, dy\, dz} \tag{C.32}$$

gives the Navier-Stokes equations in which the mass conservation principle is taken into account

$$-\nabla p + \eta \nabla^2 \vec{\mathbf{v}} + \overrightarrow{\mathcal{F}_v} = \rho \left(\frac{\partial \vec{\mathbf{v}}}{\partial t} + (\vec{\mathbf{v}} \cdot \nabla)\, \vec{\mathbf{v}} \right) \tag{C.33}$$

with $\mathcal{F}_v$ as specific volume force. This equation is the basis for the calculations of fluid flow under the influence of a pressure gradient, internal and external forces. In this equation the left hand side represents the forces working on the fluid. The terms on the right hand side represent the change of momentum or, in other words, the acceleration of the fluid.

Samenvatting

Dit proefschrift gaat over laserboren met een unieke excimeerlaser met een bijna diffractie-gelimiteerde bundel en een relatief lange optische pulsduur van 175 ns. De combinatie van hoge processnelheid en hoge proceskwaliteit, die verkregen kan worden door de goede bundelkwaliteit, maakt deze laser geschikt voor industriële toepassingen. De bundelkwaliteit maakt het mogelijk om de hele bundel te gebruiken in plaats van masker projectietechnieken toe te passen, zoals gebruikelijk is. Het onderzoek beschreven in dit proefschrift draagt bij aan het fundamentele begrip van de onderliggende processen bij het boren van metalen met deze bijzondere excimeerlaser. Dit fundamentele begrip is nodig om de processnelheid en de kwaliteit van de geboorde gaten te beheersen.

Dit proefschrift begint met een beschrijving van de verschillende processen die een belangrijke rol spelen: het verwarmen van het materiaal door de laserbundel, het smelten en verdampen, het opbouwen van druk ten gevolge van de verdamping en de interactie van de laserbundel met de pluim van verdampt en gesmolten materiaal boven het gat. De belangrijkste bestudeerde onderwerpen zijn de invloed van de pulsduur op het boorproces, de materiaalverwijdering tijdens het laserboren en de mate van transparant zijn van de pluim voor de golflengte van de boorlaser. Aan het eind van dit proefschrift wordt een model van het laser boorproces gepresenteerd.

De experimenten zijn gedaan in het vermogensbereik waar smelt-uitdrijving plaatsvindt, waarvan wordt verwacht dat dit het meest efficiënte proces is voor het verwijderen van materiaal. De materiaalverwijdering is experimenteel onderzocht voor aluminium en Hastelloy X. De grootste hoeveelheid materiaal wordt in de experimenten relatief lang na het eind van de boorpuls verwijderd. De snelheid van de smelt bereikt een maximum wanneer aan het oppervlak de kritische temperatuur wordt bereikt. Berekeningen leiden tot de conclusie dat de geboorde diepte sterk afhangt van de oppervlaktetemperatuur, die direct in verband staat met de warmtegeleiding van het materiaal. Dit impliceert dat de warmtegeleiding een belangrijke parameter voor de bereikbare boordiepte is. Bovendien wordt de oppervlaktetemperatuur sterk beïnvloed door de verzwakking van de laserbundel door de pluim. Voor het boren van aluminium resulteert een eenvoudig model voor de verzwakking van de laserbundel door de pluim in een goede overeenkomst tussen de berekende en de experimenteel gemeten geboorde diepte. De geldigheid van het ontwikkelde model voor het laserboren is aangetoond voor aluminium, nikkel en ijzer, wat aangeeft dat de belangrijkste fysische processen die een rol spelen in het proces op de juiste wijze in het model zijn verwerkt. Wat betreft de efficiëntie, is het boorproces het efficiëntste bij een laservermogen waarbij de smeltuitdrijving volledig ontwikkeld is.

De mate van transparant zijn van de pluim voor de laserbundel is onderzocht voor aluminium, aluminiumoxide, titanium, nikkel, ijzer, silicium, koper en Hastelloy X. Aluminium- en titaniumdamp zijn niet volledig transparant voor de laserbundel, wat verklaard kan worden door het bestaan van absorptielijnen voor het bewerkte materiaal op de lasergolflengte. De andere onderzochte materialen tonen een transparante damp tussen het te bewerken object en de schokgolf. Voor het boren met lage vermogens spelen de processen in de pluim een minimale rol. De experimenten wijzen erop dat, voor het boren met lange pulsduur met hoge vermogensdichtheid, de laserbundel niet sterk wordt verzwakt door de pluim. De verzwakking door de pluim kan bij zeer hoge vermogensdichtheden zelfs afnemen. Dit kan worden veroorzaakt door de afwezigheid van sterke absorptie of verstrooiing van het licht door de pluim bij deze vermogensdichtheden. Een andere reden kan zijn dat de damp in het gat het boorproces ondersteunt, door extra opwarming en een toename van de druk welke beide het resultaat zijn van het absorberen van de laserenergie door de damp.

De invloed van de pulsduur op het boorproces is bestudeerd. Het experimentele werk is gedaan met een pulsknipmethode die resulteert in een regelbare pulsduur waarbij alle andere laserparameters, in het bijzonder de bundelkwaliteit en bundelvorm, ongewijzigd blijven. Het is aangetoond dat met een lange pulsduur, in vergelijking met een korte pulsduur, de boorsnelheid tijdens de puls lager is, maar dat de gaten wijder worden, zodat het verwijderde volume groter is. Berekeningen uitgevoerd met het ontwikkelde model zijn in overeenstemming met de experimenten. Concluderend kan voor de invloed van de pulsduur gesteld worden dat bij boren met lange pulsduur de energie efficiënter wordt benut dan bij het boren met korte pulsduur.

Dankwoord

De resultaten van het werk van de afgelopen vier jaar zijn nu vastgelegd in dit proefschrift. Het werk is uitgevoerd bij het Nederlands Centrum voor Laser Research. Twee vakgroepen van de universiteit Twente waren nauw bij het project betrokken, namelijk, Mechanical Automation waarvan met name de leerstoel Applied Laser Technology en de vakgroep Laser Physics & non-Lineair Optics. Het was uitdagend om te leren omgaan met de cultuurverschillen tussen de drie bij het project betrokken groepen. Zowel commerciele, werktuigbouwkundige als natuurkundige aspecten zijn aan bod gekomen bij het project. De afgelopen jaren heb ik me van alle drie groepen volwaardig deelgenoot gevoeld, en dat voornamelijk door de collegiale sfeer die er was, terwijl ik maar weinig bij de vakgroepen aanwezig was.

NCLR ben ik veel dank verschuldigd voor de mogelijkheid die mij is geboden om dit onderzoek te doen en het proefschrift tot een goed einde te brengen. De promotoren wil ik bedanken voor hun begeleiding van dit werk en hun introductie van mij in de wereld van lasers en de wereld van de wetenschap. Veel dank ben ik verschuldigd aan Kees Biesheuvel voor zijn begeleidende en coachende rol. Door zijn vele ervaring met de karakteristieke XeCl excimeer laser, heeft Ramon Hofstra in belangrijke mate bijgedragen aan het welslagen van de experimenten, waarvoor bedankt. Frits, bedankt voor de samenwerking bij het modelleren. De technici waren onmisbaar voor het welslagen van dit project. Er zijn nog heel veel andere mensen die een belangrijke bijdrage hebben geleverd en die ik nu tekort doe omdat ik ze niet noem. Bedankt allemaal.

Meestal worden de belangrijkste mensen aan het eind bedankt, zo ook nu. Veel heb ik te danken aan mijn ouders en mijn vrouw Wilma. Tijdens de afgelopen jaren heb ik de meest droevige en de meest blijde dagen meegemaakt. Mijn promotietijd begon met de ziekte en het overlijden van mijn vader. Toen kende ik Wilma nog niet, maar enkele maanden voor het afronden van de promotie hebben we elkaar het ja-woord gegeven. Zonder hen had ik het niet gered. Vooral in de momenten dat het allemaal wat minder ging, in geestelijke, maar ook in praktische zin. Na ons trouwen moest het proefschrift af en kregen voor mij huishoudelijke werkzaamheden nogal eens een ondergeschikte rol toebedeeld. Vanaf nu zal ik een betere echtgenoot zijn.

Zalig hij, die in dit leven
Jakobs God ter hulpe heeft;
hij die door de nood gedreven,
zich tot Hem om troost begeeft;
die zijn hoop in ’t hachlijkst lot
vestigt op de HEER, zijn God.

Rhymed version, Psalm 146:3